Coventry University

DOCTOR OF PHILOSOPHY

Impact of porosity on the fatigue performance of wire + arc additive manufactured titanium alloy

Biswal, Romali

Award date:
2019

Awarding institution:
Coventry University

Link to publication

General rights
Copyright and moral rights for the publications made accessible in the public portal are retained by the authors and/or other copyright owners and it is a condition of accessing publications that users recognise and abide by the legal requirements associated with these rights.

- Users may download and print one copy of this thesis for personal non-commercial research or study
- This thesis cannot be reproduced or quoted extensively from without first obtaining permission from the copyright holder(s)
- You may not further distribute the material or use it for any profit-making activity or commercial gain
- You may freely distribute the URL identifying the publication in the public portal

Take down policy
If you believe that this document breaches copyright please contact us providing details, and we will remove access to the work immediately and investigate your claim.

Download date: 22. May. 2025

Impact of Porosity on the Fatigue Performance of Wire + Arc Additive Manufactured Titanium Alloy

by

Romali Biswal

April 2019

Faculty of Engineering, Environment and Computing.

A thesis submitted in partial fulfilment of the University's requirements for the Degree of Doctor of Philosophy

Some materials have been removed from this thesis due to Third Party Copyright or confidentiality issues. Pages where material has been removed are clearly marked in the electronic version. The unabridged version of the thesis can be viewed at the Lanchester Library, Coventry University

Certificate of Ethical Approval

Applicant:

Romali Biswal

Project Title:

Impact of Process induced Porosity Defects on the Fatigue Performance of Wire+Arc Additively Manufactured Ti-6Al-4V

This is to certify that the above named applicant has completed the Coventry University Ethical Approval process and their project has been confirmed and approved as Low Risk

Date of approval:

19 September 2017

Project Reference Number:

P60892

Publications from this research

Some parts of this research has been published in the literature.

Journal papers:

[1] R. Biswal, X. Zhang, A.K. Syed, M. Awd, J. Ding, F. Walther, S. Williams, Criticality of porosity defects on the fatigue performance of wire + arc additive manufactured titanium alloy, Int. J. Fatigue. (2019). doi:10.1016/j.ijfatigue.2019.01.017.

[2] R. Biswal, A.K. Syed, X. Zhang, Assessment of the effect of isolated porosity defects on the fatigue performance of additive manufactured titanium alloy, Addit. Manuf. 23 (2018) 433–442. doi:10.1016/j.addma.2018.08.024.

[3] R. Biswal, X. Zhang, M. Shamir, A.A Mamun, M. Awd, F. Walther, A.K. Syed, Interrupted fatigue testing with periodic tomography to monitor porosity defects in wire + arc additive manufactured Ti-6Al-4V, Addit. Manuf. (under review).

Conference papers/presentations:

[1] X. Zhang, A.K. Syed, R. Biswal, F. Martina, J. Ding, S. Williams, High cycle fatigue and fatigue crack growth rate in additive manufactured titanium alloys, Symposium of International Committee of Aeronautical Fatigue, Poland, 2-7th June 2019.

[2] R. Biswal, X. Zhang, A.K. Syed, Criticality of porosity defects on the fatigue strength of wire + arc additive manufactured titanium alloy, TMS 2019 Annual Meeting & Exhibition, Texas, 10-14th March, 2019.

[3] R. Biswal, A.K. Syed, X. Zhang, Effect of porosity on the fatigue behaviour of additive manufactured Ti-6Al-4V, 12th International Fatigue Congress, France, 27th May-1st June 2018.

To my family and friends...

Acknowledgements

A Phd is similar to a recipe and without the right ingredients, it's unlikely for one to get it right. Fortunately, I can say that I came across the right set of people, without whom this would not be possible. I am very grateful to my Director of Studies, Professor Xiang Zhang, for her expert guidance and for influencing me to be passionate towards the research. My supervisor, Dr. Abdul Khadar Syed, who with his profound experience in experimental studies, helped me with laboratory testing and interpretation of the results.

I am very grateful to Coventry University for funding my study and for the generous studentship. I would also like to thank Dr. Jialuo Ding and Professor Stewart Williams for partly funding the experimental programme through the Engineering and Physical Sciences Research Council (EPSRC) grant. Some of the experimental studies that were performed at external laboratories would not have been possible without the time and effort of Dr. Mamun Abdullah from Open University, UK and Mustafa Awd from TU Dortmund, Germany.

Geoffrey Booth, Barry Meek, Steve Damms and Steven Allitt are some of the many staff members at Coventry University, who contributed immensely during specimen preparation and testing.

I am very thankful to Ibrahim Almakky for raising intriguing research questions and the hour long discussions which often led me in the right direction. Also, Shamir Muhammad, Rohit Kshirsagar, Muhammad Marei, Anees Abu-Monshar and Sherine Zaatari for being audience to my mock presentations and giving constructive feedback.

Beyond academia, I am very grateful to my friends, Jaini Shah, Ankita Saxena, Pamela Mandal and Mousumi Dey, who were my corner stones and kept me motivated through the highs and lows. My heartfelt gratitude goes to my brother, who has always been an instant source of knowledge, motivation, criticism and has been my constant, since the beginning of everything. Finally, my dear parents, whom I can never thank enough for their love and support, without which, I would not be writing anything at all.

Abstract

The additive manufacturing process is a revolutionary technology that has drawn the attention of aerospace and automotive industries. It is particularly attractive for applications involving high-value titanium components, due to substantial material savings and reduced processing times as compared to conventional machining processes. However, the presence of process-induced defects and the limited knowledge database and understanding of the effects of these defects on the fatigue and fracture behaviour of AM parts has been a major concern which impedes their acceptance in safety critical applications.

The process-induced defects can be primarily classified as gas pores, which have a near spherical geometry and lack of fusion defects, which have an irregular geometry. Wire + arc additive manufacturing (WAAM) is a promising technique for depositing large components owing to the high deposition rate (1 kg/hr). Particularly WAAM Ti-6Al-4V parts are reported to be near fully dense (99.99%). Nevertheless, feedstock contamination can lead to the formation of gas pore defects in the parts. Therefore, this research was performed with an aim to study the effect of gas pores in the fatigue behaviour of WAAM Ti-6Al-4V. The primary objectives of the study includes: (a) porosity characterisation, (b) development of a mechanical testing strategy to enable quantitative analysis of the effect of pores on the tensile and fatigue behaviour of WAAM Ti-6Al-4V, (c) modelling the pores using finite element analysis to determine the stress distribution profile, (d) development of a fatigue life prediction method to estimate the effect of gas pores, (e) to determine the critical size of gas pores at various applied stress ranges (failure assessment diagram) for WAAM Ti-6Al-4V.

The test program consisted of two batches of WAAM Ti-6Al-4V specimens, (1) where the material was deposited using the standard processing route, referred to as reference group, and (2) using contaminated wires to deposit the specimen gauge section, referred to as porosity group. The chemical composition (% by weight) of all the influential elements in both the batches were within the permissible limits laid out by ASTM F3302-18. Two dimensional and three dimensional analysis of the gas pores was conducted using optical microscopy and X-ray computed tomography (X-ray CT) respectively. It was evident from the optical images that the

reference group specimens may consist of micron sized pores ($62 \pm 23\mu$m), such that the pore sizes are comparable to the width of the surrounding α colonies ($22 \pm 9\mu$m). In contrast, the size of gas pores in the porosity group specimens ($206 \pm 80\mu$m) were found to be much larger than the width of the surrounding α colonies. Further, the X-ray CT scans showed that the gas pore morphology in both the groups was near spherical and scarcely distributed, such that material density was found to be 99.99% and 99.96% in the reference and porosity groups respectively. Tensile test results showed that the tensile strength and yield strength of both the groups were comparable (tensile strength $859 \pm 4\mu$m and yield strength $802 \pm 7\mu$m). However, the uniform elongation measured in the two groups was widely separated (porosity group 4% and reference group 10%). Similarly, the fatigue limit i.e applied stress range for a life of 10^7 cycles, was 540 MPa for the reference group and 360 MPa for the porosity group at an applied stress ratio of 0.1. This indicates that WAAM Ti-6Al-4V has a notch fatigue factor of 1.5 and notch sensitivity of 0.5 for spherical gas pores.

Finite element (FE) analysis was used to model the pores. Results of the elastic stress distribution at pores modelled using an assumed geometry were compared with the image based meshed models of the pores to confirm that gas pores can be modelled using an ideal spherical geometry. Elastic-plastic cyclic load analysis was performed using a mixed isotropic-kinematic model to obtain the mean stress relaxation effect at the pore root. It was found that the local stress ratio at the pore root was lower than the applied stress ratio. Notch-fatigue approach was applied for fatigue life prediction i.e the stress and strain values calculated by the FE model at the pore root were used in stress-based (for low stress amplitudes) and strain-based (for high stress amplitudes) fatigue life prediction models to estimate the fatigue life of the specimens in the presence of gas pores. The life prediction model was validated with published experimental results as well as the fatigue tests conducted in this research. However, it was observed that the notch-fatigue approach was overly conservative when the crack initiating pore size was comparable to the width of the surrounding α colony. In order to account for the applied stress range as well as the defect size, linear elastic fracture mechanics was implemented. The stress intensity factor range of the crack initiating pore in the reference and porosity group specimens were found to correlate well with the test fatigue life. The correlation was kinked at the value of the long crack threshold stress intensity factor range of WAAM Ti-6Al-4V (ΔK_{th} 4.5 MPa$\sqrt{\text{m}}$ for an applied stress ratio of 0.1). Further, the Kitagawa-Takahashi diagram (failure assessment diagram) was developed for WAAM Ti-6Al-4V in the presence of gas pore defects by setting the lower bound to the notch fatigue limit for gas pores and the remaining section of

the boundary defined by the modified El-Haddad's model proposed by Beretta and Romano. The Kitagawa-Takahashi diagram showed that the critical pore diameter was 100 μm for WAAM Ti-6Al-4V.

Table of contents

List of figures

List of tables

Chapter 1

Introduction

1.1 Background and Motivation

The present study investigates the effects of porosity on the fatigue performance of additive manufactured (AM) titanium alloy. Ti-6Al-4V is extensively used in the aircraft structures due to its high specific strength. However, conventional manufacturing methods (e.g. forging, casting) and subsequent machining operations can lead to approximately 90% of the material removal and thereby increase the buy-to-fly ratio significantly. One such AM process referred to as wire + arc additive manufacturing (WAAM) has gained industrial attention, especially due to the high deposition rates (upto 1 kg/hr) and near fully dense builds. Unfortunately, occurrences of porosity defects cannot be neglected in AM parts, therefore this study was undertaken to characterise a type of defect i.e porosity and to develop suitable predictive models for fatigue life assessment.

The rapid cooling involved with WAAM processing leads to the formation of microstructures that are significantly different from those obtained using conventional thermomechanical processing routes. Additionally, the presence of process-induced porosity defects can also affect the mechanical behaviour of the component. Hence, more research is required to fully understand the implications of the typical AM microstructure and porosity on the mechanical performance. Fatigue testing of WAAM and powder bed AM Ti-6Al-4V samples have shown pores to be the preferred sites for crack initiation. Despite this, while some authors have noted the presence of porosity in WAAM Ti-6Al-4V [34, 14], there has been no study which characterises the pores in WAAM Ti-6Al-4V, based on parameters such as pore size, shape and spacial distribution. Furthermore, there have been no attempts to quantify the effects of the pores on the fatigue life of wire based additive manufactured material; in other words, to understand why cracks are

more likely to initiate at certain pores rather than others and to develop models for predicting the fatigue life and fatigue strength limit.

1.2 Aim and Objectives

The aim of the work presented in this thesis is therefore:
To investigate and predict the effect of porosity defects on the fatigue performance of WAAM Ti-6Al-4V material.

The main objectives are:

- To conduct a state of the art literature survey of AM Ti-6Al-4V.
- To characterise the porosity defects found in WAAM Ti-6Al-4V.
- To obtain material property data of WAAM Ti-6Al-4V using material characterisation techniques.
- To perform experimental studies on WAAM Ti-6Al-4V to understand the role of porosity in fatigue performace.
- To develop predictive models to determine the effect of pores on the fatigue life of WAAM Ti-6Al-4V.
- To determine the critical porosity diameter in WAAM Ti-6Al-4V for fatigue applications.

1.3 Scope, Methods and Thesis Structure

A range of techniques were used to predict the fatigue crack initiation and characterise crack growth. Finite element analysis of idealised pore geometries revealed possible reasons for the preferential nucleation of cracks at certain pores within a component. X-ray computed tomography was also used to identify pores in fatigue samples prior to loading and then repeatedly monitored between loading cycles to study the morphological changes in the pore taking place due to fatigue cycling. Finally, fracture surfaces and crack paths were investigated using scanning electron microscopy in order to understand the crack growth behaviour.

Following this introduction, the work begins with a review and analysis of the published literature on the nature of porosity defects encountered in AM processes, all of which form **Chapter 2**. This lays the foundation for building up on the existing understanding of porosity

and fatigue relationship. Thereafter, the classical theories are presented in **Chapter 3**, which will be used in later chapters while discussing the development of the predictive models and the fatigue damage mechanisms that help in interpreting the experimental results. Having covered the existing knowledge database, a systematic experimental plan was chalked out, the details of which are presented in **Chapter 4**. Novel experimental strategy was implemented to enable the distinct detection and analysis of pores while keeping in mind the limitations of the existing non-destructive techniques. The findings from the experimental studies are elucidated in **Chapter 5**. Later, **Chapter 6** details the finite element modelling and fatigue life prediction method with **Chapter 7** subsequently discussing the fracture mechanics based modelling approach used to identify the critical pore size for fatigue applications. Finally, **Chapter 8** summarises the research findings and draws the final conclusions as well as scopes that this research has opened.

Chapter 2

Literature Review

2.1 Introduction

The subject of structural integrity of aerospace materials and structures can be vast, therefore, the aim of this review chapter was kept specific to the microstructure, mechanical properties and modelling methodologies applicable to additively manufactured $(\alpha+\beta)$ titanium alloy (Ti-6Al-4V). The conventionally processed (wrought or cast) material was considered as a benchmark while making comparative studies on material performance. In the following chapters, novel experiments, finite element analysis and fracture mechanics based modelling methods will be used to obtain useful findings on the effect of the pore characteristics such as shape, size, location and distribution on the fatigue life of the part. Titanium alloys (Ti-6Al-4V in particular) happen to be the material of choice in the aerospace industry due to the high specific strength, corrosion resistance, low thermal expansion and compatibility with carbon-fibre composites. The applications usually include parts subjected to moderate temperatures such as fan blade and casing in the anterior section of the aircraft engine. The high cost of titanium raw material (titanium ingot is about 100 times more expensive than a steel ingot) [35] makes additive manufacturing (AM) an attractive technology as it can render parts very close to the final dimensions and decrease the buy-to-fly ratio due to the considerable reduction in material costs in addition to far less post processing (metal cutting operation). The application of AM parts in commercial aircrafts is growing rapidly with the fast paced research in this field. Finnish Air force were the first to conduct a flight test (Jan, 2018) on an F/A-18 Hornet fighter with an AM Inconel 625 part in the engine [36]. Prior to this, Boeing were the first (in 2017) to design and install an AM titanium part qualified by the Federal Aviation Administration (FAA) on the B787 Dreamliner [37]. Acronic and Airbus worked in collaboration to push the boundaries of AM

to produce FAA-qualified large structures such as pylon spars and rib structures. Consequently, Airbus was the first to install an AM titanium bracket which is part of the aircraft pylon at the junction between the wings and the engines on an in-series production A350 XWB [38]. These advances show the growing demands of AM parts in the aerospace industry.

2.2 Additive manufacturing techniques

According to the American Society for Testing and Materials (ASTM) classification, metal AM processes can be broadly divided into two categories, namely, Powder Bed Fusion (PBF) and Directed Energy Deposition (DED). In PBF, a focussed thermal energy source (laser or electron beam) is used to selectively fuse the metal in the scanned path of the beam. In DED, focussed thermal energy (laser, electron beam or plasma arc) is used to melt and deposit the metal in the desired contour, feedstock can be in the form of powder or wire.

2.2.1 Powder bed fusion (PBF)

The raw material used in this process is in the form of powder. Gas and plasma atomisation are the two main processes which are used for manufacturing metal powders. Since gas atomisation gives smaller diameter powder particles, it is usually preferred for laser based applications [39]. However, the part geometry is usually the determining factor while selecting the AM process and powder type. To make the process more economic, once the part is built, the remaining unfused powder can be reused. A study [40] on Electron Beam Melted (EBM) Ti-6Al-4V reported that the tensile properties of parts built with powder that was reused upto 21 times did not show any significant reduction. However, the number of reuse cycles should be monitored, particularly for the oxygen and aluminium content. Reused powder can show elevated oxygen levels due to exposure to atmosphere and result in the loss of ductility of the part, while the powder deposited around the part during deposition, can be exposed to high temperatures and result in change in composition due to vapourisation of aluminium.

The schematic of PBF process is shown in Figure 2.1 (a) and the heat input during deposition is given by Eq. 2.1.

$$E_d = \frac{P}{vht} \tag{2.1}$$

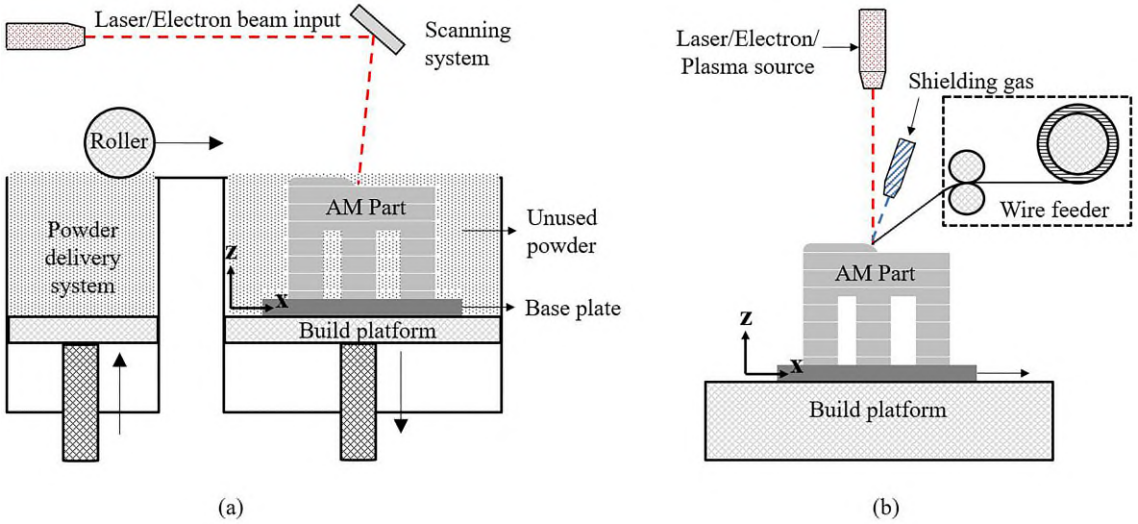

Fig. 2.1 Schematic of: (a) powder bed fusion process, (b) directed energy deposition process; adapted from [1]

where E_d is the energy density (J/mm^3), P the laser/electron beam power (W), v the scanning velocity (mm/s), h the hatch spacing (or the distance between two adjacent scanned rows) (mm) and t the layer thickness (or depth of penetration of the melt pool) (mm).

2.2.2 Directed energy deposition (DED)

This process can use powder or wire as the raw material. The system consists of a powder/wire feeder that inserts the material in the path of the laser/electron beam or plasma arc as shown in Figure 2.1 (b). The advantage of high deposition rate in this approach makes it an attractive option for commercial applications [41]. Similar to PBF process, the energy density in the DED process can also be expressed by Eq. 2.1. The lower surface area of wire in comparison to powder, reduces the chances of contamination. Studies show that the wire-based processes have lower process-induced defects [42]. One such wire-based process referred to as wire+arc additive manufacturing (WAAM), is reported to deliver fully dense (>99.99%) components made of titanium alloy (Ti-6Al-4V) [43, 44].

2.3 Microstructural characterization of AM Ti-6Al-4V

The different AM processes manifest a similar pattern in the microstructure because the directional solidification, but at the same time they also exhibit significant differences in the dimensions, due to the difference in the cooling rates. The phase composition $(\alpha+\beta)$, prior β grain morphology (primarily columnar), α grain morphology (equi-axed or lamellar) and texture

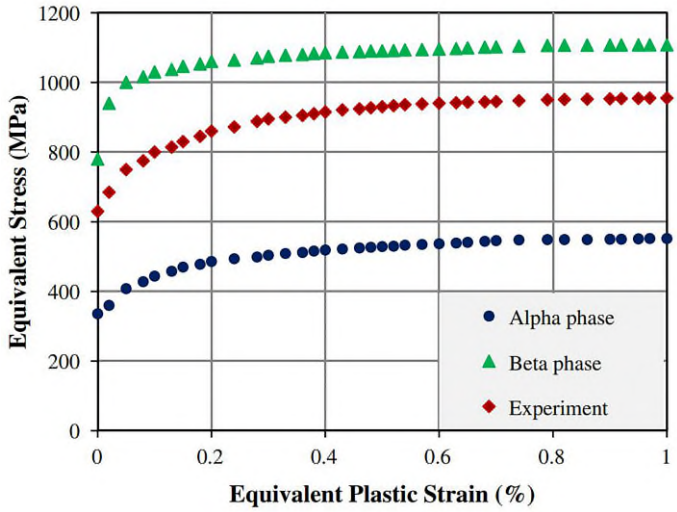

Fig. 2.2 Strength of α and β phases in mill-annealed Ti-6Al-4V; reprint from [2]

(of the α phase) are the important microstructural characteristics that vary with the material processing route and post processing operations performed on the alloy. All AM processes show epitaxial growth of the prior β grains in the build direction due to the directional solidification. The prior β grain boundary is composed of grain boundary α which has a preferred orientation relationship with the adjacent β grain (<0001>α parallel to <110>β). This leads to a micro-textured region across the prior β grain boundaries and forms potential sites for easy slip transmission [45, 46]. Studies show that smaller size of β grains are preferable for fatigue applications as it can resist the transmission of slip [47]. However, as a result of the 12 possible variants of crystallographic orientations, the overall texture in AM Ti-6Al-4V is reported to be weak [48]. Further the columnar β grains can lead to mechanical anisotropy. Another characteristic of AM builds is the graded microstructure i.e the lamellar α width increases with increasing distance from the substrate [49, 50], except for the last few layers, which are acicular due to the absence of overlaying layers.

The Vicker's hardness ratio of the α phase to the β phase is reported to be 0.62 [2]. In addition to different hardness, the two phases also exhibit significant differences in their stress vs. plastic strain response as shown in Figure 2.2. The wide difference in the strength and hardness of the two phases can lead to inhomogeneous strain localisations, with higher strains accumulated in the α phase. Therefore, the fatigue properties of Ti-6Al-4V are directly related to the resistance to slip offered by the α grains [51].

2.3.1 As-deposited condition

Selective Laser Melting (SLM) and electron beam melting (EBM) are the most popular PBF processes. The use of high energy density heat sources results in a cooling rate in the order of 10^4 to 10^6 °C/s [34]. The EBM builds are made in a vacuum chamber with the temperature of the build platform maintained at 600 to 630 °C while the SLM builds are made in a shielding atmosphere (of Argon gas) with the platform temperature maintained at 35 to 230 °C [52, 50]. Due to the lower chamber temperature (hence higher cooling rates) in the SLM process, the resulting microstructure consists of needle shaped non-equilibrium acicular α' phase [53]. The non-equilibrium phase in SLM improves the strength by 20% to 30% (yield point and ultimate tensile strength) as compared to mill-annealed wrought Ti-6Al-4V while reducing the ductility by 30% to 40% [54]. On the other hand, the higher chamber temperature in the EBM process allows an equilibrium transformation (since the chamber temperature is greater than martensitic tranformation temperature, 575 °C [55], non-equilibrium phases are avoided) from β to α phase with a predominantly lamellar morphology with either colony (formed near the prior β grain boundaries) or Widmanstätten arrangement (formed away from the prior β grain boundary). Since colony microstructure is formed at rapid cooling rates [56], the presence of α colony on either side of the prior β grain boundaries indicate higher cooling rates at these locations. As a result of rapid cooling at the prior β boundaries, it is typically not possible for the grain boundary α to maintain the Burgers orientation relationship with both the neighbouring β grains and therefore the orientation of α lamellae is usually different on either side of the grain boundary. As the α lamellae grow away from the prior β grain boundaries, the cooling rate decreases and the α grain morphology becomes basketweave (or Widmanstätten microstructure).

Similarly, depending on the type of energy source (laser, electron or plasma) and raw material (powder-feed, wire-feed) the microstructure in DED processes can vary from non-equilibrium acicular α' (for laser based processes such as directed laser deposition (DLD), direct metal laser sintering (DMLS) etc.) to equilibrium $(\alpha+\beta)$ phase (for electron beam or plasma arc based processes). The microstructure is primarily controlled by the cooling rate and peak temperature during deposition [57]. The volume fraction of α phase is greater than 90% [58, 34], and wire based processes like WAAM have a predominantly Widmanstätten microstructure with an average α lath width of 1.5±1 µm [59, 58, 34]. The lamellar α grain width, Y, expressed as a function of the cooling rate, T, is shown in Eq. 2.2.

$$Y = A \times \dot{T}^{-n} \tag{2.2}$$

where A and n are material constants ($A = 3.1 \times 10^6$ μm $(K/s)^n$, $n = 0.93$ for Ti-6Al-4V [46]).

2.3.2 Heat-treated condition

When the parts are heat-treated above the prior β transus temperature (990 °C), the cooling rate below the transition point controls the recrystallised α grain morphology. Non-equilibrium phases can be avoided by maintaining the cooling rate below 410 °C/s [51]. Heat-treatment operation in the laser based processes cause the non-equillibrium α' phase to transform into α phase, while in electron and plasma arc based processes, the lamellar α grains are reported to undergo grain coarsening due to coalescence of α laths separated by low angle grain boundaries i.e misorientation angles are less than 2° [10, 60, 54]. In order to reduce the processing time and cost in the SLM process, Xu et al. [50] demonstrated that in-situ heat treatment can be performed (by offsetting the focal point of the laser) to obtain parts with higher strength and ductility.

Another commonly applied post-processing technique is hot isostatic pressing (HIPing), which is found to be very effective in making the AM parts near fully dense by fusing the internal defects. HIPing is performed at temperatures close to the $(\alpha - \beta)$ transition temperature and 1000 bar isostatic pressure [52, 60, 61]. However, HIPing also leads to significant grain coarsening, which may not be desirable for high cycle fatigue applications [62]. Alternatively, in-situ rolling [63] and inter-pass rolling techniques [64, 65, 43, 44] have been applied to WAAM process to achieve a significant reduction in the size of prior β grains and additionally eliminating the process-induced defects in the build stage. In this process, the final size of the prior β grains is inversely proportional to the applied rolling force. For an applied reduction of 20%, a final prior β grain size of 90 μm was reported for WAAM Ti-6Al-4V [43].

2.4 Process-induced defects

2.4.1 Gas pores and Lack of fusion defects

AM processed Ti-6Al-4V generally exhibits two broad categories of process induced internal defects. The first category is referred to as gas pores, which are caused by gas entrapment in the melt pool. These pores have a spherical or near-spherical geometry as shown in Fig. 2.3(a). The other category of process induced defects is referred to as lack of fusion (LOF) defect, which can be caused due to use of non-optimum processing parameters leading to insufficient power delivered to the melt pool. The LOF defects manifest as irregular crack-like delaminations as

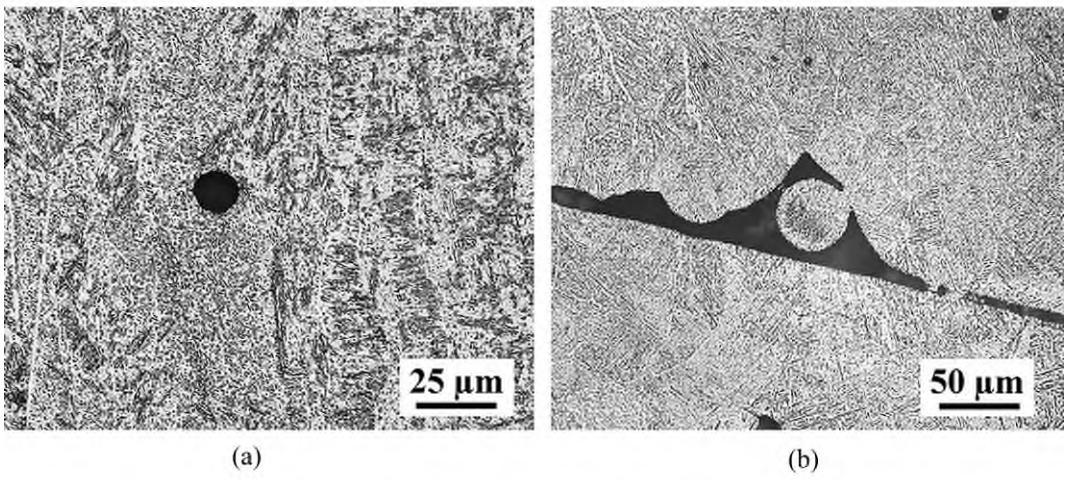

Fig. 2.3 Process-induced defects in Electron Beam Melted Ti-6Al-4V (a) gas porosity (b) lack of fusion; reprint from [3]

shown in Fig. 2.3(b), and can lead to significant reduction in the fatigue performance [61, 66, 67]. Additionally, surface roughness of as-deposited parts [20, 21] and residual stress distortions [6] are also treated as process-induced defects. However, surface roughness and residual stress are beyond the scope of this study and therefore only the porosity defects are discussed.

The volume fractions of porosity in AM Ti-6Al-4V, built with optimised deposition parameters have been reported to lie between 0.03% - 0.19% for EBM [68, 26], 0.08% - 0.23% for SLM [11, 10] and 0.013% - 0.36% for the DLD process [69]. Though WAAM Ti-6Al-4V seldom contains process-induced defects, studies show that feedstock contamination is a common source for occurrence of gas pores in the material [14, 70]. The crack initiating defects reported in SLM and EBM processes are both gas pores and LOFs, while in case of WAAM Ti-6Al-4V they were essentially spherical gas pores.

Some studies [71, 13] stated that the preferential orientation of the long axis of the LOF defects is perpendicular to the deposition direction. The LOFs reported in EBM Ti-6Al-4V [4] show that the orientation of the major axis of 75% of the defects lie at an angle between 70° and 90° to the build direction. This indicates that when the applied external load is perpendicular to the long axis of such defects (i.e loading direction is parallel to the build direction of the part), the part will exhibit poor mechanical performance.

2.4.2 Porosity detection and elimination

Earlier the studies on porosity in AM parts were conducted using density-based approaches, such as the Archimedes' method or destructive techniques such as metallographic analysis. However,

density-based methods do not give any information on the pore shape, size or spatial distribution, which are essential for determining the resulting mechanical properties by computational modelling. Metallographic analysis is a destructive technique and gives information of a specific location in the two dimensional plane, which may or may not be the true representative of the entire part. Therefore, advanced non-destructive techniques such as X-ray computed tomography (X-ray CT) [66] and X-ray synchrotron imaging [72] are increasingly used for obtaining detailed information of the pore characteristics (shape, size and location and distribution) as shown in Figure 2.4. These techniques when coupled with fatigue loading experiments, render valuable insights into the role of pores in the fatigue damage process. In an initial study on cast aluminium alloy [73], the authors applied in-situ X-ray CT scans on cylindrical fatigue specimens and observed that the fatigue crack tip advanced at a higher rate in the vicinity of pores. Later Tammas-Williams et al. [66] performed in-situ X-ray CT scans to study the crack growth from internal pores in EBM Ti-6Al-4V specimens and showed that crack was not initiated at defects, which conventional fracture mechanics would predict based on the defect size and location, but at substantially smaller surface defects. There can be two reasons for this behaviour, first being the fact that the porosity defects reported in [66] had varying morphologies. Since the defect geometry is a critical parameter in determining the stress concentration factor value, a direct comparison of the stress intensity factor based on Murakami's projected square root area parameter [74] may not work. Secondly, the low activation energy required for dislocation movement at surface grains can promote fatigue crack initiation [75]. Nevertheless, studies involving detection of crack initiation using X-ray CT technique still remain a challenge as the cracks may not be detected until the crack opening distance reaches the minimum detection resolution of the equipment (e.g. 20-30 microns) [66].

It has been reported that post processing operations such as hot isostatic pressing [11, 68, 60] and cold rolling [64, 65, 43, 44] can be very effective in removing the LOF defects and in shrinking the gas pores such that the final size is less than the minimum detection resolution. However, complete elimination of gas pores is difficult due to the internal gas pressure. Furthermore, it has been reported in a study [68] that those gas pores which had been reduced to sizes below the X-ray CT resolution via HIPing, subsequently regrew when the material was subjected to elevated temperatures at above 1000°C. This can be due to the combined effect of an increase in the internal pressure in the gas pore and the simultaneous recrystallisation and grain growth taking place in the microstructure at temperatures above the β transus temperature. A recent study [72] using in-situ X-ray synchrotron imaging monitored the

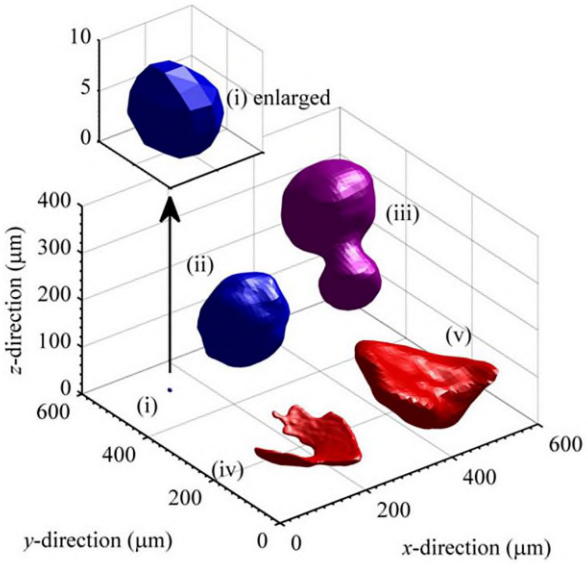

Fig. 2.4 X-ray computed tomography image of EBM Ti-6Al-4V (reprint from [4]), showing (i) small, (ii) large and (iii) coalesced spherical gas pores and (iv-v) sharp irregular lack of fusions.

melt pool solidification and porosity evolution during EBM of Ti-6Al-4V and concluded that centrifugal Marangoni convention force drives the entrapped gas pores in the melt pool. This is evidence of the high probability of gas entrapment in the melt pool and therefore it is important to understand the impact of gas pores on the fatigue behaviour.

2.5 Mechanical properties

2.5.1 Tensile behaviour

The yield strength, tensile strength and ductility properties depend on the AM process and the post-processing applied. Fig. 2.5 shows the published results of tensile properties of various AM processes. It can be seen that in as-deposited condition, particularly the studies on SLM Ti-6Al-4V show that the yield strength lies between 938 - 1143 MPa, tensile strength between 1035 - 1219 MPa and ductility between 2% and 12 % [5–11]. The respective values for EBM and DED processes (laser, electron and plasma arc) were found to be similar to each other, with the yield strength reported between 812 - 860 MPa, tensile strength 782 - 939 MPa and ductility 4% and 15 % [12–14]. All the values mentioned above correspond to the tensile properties of vertically oriented specimens, i.e uniaxial load was applied parallel to the material deposition direction. It is worth mentioning that the relatively similar microstructure of EBM, laser - wire directed energy deposited (L-W DED) and WAAM Ti-6Al-4V results in comparable tensile

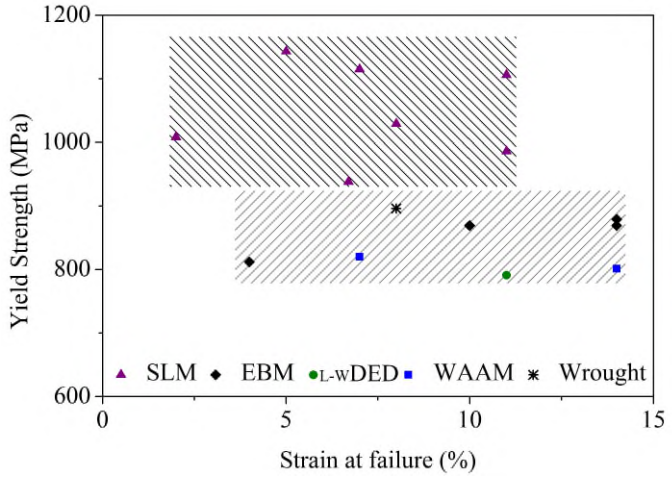

Fig. 2.5 Tensile properties of Ti-6Al-4V processed using selective laser melting [5–11], electron beam melting [12, 13], laser - wire directed energy deposition [13] and wire + arc additive manufacturing [14, 15] reported in literature. Wrought data [16].

properties. In contrast, the rapid cooling rates in SLM Ti-6Al-4V lead to the formation of a non equilibrium $\alpha - \beta$ microstructure with α' causing higher strength and lower ductility [5].

Post-processing techniques such as heat treatment and hot isostatic pressing, were found to reduce the yield strength and tensile strength by 10 to 15% for all the processes. This can be due to the grain coarsening effect caused by the coalescence of low angle α laths. Grain coarsening also results in improved ductility, however, the significant rise in ductility in HIPed specimens is primarily due to the removal of internal defects.

It can be observed that in both the AM processed Ti-6Al-4V (PBF and DED) the difference between the stress at onset of yielding and the stress at the onset of necking is about 10%, which indicates that the material has limited work hardening and is therefore better suited for high cycle fatigue applications (materials being operated at stresses well below the yield strength value). High strength and low work hardening increases the sensitivity of the material towards process-induced defects such as gas pores and lack of fusion pores.

2.5.2 Cyclic stress vs. strain behaviour

Experimental tests in literature have shown that the cyclic stress-strain relationship of SLM [5, 17] and DLD Ti-6Al-4V [18] are very similar in comparison with the wrought material as shown in Fig. 2.6. This indicates that a common cyclic stress-strain curve may be used for modelling Ti-6Al-4V processed by the different powder-based AM techniques. It can also be inferred from Fig. 2.6 that Ti-6Al-4V undergoes cyclic softening. The amount of cyclic softening exhibited by AM processed Ti-6Al-4V was however much lower in comparison with wrought

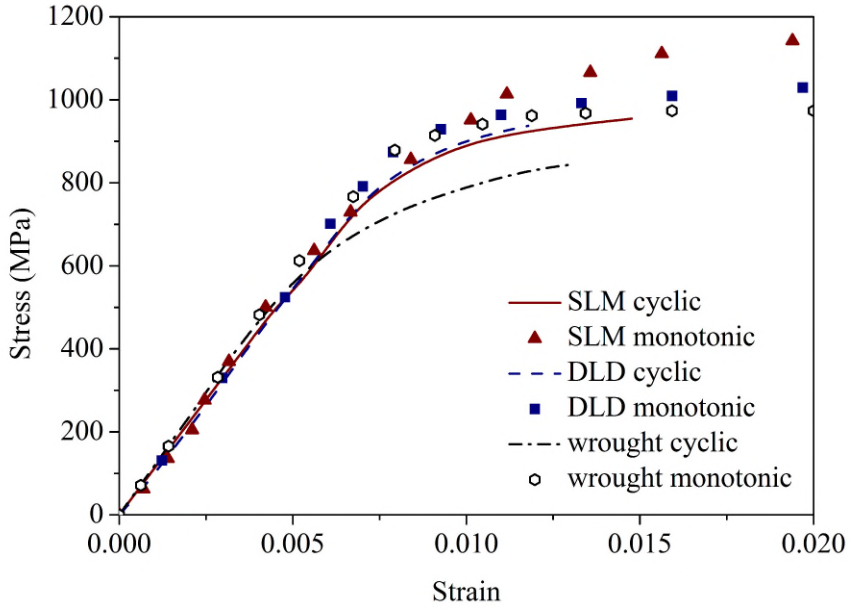

Fig. 2.6 Cyclic stress-strain curves of powder based AM Ti-6Al-4V i.e selective laser melted [5, 17] and direct laser deposited (DLD) [18] processed Ti-6Al-4V compared with wrought Ti-6Al-4V [16].

Ti-6Al-4V. This is because rapid cooling in powder based AM process leads to the formation of martensite or lamellar α. Due to the much smaller width of the α grains, the movement of dislocations is restricted and therefore the limited cyclic softening.

2.5.3 Fatigue behaviour

A number of studies have been performed to understand the fatigue behaviour of Ti-6Al-4V manufactured either via SLM [23, 27, 11, 20, 19], EBM [66, 20, 24, 21, 52, 26], DLD [18, 13] or WAAM process [14, 15]. The published fatigue life data shows that unpolished test specimens i.e specimens built using near net shape deposition, have inferior fatigue performance as compared to the specimens tested with a machined surface finish. It was also observed that there was no measurable influence of any post processing technique on the unpolished fatigue specimens. Specimens tested with a machined and polished surface showed a significant improvement in the fatigue strength as shown in Fig. 2.7 [19–21]. The near net shape builds are reported to have a surface finish of $38.5 \pm 1.7 \mu$m for SLM Ti-6Al-4V and $131.4 \pm 45 \mu$m for EBM Ti-6Al-4V [76]. Rough and undulated surfaces cause stress concentration at the surface features that act as preferable fatigue crack initiation sites.

It was also observed that the fatigue performance of the polished specimens which were subjected to thermal treatment (i.e heat treatment without HIPing) were comparable to the non-heat treated or asbuilt polished specimens [52, 27, 18]. This indicates that internal defects

dominate the fatigue behaviour more than the material microstructure in the case of machined (or polished) specimens. Fatigue performance of HIPed AM Ti-6Al-4V was comparable to wrought Ti-6Al-4V when the applied stress ratio was 0.1 as shown in Fig. 2.8. However, the fatigue performance of HIPed AM Ti-6Al-4V was better than wrought Ti-6Al-4V for applied stress ratio of -1 as shown in Fig. 2.9. This is because under reversed loading conditions, roughness induced crack closure and crack bridging phenomena can be significant [77]. It is reported that the effect of these mechanisms is higher for lamellar microstructure as compared to equi-axed microstructure [78]. However, for tension-tension loading (positive stress ratios) these mechanisms are not as effective and hence the two microstructures (lamellar and equi-axed) perform similarly.

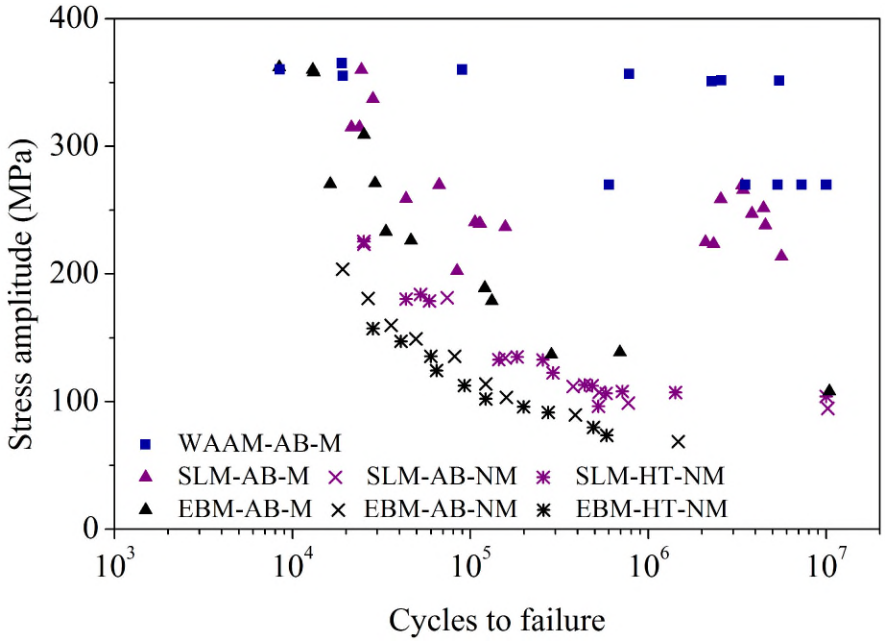

Fig. 2.7 Published non-HIPed condition (with internal defects) S-N data of SLM [19, 7], EBM [20–22] and WAAM Ti-6Al-4V [15, 14] reported in literature. Wrought data [16]. All the presented data were tested at a stress ratio of 0.1. [Meaning of legends: AB-asbuilt, HT-heat treated, M-machined and polished surface, NM- non-machined surface i.e near net shape builds].

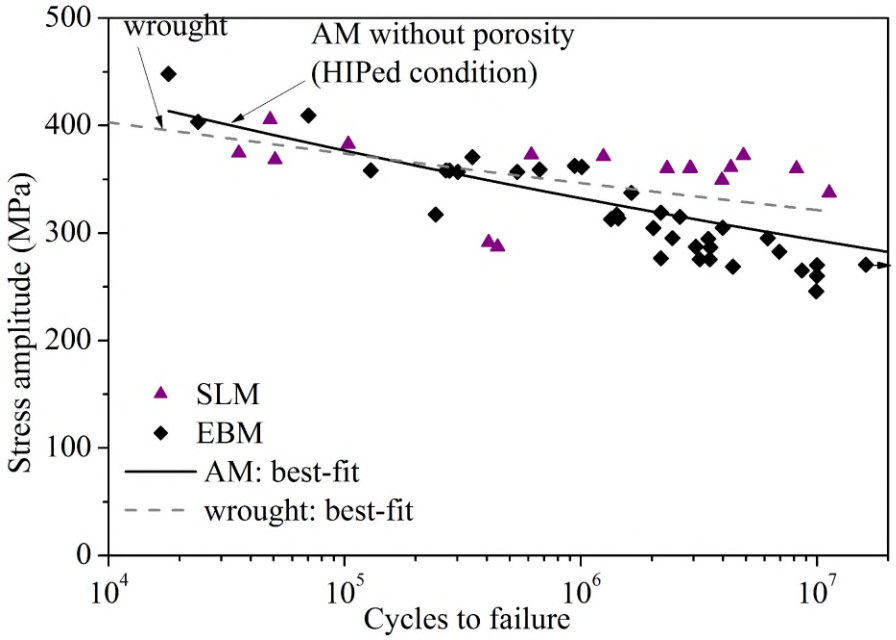

Fig. 2.8 Published HIPed S-N data of SLM [23, 20] and EBM Ti-6Al-4V [24, 13, 25, 26, 20] reported in literature. All the presented data were tested at a stress ratio of 0.1. Wrought data [16].

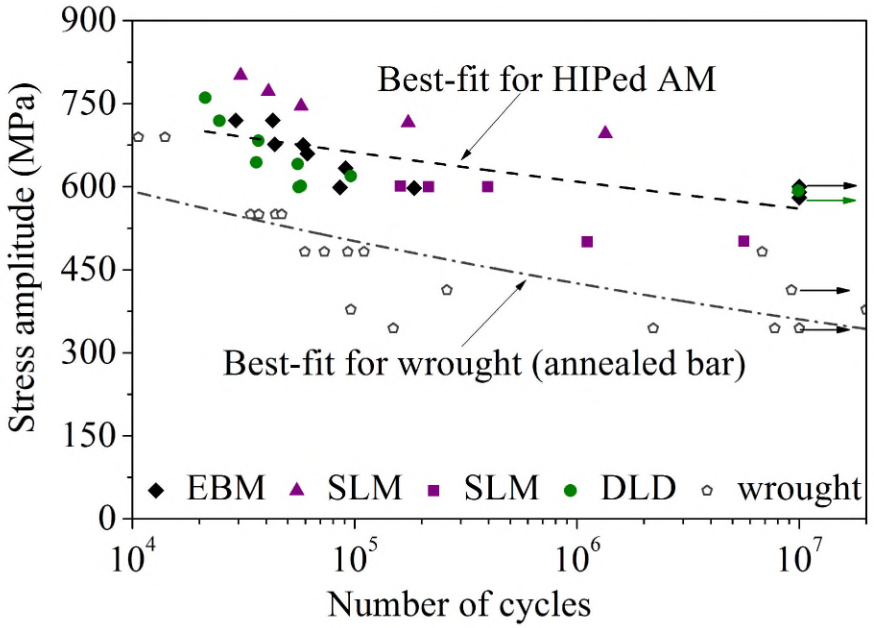

Fig. 2.9 Published HIPed S-N data of SLM [27, 11], EBM [28] and DLD Ti-6Al-4V [28] reported in literature. All the presented data were tested at a stress ratio of -1. Wrought data [16].

2.6 Predictive models

In terms of defect-based modelling and fatigue life prediction, the commonly used approaches in the literature are, probabilistic modelling, using statistical techniques (such as the weakest link theory [79, 67, 80, 81]), micromechanical modelling using the crystal plasticity finite

element method (FEM) [82–84], continuum mechanics method using the notch-fatigue approach developed for macroscale notches [85, 86] and material's S-N data, and fracture mechanics modelling based on damage tolerance design approach [87, 88, 74, 89].

2.6.1 Probabilistic approach

In this approach the material strength is assumed to be stochastic in nature while assuming a random distribution of the defects. Development of such statistical models require sufficient number of mechanical tests to obtain a representative correlation. One such study on SLM AlSi10Mg [67] has reported a correlation between the static strength and fatigue limit in the presence of internal defects. However, due to significant differences between the material properties and microstructure of AlSi10Mg and Ti-6Al-4V, the correlation may not be applied directly to AM Ti-6Al-4V. In [61], the authors applied a Weibull distribution to correlate the failure probability to the defect size in powder bed fusion processes (SLM and EBM). It was found that crack initiation from pores and from α phase had a similar trend, and as anticipated, the failure probability of specimens with lack of fusion defects was higher. The approach was based on the size of the defect and since the porosity defects reported in the study were an order of magnitude smaller than the lack of fusions, the lower failure probability was justified. However, this approach did not account for the shape of the defect and may lead to conservative predictions when applied to larger pores. Moreover, the established statistical methods are validated with powder bed fusion processes, which is known to have higher population of porosity as compared to wire-based processes such as WAAM Ti-6Al-4V, where the parts exhibit fewer and isolated pores [14, 34].

2.6.2 Micromechanical modelling approach

Microstructure controls the fatigue behaviour, particularly when the applied cyclic stress level is close to the fatigue limit. An experimental study conducted using digital image correlation techniques showed that the strain localisations (or dislocation pile ups) are more prone to occur along the α laths with the long axis oriented at 45° to the loading axis [47]. Effects of such inhomogeneities can be heightened in the presence of a defect due to stress redistribution. The resultant stress and the corresponding microstructural response can be captured using the crystal plasticity finite element method. Crystal plasticity modelling can be implemented via the user defined material subroutine (UMAT) in the ABAQUS® software to compute the mechanical response of explicitly modelled grains in the polycrystalline material under the applied loading

condition. In [82], the authors presented a three dimensional crystal plasticity FE model to study the cyclic stress vs. strain response of wrought Ti-6Al-4V at the grain scale. It was found that due to the small difference between the critical resolved shear stress values of the basal, prismatic and pyramidal slip systems (varying between 370 MPa and 490 MPa), the α grain has a higher probability of undergoing failure by multiple slip activity, especially when the applied stress levels are high. The fitting parameters of the isotropic hardening and softening model are found from Eq. 2.3 [82].

$$\tau^{k}_{\mathrm{CRSS}} = \frac{\kappa_y}{\sqrt{d^k}} + \kappa^{k}_{s}(0) + D^k \tag{2.3}$$

where τ^{k}_{CRSS} is the resolved shear stress on the slip plane, κ_{y} and $\sqrt{d^k}$ the Hall-Petch slope and the microstructural dimension of the free slip length and microstructural dimension respectively, D^k remains unchanged and is equal to the difference between the CRSS and the initial threshold stress on the k^{th} slip system.

In another study [90], the authors applied this approach to model an open hole in EBM Ti-6Al-4V. In order to reduce the complexity, only the lamellar α phase was considered in the model without the β phase as more than 90% of the material is reported to exist in the α phase [58, 61]. The study [90] showed that when the hole diameter was large in comparison with the surrounding microstructure, the stress distribution map conformed to the strain distribution around the hole. However, as the hole diameter reduced to microstructural dimension i.e less than 8 times the width of the lamellar α grains [91], the strain distribution was dependent on the orientation of the individual α lamellae instead of the applied stress. This indicates that when the defect size reduces to microstructural dimension, microstructure based modelling approaches can give accurate fatigue life estimations.

2.6.3 Continuum mechanics approach

Due to their regular spherical geometries, the gas pores behave as stress raisers and therefore the effect can be modelled using notch-fatigue analysis where the local stress and strain amplitude at the notch root govern the fatigue life of the component. The continuum mechanics approach can be applied using various parameters, which determine the level of complexity and accuracy of the life prediction.

(a) Stress concentration factor (K_{t})

The inhomogeneous stress distribution around a notch or a defect can be represented using the stress concentration factor. K_t is defined as the ratio of the maximum stress at the pore root in the load direction to the gross applied stress. The geometry of the defect plays an important role in controlling the value of K_t. Using the theory of elasticity, analytical solutions of K_t can be derived for 3-D geometries i.e stress raisers, such as spherical cavity [31], elliptical cavity [92] and surface hemispherical dent [32] in an infinitely large body. It is worth mentioning that except for the analytical solution of spherical internal cavity, Eq. 2.4, the K_t for the rest of the 3-D geometries have been derived for a fixed Poisson's ratio of 0.25. Being a 3-D geometry, the value of Poisson's ratio affects the value of K_t. In this scenerio, finite element modelling can be implemented to obtain the K_t for different values of Poisson's ratio, applied loading conditions and more importantly to understand the effect of the stress raiser in a finite part geometry.

$$K_t = \frac{27 - 15v}{14 - 10v} \tag{2.4}$$

where K_t is the stress concentration factor at the mid-riff region of a spherical cavity in an infinitely large body and v is the Poisson's ratio for the material (v=0.32 for Ti-6Al-4V [66]).

With advanced imaging techniques such as X-ray Computed Tomography (X-ray CT), more realistic crack initiation models can be developed by mapping the porosity distribution in the part and transferring it to FEA models via image based meshing techniques. In this way, the porosity shape, size and location details can be applied to the FEA.

In a study [93], the authors imported the X-ray CT scanned map of cylindrical test specimens into ABAQUS® and performed elastic stress analysis with uniaxial static load. The authors defined a parameter called 'porosity characteristic' and defined it as the ratio of pore size to the pore distance from the nearest free surface. A correlation between the value of K_t obtained from the FE model and the 'porosity characteristic' parameter was proposed [93]. However, this parameter did not include the geometry of the porosity defect, which is a critical parameter controlling the value of K_t. Also, the K_t obtained by this correlation was found to be of much lower than the theoretical K_t for a spherical cavity in an infinite solid given by Eq. 2.4 [31], and therefore, may not be applicable for gas pores.

(b) Notch fatigue factor (K_f)

Since metallic materials exhibit ductility, the local stress at the root of the stress raiser tends to be lower than the value calculated using elastic stress analysis. The value of notch fatigue factor for any material can be obtained from experimental fatigue tests conducted on the notched and the smooth specimens, where the ratio of the fatigue strength of notched specimens to

the fatigue strength of smooth specimens gives the notch fatigue factor. For commonly used alloys, this value can be obtained from Peterson's handbook [33]. Classical fatigue assessment of notched structures are based on the notch fatigue factor as shown in Eq. 2.5 [86].

$$K_f = 1 + q(K_t - 1) \tag{2.5}$$

where K_f is the notch fatigue factor, q the notch sensitivity of the material. The value of q depends on the microstructure and the notch geometry and is reported to be around 0.5 to 0.6 for SLM and EBM Ti-6Al-4V [20, 94]).

(c) Local stress-strain values ($\sigma - \varepsilon$)

The local stress-strain at the notch or defect can be computed either using analytical techniques such as Neuber's method [95] or using FEA [30]. Neuber's method uses either K_t, given by Eq. 2.6 or K_f, given by Eq. 2.7 to determine the value of local stress-strain values. As mentioned earlier, use of K_f should be preferred to avoid a conservative prediction in case of metallic materials.

$$\sigma_a \varepsilon_a = \frac{(K_t S_a)^2}{E} \tag{2.6}$$

$$\sigma_a \varepsilon_a = \frac{(K_f S_a)^2}{E} \tag{2.7}$$

where σ_a is the local stress amplitude, ε_a the local strain amplitude, S_a the gross applied stress amplitude and E the Young's modulus of the material.

The calculated local stress-strain values can be applied either in Basquin's equation [96], or Coffin-Manson equation [97, 98] to predict the fatigue life of the part.

It is worth mentioning that the classical stress-life and strain-life equations are produced at a stress ratio of -1, i.e no mean stress. Therefore, while performing tests at stress ratios other than -1, the mean stress effect should be accounted. Also, Ti-6Al-4V is reported to exhibit cyclic softening behaviour which would result in a mean stress reduction on application of cyclic stresses. In other words, the local stress ratio might differ from the applied stress ratio. Smith-Watson-Topper model [99] and Morrow's model [100, 101] are commonly used in literature to account for the local stress ratio variation for Ti-6Al-4V [102, 103].

2.6.4 Fracture mechanics approach

Existing fracture mechanics based models account for the effect of porosity on the fatigue performance by determining the reduced fatigue limit on the basis of the projected area of the defect on the plane perpendicular to the loading axis [60, 61]. According to one such model, known as Murakami's model as shown in Eq. 2.8 [104], fatigue limit can be expressed as a function of the defect location (using a correlation co-efficient), the defect size (using the square root of the projected area) and the material's Vicker's hardness. This approach worked for irregular LOF defects (similar to cracks) in AM Ti-6Al-4V [61, 19] but gave a highly conservative prediction for specimens with gas pores [60].

$$\Delta\sigma_{\mathrm{w}} = \frac{C_1(HV+120)}{\sqrt{area}^{1/6}} \tag{2.8}$$

where $\Delta\sigma_{\mathrm{w}}$ is the reduced fatigue limit due to defect, HV is the Vicker's hardness of the material, *area* is the projected cross-sectional area of the defect in the plane normal to the loading direction and C_1 is a location parameter with a value of 1.43 for surface defects, 1.41 for sub-surface defects and 1.56 for internal defects.

Kitagawa-Takahashi diagram as shown in Figure 2.10 [105] is one of the most used analysis tool for qualitative representation of the fatigue design limits. The two limits in the diagram are obtained from specimen testing, i.e. the S-N data (to determine the fatigue limit in defect-free condition) and crack propagation rates (to determine the threshold value of the stress intensity factor range, which gives the condition for non-propagating cracks.

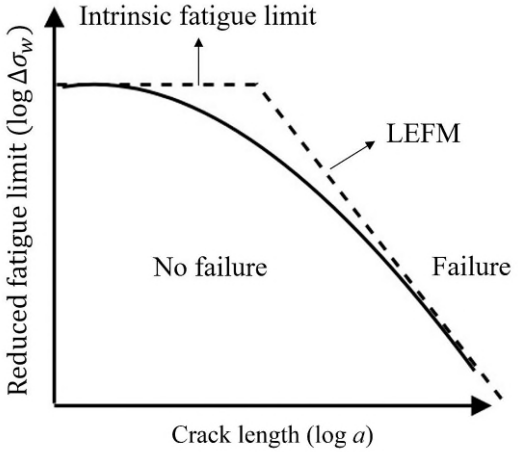

Fig. 2.10 Kitagawa-Takahashi diagram, showing the safe and unsafe regions for a given fatigue life.

2.7 Summary

Microstructure:

The layer-wise deposition approach followed by additive manufacturing (AM) process compliments the existing capabilities of the manufacturing industry with advantages of material savings and unparalleled design freedom. However, the layer-wise deposition strategy also subjects the AM processed parts to a complex thermal history which can vary the microstructure from part to part and even from location to location within the same part.

Porosity:

In addition to the variation in microstructure, process-induced defects in AM processes are a major topic of concern for causing scatter in the fatigue performance. Presence of porosity defects cause localised regions of higher stress which depends on the pore characteristics (size, shape and location). However, limited studies report all the porosity characteristics, either due to the inherent randomness of pores or due to equipment limitations. Only one study implemented X-ray computed tomography technique and monitored the growth of pores during fatigue loading. There is still a gap in understanding the role of pores, primarily due to the difficulty associated with its detection.

Pore vs. microstructure:

Since Ti-6Al-4V shows low work hardening (the difference between yield stress and ultimate tensile strength is relatively small), the material is sensitive to porosity defects. Further, depending on the size of the pore in comparison to the surrounding microstructure, it can either act as a microscopic or a macroscopic stress raiser. Since Ti-6Al-4V is a ductile material, the sensitivity to microscopic defects is low, however, macroscopic defects with diameters greater than the surrounding α lamellae by a factor of eight or more can be adverse for fatigue applications.

Life prediction:

In terms of defect-based modelling and fatigue life prediction, the statistical approaches have been used effectively for correlating fatigue life of test specimens to the initial porosity distribution map obtained from X-ray computed tomography (CT) particularly in case of AM aluminium alloy. All the studies on microstructure models, notch-fatigue and fracture mechanics method involving Ti-6Al-4V were focused on powder-based AM processes which have higher porosity density and irregular shaped lack of fusion defects. However, in case of wire-based processes, the parts exhibit fewer and isolated pores which have a predominantly spherical morphology.

Therefore, this study aims to contribute towards understanding the role of gas pore defects on the fatigue performance of wire + arc additively manufactured Ti-6Al-4V. It is important to link the effect of gas pores on the fatigue life so that their impact on the structural integrity of the component can be predicted. This step has not yet been attempted in the literature therefore a systematic testing and modelling strategy as shown in the project outline in Fig. 2.11 was developed in the following chapters.

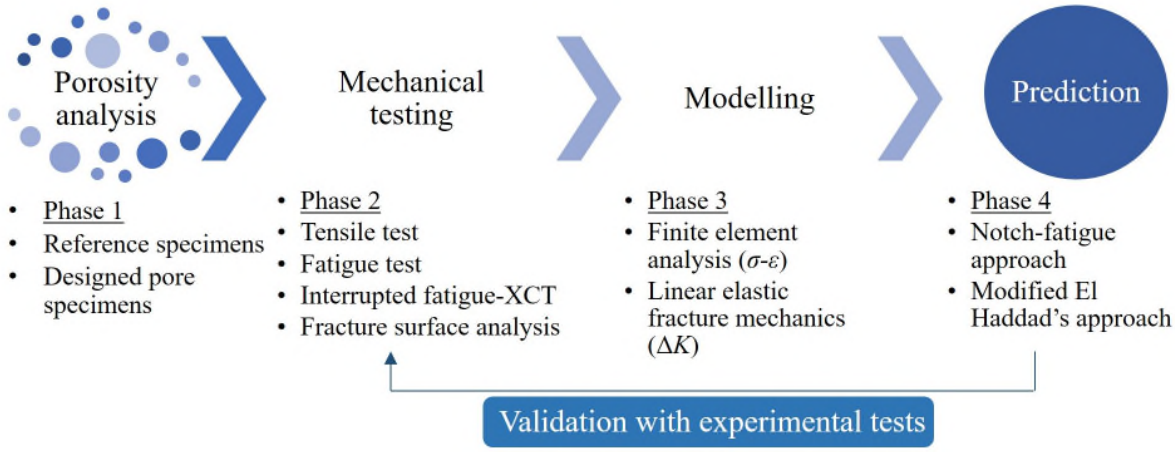

Fig. 2.11 Outline of the work plan.

Chapter 3

Theoretical Framework

3.1 Introduction

Fatigue is a complex phenomena and the associated failure mechanisms vary widely depending on the crack initiating feature. In this chapter, attention is first directed at the mechanisms leading to fatigue crack initiation at stress concentration sites which includes experimental evidences of role of stress raisers in accelerating cyclic damage. This will be followed by an introduction to the classical deformation concepts such as Bauschinger effect, dislocation movements and slip characteristics. Later, continuum aspects of fatigue crack initiation and the corresponding fatigue design approaches used in the aircraft and automobile industries have been discussed. Such modelling methodologies are particularly useful for uniaxial cyclic deformation conditions where the material behaviour can be represented using an isotropic and kinematic hardening model. This chapter will then be concluded with the derived assumptions and models applicable for the present study on crack initiation at process-induced porosity defects in WAAM Ti-6Al-4V.

3.2 Cyclic deformation behaviour

Formation of persistent slip bands have been identified as the predecessor of fatigue crack initiation. However, in case of polycrystalline materials, especially when the material exhibits texture, fatigue life of similarly processed samples can show a significant scatter in the fatigue life. This is due to the microstructural variations and the associated activation energies of the different slip systems. Additive manufacturing is known to result in some level of texture effect, especially near the prior β grain boundaries, which can become preferred crack initiation sites. Strains are manifested by dislocation pile-ups at grain boundaries and free surfaces. These dislocation bands

tend to become increasingly prominent with increasing number of cycles. When the dislocation density becomes sufficiently high, it leads to formation of an intrusion-extrusion pair, that is the mark of crack nucleation. In the presence of stress raisers, this process is expedited by the high stress created at the root of the stress raiser. In other words, in a localised region, the stress is sufficiently high to cause dislocation pile-up. The magnitude of local stress is controlled by the geometry of the stress raiser, while the size and shape of the plastic zone is controlled by the applied stress and the size of the stress raiser with respect to the part geometry. It is known that low cycle fatigue is dominated by the crack propagation phase while the high cycle fatigue is dominated by the crack initiation phase [77]. However, presence of a stress raiser adds a complexity, i.e the local high stress region, which undergoes plastic strain accumulation while the surrounding region is elastic. Also, the probability of fatigue crack initiation is higher when the plastic zone size increases. Therefore, to understand the effect of microstructure, the following section presents the established concepts which lay the foundation for comprehending the fatigue failure mechanisms [77].

3.2.1 Role of microstructure

Microstructural aspects such as persistent slip bands, grain boundaries, micro-pores and inclusions are some of the competing elements at play during fatigue load applications. Intrusion-extrusion pairs appear at the slip bands which have the active slip planes (low critical resolved shear stress) oriented approximately at 45° to the loading axis. Such cracks are often referred to as microstructural or slip-band cracks and constitute the 1st stage of fatigue crack growth. In the 1st stage, the crack path is zig-zag or jagged (sharp deflections), since the crack goes through the active slip planes of the neighbouring grains, and the crack propagation behaviour is referred to as transgranular propagation. The effect of the surrounding microstructure is most significant in this stage of crack growth. The presence of two phases, i.e α and β in Ti-6Al-4V increases the microstructural barriers for the micro-crack. However, the lower strength of the α phase compared to the β phase, and the minimal percentage of the retained β phase in the final microstructure of WAAM Ti-6Al-4V make it possible to determine the fatigue performance by studying the α phase alone [51].

The α phase has 12 slip systems, which include the 4 slip planes (basal (0002), prismatic $\{10\bar{1}0\}$, 1st order pyramidal $\{10\bar{1}1\}$ and 2nd order pyramidal $\{11\bar{2}2\}$) and 3 primary slip directions of type <11$\bar{2}$0> (which results in 12 possible slip systems in the α phase). The prismatic and basal slip systems have lower values of critical resolved shear stress (370 MPa and 420 MPa

respectively [82]), which are activated when the c-axis of the α phase is aligned at 45° to the loading direction [56].

3.2.2 Cyclic response

In general, soft metals (metals with a large difference between yield stress, σ_{ys} and ultimate tensile stress, σ_{uts}, such that the ratio of σ_{uts} to σ_{ys} is greater than 1.4) have lower dislocation density in the beginning and the application of cyclic loading rapidly increases the dislocation density resulting in cyclic strain hardening. On the other hand, the dislocation density is high for harder metals (when the ratio of σ_{uts} to σ_{ys} is less than 1.2) and an application of cyclic loading results in a rearrangement of the dislocations into a new configuration such that it offers less resistance to deformation, thereby leading to cyclic strain softening [106]. Various individual phenomena act in combination to result in such complex cyclic responses. Strain hardening takes place when the applied stresses are above the material's yield strength. Microscopically, this happens by the progressive pile up of dislocations at the microstructural barriers such as grain boundaries, persistent slip band walls etc., which increases the stresses necessary to cause further movement of dislocations. On the contrary, Bauschinger effect causes reduction in the yield stress when the loading direction is reversed (refer Fig. 3.1a). This can be either due to the lower energy requirements in the reversed loading direction since the dislocations are piled-up at obstacles in the loading direction, or due to the long-range internal stresses that favour early yielding in the reversed loading direction [106]. The changes in the yield surface with cyclic loading is frequently represented using isotropic and kinematic hardening mechanisms as shown in Fig. 3.1(b). The isotropic hardening mechanism assumes a uniform expansion of the yield surface in the tension and compression direction i.e magnitude of the yield stress in tension is equal to the yield stress in compression. While the kinematic hardening mechanism keeps the size of yield surface constant while translating the centre through the stress space [77].

The cyclic response of a material is obtained from a displacement controlled fully reversed cyclic load test. Within 20 to 100 cycles the dislocation substructure stabilises and the stress vs. strain response at this state gives the stabilised hysteresis loop [29]. The area under the hysteresis loop indicates the accumulated plastic strain energy in each cycle and is representative of the cyclic response of the material for fatigue loading for the applied strain level. The stabilised cyclic stress-strain curve of the material can be obtained by joining the tips of the stabilised hysteresis loops as shown in Fig. 3.2. The stress vs. strain relationship is given by Eq. 3.1 which is also referred to as Ramberg-Osgood equation [107]. A logarithmic plot of the stress vs. plastic

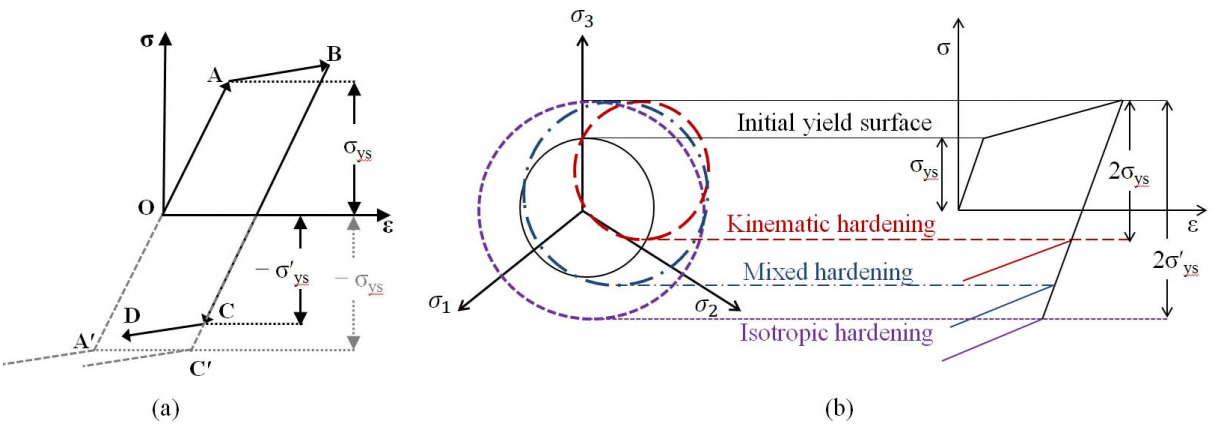

Fig. 3.1 (a) Path *OABCD* shows the Bauschinger effect (yield stress in compression reduces from C' to C) [29] and (b) schematic of the changes in the yield surface through isotropic and kinematic hardening mechanisms.

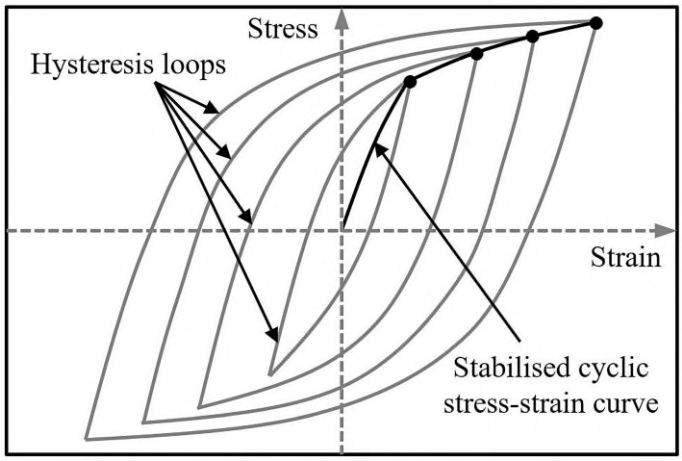

Fig. 3.2 Schematic of stabilised hysteresis loops and corresponding stabilised cyclic stress vs. strain curve obtained by joining the tips of hysteresis loops.

strain component from the stabilised cyclic stress vs. strain curve is often used to model the cyclic plastic response of the material.

$$\Delta\varepsilon_a = \frac{\Delta\sigma_a}{E} + \left(\frac{\Delta\sigma_a}{K'}\right)^{1/n'} \tag{3.1}$$

where $\Delta\varepsilon_a$ is the strain range, $\Delta\sigma_a$ the stress range, E the Young's modulus, K' the cyclic strength coefficient and n' the cyclic strain hardening exponent.

Cyclic response of ductile metals are widely modelled using isotropic and kinematic hardening or softening models. An isotropic hardening or softening model assumes the material response to be symmetrical (i.e any change in the flow stress in tension is also observed in equal magnitude in compression loading due to the uniform expansion of yield surface such that the shape and centre remains unchanged). This however does not represent the Bauschinger effect where changes in flow stress in tension are not equal to that in the reversed loading condition.

This effect is implemented via kinematic model where the yield surface translates (without any change in shape or size) in the stress space in the direction of its normal.

3.3 Notches and defects

Notches and defects act as sites of stress concentration and alter the stress distribution profile in the vicinity as shown in Fig. 3.3(a). Other effects include difference in the mean stress at the root of the notch or defect as compared to the applied value, local plastic deformation and strain mismatch at the interface of the plastically deformed region and the surrounding elastic region, which can lead to crack nucleation. One of the most commonly used terms in the study of stress raisers is theoretical stress concentration factor (K_t), which is an elastic concept and is defined as the ratio of the maximum stress or strain (at the notch or defect root) to the (gross) applied stress or strain. It should be mentioned that K_t is a geometric parameter and depends only on the defect morphology, part geometry and the size ratio of the defect to part containing the defect. For volumetric defects, Poisson's ratio, which is a material property, also affects the value of K_t. This is because, the volumetric defects are constrained in the material and Poisson's ratio controls the change in lateral strain for an applied longitudinal strain in a material. For simple geometries such as open hole in an infinitely wide plate or a spherical cavity in an infinite solid, the mathematical solution under uniaxial loading can be derived using the theory of elasticity as shown in Eq. 3.2 [33] and Eq. 3.3 [31] respectively.

$$K_t = 1 + 2\left(\frac{b}{a}\right) \tag{3.2}$$

where K_t is the stress concentration factor at the points highlighted in Fig. 3.3(a) when the width of the plate, W, is significantly larger than a (a and b are the major and minor diameters of the hole. For open circular hole, a=b).

$$K_t = \frac{27 - 15v}{14 - 10v} \tag{3.3}$$

where K_t is the stress concentration factor at the mid-riff region of a spherical cavity in an infinitely large body and v is the Poisson's ratio for the material (v=0.32 for Ti-6Al-4V [66]).

Some of the common experimental measurement techniques of K_t include photoelasticity and strain gauges. For photoelasticity (refer Fig. 3.3b), a transparent replica specimen with identical geometry as the test specimen is loaded to study the changes in the optical properties of the material (which depend on the stress distribution) using a polariscope. Alternatively, strain

gauges can be fixed at the root of the defect to measure the local strain which is proportional to the stress under linear elastic condition. This technique is frequently used in industrial applications due to the easiness of use [107].

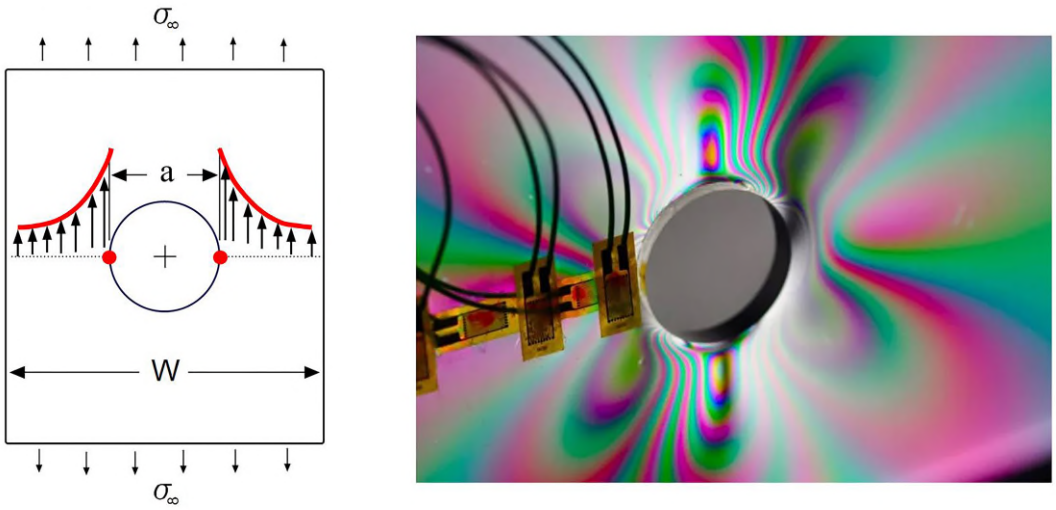

Fig. 3.3 (a) Schematic of stress distribution for open hole, (b) photo-elastic fringes for a uniaxially loaded open hole in a wide plate [source: https://teamuv.org/tag/photoelasticity/]

Once the value of K_t is known, semi-analytical techniques such as Neuber's method (Eq. 3.4) can be used for determining the plastic strain amplitude at the root of the notch.

$$\sigma_a \varepsilon_a = \frac{(K_t S_a)^2}{E} \tag{3.4}$$

where σ_a is the applied stress amplitude and ε_a is the strain amplitude and E is the $Young's$ modulus of the material. For ductile metals, use of fatigue notch factor (K_f) is preferred instead of K_t to avoid over conservative predictions.

However, derivation of mathematical solutions for K_t become increasingly difficult as the complexity of the defect and the part geometry increases in addition to the true loading and boundary conditions being further away from assumptions of infinite distances. With advanced computing capabilities numerical methods based on finite element analysis (FEA) are being increasingly used for determining the stress concentration factor at complex geometries. Nevertheless, the result is highly dependent on the mesh quality at the region of stress concentration. Therefore, the first step in using FEA based techniques for determination of stress concentration factor value should be mesh convergence.

3.4 Fatigue design methods

3.4.1 Infinite and safe-life design

Parts with a service life of a million cycles such as engine valve springs and railroad axles, are designed to be operated at stresses and strains less than the fatigue limit of the material. This approach is non-economic and impractical for aircraft applications where weight reduction is critical. On the contrary, designing for a finite life (which is more than the service life of the part) is called safe-life design. This requires the stress-life and strain-life experimental data and is widely used for jet engine, pressure vessel and gun tube designs. The stress-life relationship given by Basquin's equation [96] and strain-life relationship given by Coffin-Manson equation [97] are shown in Eq. 3.5 and Eq. 3.6 respectively.

$$\frac{\Delta\sigma_{\mathrm{e}}}{2} = \sigma_{\mathrm{f}}'(2N_{\mathrm{f}})^{b} \tag{3.5}$$

$$\frac{\Delta\varepsilon_{\mathrm{p}}}{2} = \varepsilon_{\mathrm{f}}'(2N_{\mathrm{f}})^{c} \tag{3.6}$$

where in Eq. 3.5, $\Delta\sigma_{\mathrm{e}}$ is the applied elastic stress range, σ_{f}' and b are material constants referred to as fatigue strength co-efficient and fatigue strength exponent respectively. The values of σ_{f}' and b are obtained from the intercept and slope of $\frac{\Delta\sigma_{\mathrm{e}}}{2}$ vs. N_{f} plot (with the stress ratio equal to -1) on a logarithmic scale. In Eq. 3.6, $\Delta\varepsilon_{\mathrm{p}}$ is the applied plastic strain range, $\varepsilon_{\mathrm{f}}'$ and c are material constants referred to as fatigue ductility co-efficient and fatigue ductility exponent respectively. The values of $\varepsilon_{\mathrm{f}}'$ and c are obtained from the intercept and slope of $\frac{\Delta\varepsilon_{\mathrm{p}}}{2}$ vs. N_{f} plot (fully reversed loading) on a logarithmic scale. N_{f} is the number of reversals to failure.

The factor of safety (FOS) can be specified in terms of load (usually FOS = 2) or in terms of fatigue life (usually a factor of 20 is applied), which makes the design well within safe operational limits. In the presence of notches, instead of the applied stress or strain, the local stress and strains at the notch root are used for determining the design limits. The local strain amplitude can be calculated using FEA or Neuber's method. It is important to consider the effect of mean stress variation at the notch root due to the cyclic plasticity effect. The constants in Eq. 3.5 and Eq. 3.6 are derived for fully reversed loading condition (i.e mean stress is zero). For non-zero mean stresses, models accounting for the mean stress effect such as Smith-Watson-Topper (Eq. 3.7), Morrow (Eq. 3.8), Walker (Eq. 3.9) etc. should be used.

$$\varepsilon_a \sigma_{max} = \frac{(\sigma_f')^2}{E}(2N_f)^{2b} + \sigma_f'\varepsilon_f'(2N_f)^{b+c} \tag{3.7}$$

$$\varepsilon_a = \frac{\sigma_f' - \sigma_m}{E}(2N_f)^b + \varepsilon_f'(2N_f)^c \tag{3.8}$$

$$\sigma_e = \sigma_{max}\left(\frac{1-R}{2}\right)^n \tag{3.9}$$

where ε_a and σ_{max} are the strain amplitude and maximum stress amplitude at the notch root, σ_m is the local mean stress, σ_e the equivalent stress amplitude for fully reversed loading, R the local stress ratio and E the Young's modulus of the material.

3.4.2 Damage tolerant design

The Paris law (shown in Eq. 3.10) [108] forms the foundation of this method, where the structure is subjected to periodic non-destructive inspection to detect any cracks. Once the crack is detected, the residual life of the structure is estimated based on the fatigue crack growth behaviour data (Paris equation). Unlike the former approach (infinite and safe-life design) where the part is designed for crack nucleation and the residual life is neglected, the present approaches increase the cost effectiveness including the residual life, which is particularly a large percentage of the total fatigue life of metallic parts.

$$\frac{da}{dN} = C(\Delta K)^m \tag{3.10}$$

$$\Delta K = \beta \Delta\sigma\sqrt{\pi a} \tag{3.11}$$

where da/dN is the crack growth rate, ΔK is the stress intensity factor range, C and m are material constants derived from the intercept and slope of the da/dN vs. ΔK plot in a logarithmic scale. The value of ΔK for a given crack is calculated using Eq. 3.11, where β is the geometric parameter depending on the crack location and part geometry, $\Delta\sigma$ is the applied stress range and a is the half crack length.

Fig. 3.4 shows the classic Paris curve which is applicable in the long crack regime, i.e region III, where the crack length is much larger than the size of plastic zone ahead of the crack tip. This will allow the application of the linear elastic fracture mechanics (LEFM), so that the crack tip stress field is dominated by elastic stresses. The ASTM standard defines a

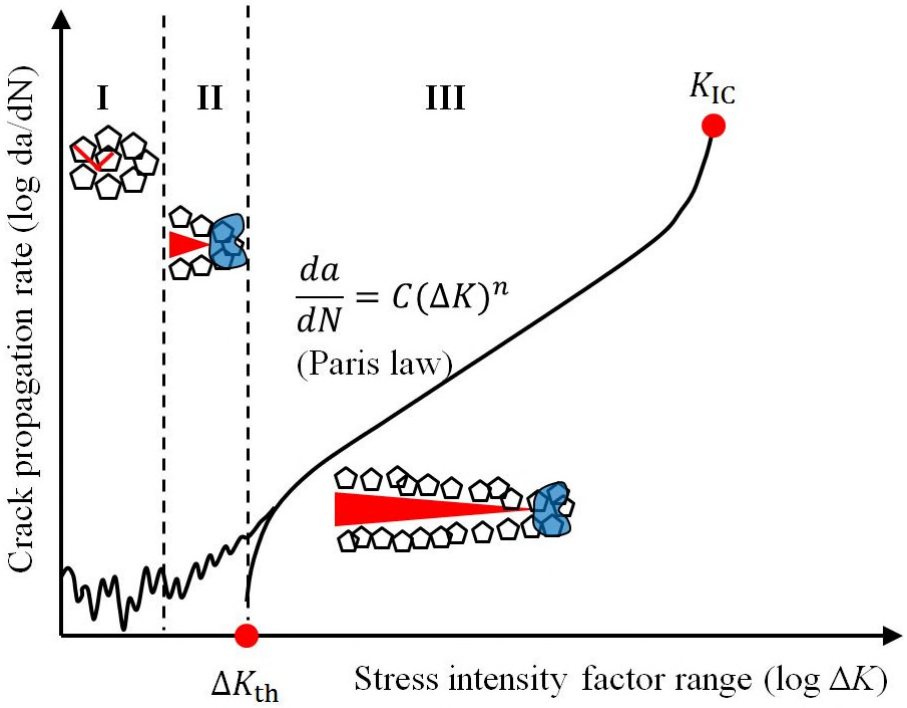

Fig. 3.4 Different regimes of fatigue crack growth with schematic representation of the crack length scale with respect to surrounding microstructure. Region I: microstructurally short crack contained within few grains; region II: mechanically short crack, comparable to the plastic zone size; region III: long crack, when crack length is much larger than plastic zone size. (adapted from [30])

LEFM long crack as 50 times greater than the crack tip plastic zone size. The propagation behaviour and crack growth rate of such a crack can be described by the Paris law. However, the porosity defects and small cracks initiated from porosity, fall within the so-called short crack regime shown in region II [109], where the crack size is comparable to the crack tip plastic zone size. Consequently, the LEFM similitude principle does not hold for such defects, and a correction factor should be accounted in order to avoid non-conservative predictions of fatigue crack growth life. Experimental studies [110, 111] have confirmed that the Paris law significantly underestimates the growth rate of short cracks.

The Kitagawa-Takahashi diagram [105] has been frequently applied for qualitative representation of the fatigue design limits. The fatigue strength of the material in defect-free condition and the threshold value of stress intensity factor for long cracks, obtained from the S-N data and the fatigue crack growth data respectively, are used to determine the boundary for non-propagating cracks. However, since the short cracks propagate at a much faster rate than that predicted by linear elastic fracture mechanics [110], El Haddad et al. introduced a fictitious crack size to increase the crack driving force in the short crack regime [89]. Later, Murakami and Endo [112] proposed a parameter derived from the projected area of defect to represent an effective crack size for embedded defects. Subsequently, Beretta and Romano adapted the El Haddad model

and the root area parameter to predict the non-propagating crack condition for the lack of fusion defects encountered in AM materials [87]. These models [112, 89, 87] have been proven to be accurate for lack of fusion defects [19, 80, 52], which are comparable to a planar crack geometry. However, only one study has tested Murakami's approach on gas pore defects and found it to be conservative [60]. These works will be discussed further in Chapter 7 for developing meaningful correlations between the porosity size and fatigue strength.

3.5 Summary

This chapter introduces the established theories related to cyclic deformation and fatigue failure. The dependence of cyclic response of a material to the microstructure was presented. The 12 slip systems in the α phase of Ti-6Al-4V indicate that the cyclic deformation behaviour will be dominated by the characteristics of the α phase. In addition, being a high strength alloy, Ti-6Al-4V is more likely to undergo cyclic softening, which causes the yield strength to reduce with increasing number of cycles. Consequently, the concepts of isotropic and kinematic hardening and softening were discussed. Isotropic cyclic deformation causes the yield surface to expand or shrink symmetrically in tension and compression while kinematic cyclic deformation maintains the shape and size of the yield surface while translating it in the stress space in the direction of its normal. For Ti-6Al-4V, a combination of isotropic and kinematic deformation behaviour would be applicable since the material undergoes significant cyclic softening (modelled via isotropic algorithm) and exhibits Bauschinger effect (modelled via kinematic algorithm).

Next the notch fatigue theory was discussed, which included the Neuber's method of calculating local plastic strains based on the energy equilibrium using the elastic stress concentration factor concept. It was identified that the first step towards quantifying the effect of a stress raiser on the fatigue performance is the determination of the elastic stress concentration factor associated with the defect. For complex defect geometries and non-ideal boundary conditions (which arise due to the finite width of the specimen), finite element analysis is one of the most used techniques. Depending on whether a porosity defect is treated as a stress raiser (similar to notch) or a short crack, both notch-fatigue and linear elastic fracture mechanics with El Haddad's correction for short cracks can be studied further for application into modelling porosity defects in WAAM Ti-6Al-4V.

Chapter 4

Experimental Methodology

4.1 Introduction

Wire-based processes are gaining increased attention for their low cost and high deposition rates with an added advantage of lower process-induced defects [42]. One such wire-based process referred to as wire+arc additive manufacturing (WAAM), is reported to deliver fully dense (>99.99%) components made of titanium alloy (Ti-6Al-4V) [44]. Studies have shown that the resultant microstructure of WAAM Ti-6Al-4V is highly dependent on the rate of cooling and the maximum temperature in the melt pool during deposition [57]. The volume fraction of α phase is greater than 90% [58, 34], with a predominantly Widmanstätten microstructure and an average α lath width of 1.5±1 μm [59, 58]. The prior β grains are columnar and aligned in the build direction which can lead to mechanical property anisotropy in terms of the tensile [14, 15] and fatigue strength [14]. However, more studies comparing the tensile and fatigue performance of WAAM Ti-6Al-4V in the vertical and horizontal directions (with respect to the build direction) are required to confirm the extent of mechanical anisotropy. Therefore, the first objective of this research was to perform tensile and fatigue tests on WAAM Ti-6Al-4V to gain insight into the intrinsic material performance.

Even though WAAM Ti-6Al-4V seldom contains process-induced defects, studies show that feedstock contamination is a common source for occurrence of gas pores [14, 70]. Recent advances on the application of in-situ rolling [63] and inter-pass rolling techniques [65, 64] have shown promising results in homogenising the microstructure by making the prior β grains equiaxed and more importantly, eliminating the process-induced defects in the build stage. However, adding a processing step increases the time and cost of production significantly.

Therefore, the next objective of the study was to device suitable experimental strategies to enable the quantitative study of pores and its effect on the fatigue performance.

4.2 Manufacturing strategy

4.2.1 WAAM Ti-6Al-4V wall

Optimised processing arameters were used to build the WAAM Ti-6Al-4V walls. The processing parameters are shown in Table 4.1. The manufacturing set-up consisted of a HiVE machine (High-Value Engineering) with a Fronius Plasma 10 module attached to a rotator, allowing the co-axial rotation of the wire feeding unit around the plasma torch. The plasma arc was controlled by a Fanuc robot arc mate 120i. A water-cooled backing plate was provided to dissipate the heat from the substrate during deposition. Argon gas of 99.99% purity was used as shielding gas and was placed ahead of the torch and as well as the trailing end of the torch, directed precisely at the melt pool to avoid oxidation. Oscillation strategy was used to deposit the material as shown in Fig. 4.1(a), which resulted in a wall thickness of 27 mm as shown in Fig. 4.1(b). The chemical composition of the Ti-6Al-4V wire (AWS 5.16- grade 5, 1.2 mm diameter) and the walls deposited for the study have been provided in Table 4.2. Chemical composition of the wire was taken from the product certificate and that of the deposited walls from energy dispersive X-ray spectroscopy (for the primary elements) and LECO® analysis (for gaseous elements). The base plate was a hot-rolled Ti-6Al-4V of 12 mm thickness and was clamped to a rigid steel backing block during deposition. The clamping of the base plate prevents any distortion due to thermal residual stresses.

Table 4.1 WAAM Ti-6Al-4V wall build parameters

Current (A)	210	Plasma gas (l/min)	0.8
Torch stand-off (mm)	8	Plasma shield (l/min)	10
Travel speed (m/min)	3.5	Trailing shield (l/min)	200

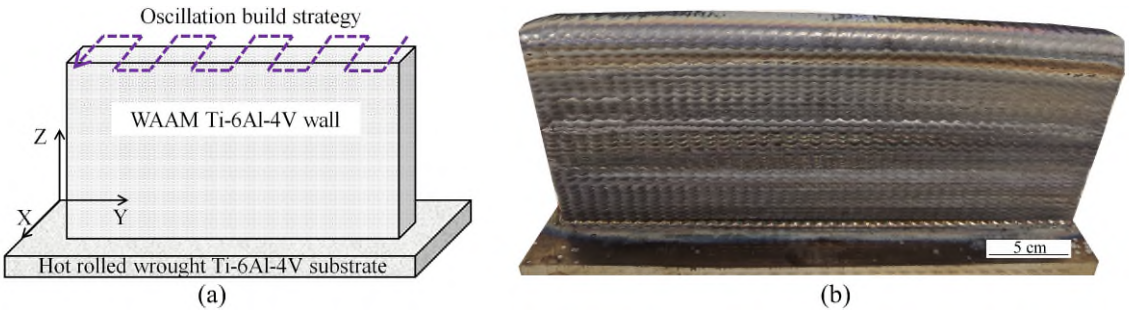

Fig. 4.1 (a) Schematic of WAAM Ti-6Al-4V wall deposition strategy, (b) finished wall used for specimen extraction (material was deposited in *Z*-direction).

4.2.2 Specimen extraction

The deposited walls, referred to as 'reference' and 'porosity', were built with optimised processing parameters. The porosity wall (Fig. 4.2b) was built with contaminated wires in the mid-section (which forms the gauge section of the specimens) and the rest of the wall was deposited with clean wires. Water displacement 40^{th} formula (WD-40®) was used to contaminate the wire. Selective contamination of the specimen gauge section results in (3-7 times) larger pores as compared to the pores found in the reference material (this study) as well as the pores reported in literature for WAAM Ti-6Al-4V built without any known contamination [14]. This strategy is particularly applied in this study because larger pores are easier to detect and monitor using X-ray CT. The test specimens were extracted in parallel with the build direction.

Table 4.2 Chemical composition (weight %) of feedstock (wire) and deposited walls (reference and porosity). [NA: data not available].

	Al	V	Fe	O	C	N	H	ResidualTi	
Wire	6.24	4.18	0.131	0.15	0.01	0.009	0.005	<0.4	Balance
Reference wall	5.61	3.8	NA	0.18	NA	0.008	0.007	NA	NA
Porosity wall	5.89	3.8	NA	0.17	NA	0.017	0.006	NA	NA
Allowable [113]	5.5-6.75	3.5-4.5	0.3	0.2	0.08	0.05	0.015	<0.4	Balance

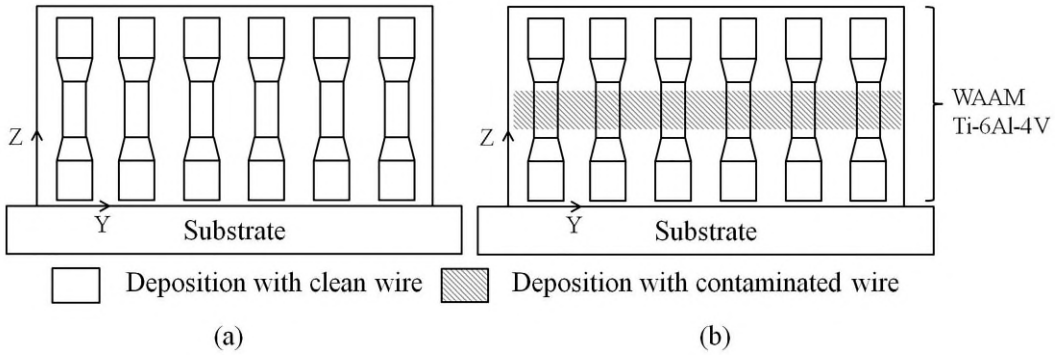

Fig. 4.2 Schematic of specimen extraction: (a) reference specimens, (b) porosity specimens using contaminated wires at the gauge section. Material was deposited in the *Z*-direction.

4.3 Material characterisation

4.3.1 Optical and electron microscopy

The optical microscopy examinations were conducted with Axio-observer materials inverted microscope manufactured by Carl Zeiss, UK. Metallographic specimens were extracted in different orientations with respect to the build direction as shown in Fig. 4.3(a). The metallography specimen preparation involved grinding and polishing operations according to ASTM E3 standard. For microstructure examination, Kroll's reagent was used to reveal the microstructure via etching (caused by selective corrosion of the β phase).

Porosity characteristics (shape, size and area fraction) was studied in the as-polished samples. It should be noted that porosity area fraction measurement is a two dimensional technique based on the pores on the inspected surface and may not be true representative of the porosity fraction in the entire wall. This value has been reported to be less than the porosity volume fraction measured using X-ray computed tomography [4], which gives more information regarding pores as compared to optical images. In case of microstructural studies, multiple images were stitched to capture the large prior β grain boundaries. The stitched images were then processed using ImageJ® software to measure the α and prior β grain sizes by line intersection method according to ASTM E112. The microstructure was systematically inspected in the build direction to observe the changes in the α lath width through the build height.

Scanning electron microscopy (Zeiss Sigma 500 VP) was used to obtain high resolution images of the microstructure and the fracture surfaces of the tensile and fatigue specimens. The working distance and beam energy was set to 7.5 mm and 15 kV respectively for high resolution imaging. However, the overall images (at low magnification of 30$\times$ to 40$\times$) of the tensile and

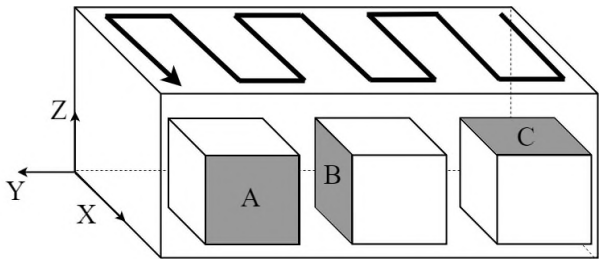

Fig. 4.3 Schematic of metallographic specimens extracted from WAAM Ti-6Al-4V wall for optical microscopy of surfaces marked as A, B and C (build direction is along *Z*-axis).

fatigue fracture surfaces (fractography analysis) were taken with a working distance between 30 mm to 45 mm. Further, detailed examination of selected sites on the fracture surface was performed with working distance between 7.1 mm to 7.5 mm and beam energy of 10 kV to 20 kV .

Electron back scatter diffraction (EBSD) imaging was performed to obtain the texture property of WAAM Ti-6Al-4V. In this case, the polished specimens were subjected to additional six hours of polishing using vibration polishing (Buehler VibroMet®) at 80% vibration amplitude. The mirror polished specimens were then inspected under the EBSD camera for the texture analysis. A high binning mode was used to enable a large area scan with 21 reflectors for α phase detection and 55 reflectors for the β phase detection. The working distance was 10 mm, beam energy 20 kV, scan area 500 $\times$ 400 μm^2 and step size 0.6 μm for all the scans.

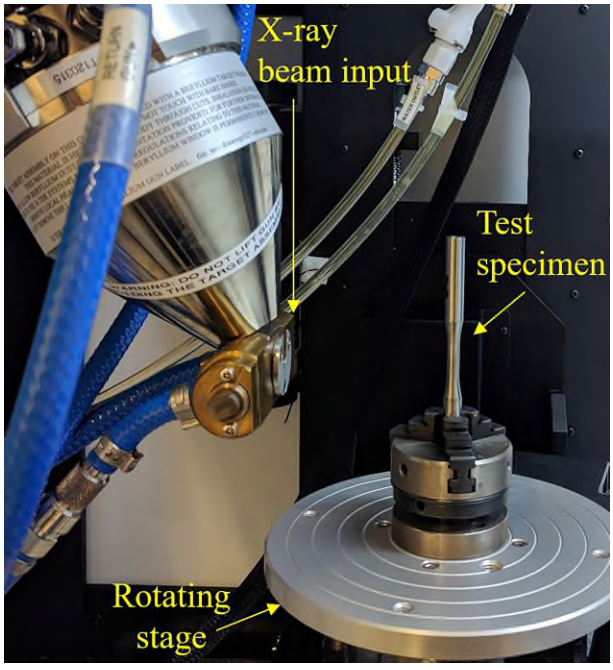

Fig. 4.4 X-ray computed tomography measurement set-up for porosity mapping in specimen gauge section

4.3.2 X-ray computed tomography

An X-ray computed tomography (X-ray CT) scanning unit (X TH 160 system, Nikon Metrology) was used to map the spatial distribution and three dimensional morphology of pores in the gauge section of the test specimens as shown in Fig. 4.4. The target specimen was placed in between the X-ray beam source and the detector. The X-rays incident on the specimen gets attenuated and the attenuated beam is captured by the detector. The attenuation depends on the density of the material in the path of the beam. The X-ray CT scans were conducted at an accelerating voltage of 120 kV, current of 58 μA and voxel size of 20 μm (effective pixel size of 10 μm). Exposure time was set at 500 ms and rotation step size at 0.22° while capturing approximately 1600 radiographic projections for mapping the gauge section of the fatigue test specimens. Total time required for scanning each specimen was approximately 50 minutes. The final three dimensional image was then reconstructed from the series of projected images using Volume graphics® software (VG Studio Max 2.2).

4.4 Mechanical tests

4.4.1 Tensile test

Table 4.3 gives a summary of the number of tests performed. Using wire-electric discharge machining, flat tensile specimens were machined according to ASTM E8 standard as shown in Fig. 4.5(a). Specimen surface roughness was measured with a light interferometer and was found to be 2±0.3 μm. Four specimens each from reference and porosity group were tested with a 250 kN Instron servo-hydraulic test machine at room temperature at a strain rate of 0.06 min^{-1}. Strain was measured with an Instron extensometer of 25 mm gauge length.

4.4.2 Cyclic stress-strain test

Displacement controlled cyclic load test specimens were extracted from the reference wall in vertical orientation with respect to the build direction and machined according to ASTM E606

Table 4.3 No. of specimens tested

Test	Reference group	Porosity group
Tensile	4	4
Fatigue	20	24
Interrupted fatigue-tomography	-	3

as shown in Fig. 4.5(b). Tests were performed at room temperature with a 100 kN Instron servo-hydraulic test machine. Three specimens were tested, and each specimen was subjected to fully-reversed cyclic loading with constant strain amplitude loading at a strain ratio of -1. Each specimen was tested at fixed strain amplitude (1%, 1.5% and 2%), at a frequency of 0.1 Hz. The stress and strain values were recorded at a frequency of 40 Hz until the hysteresis loops reached to a stabilised state.

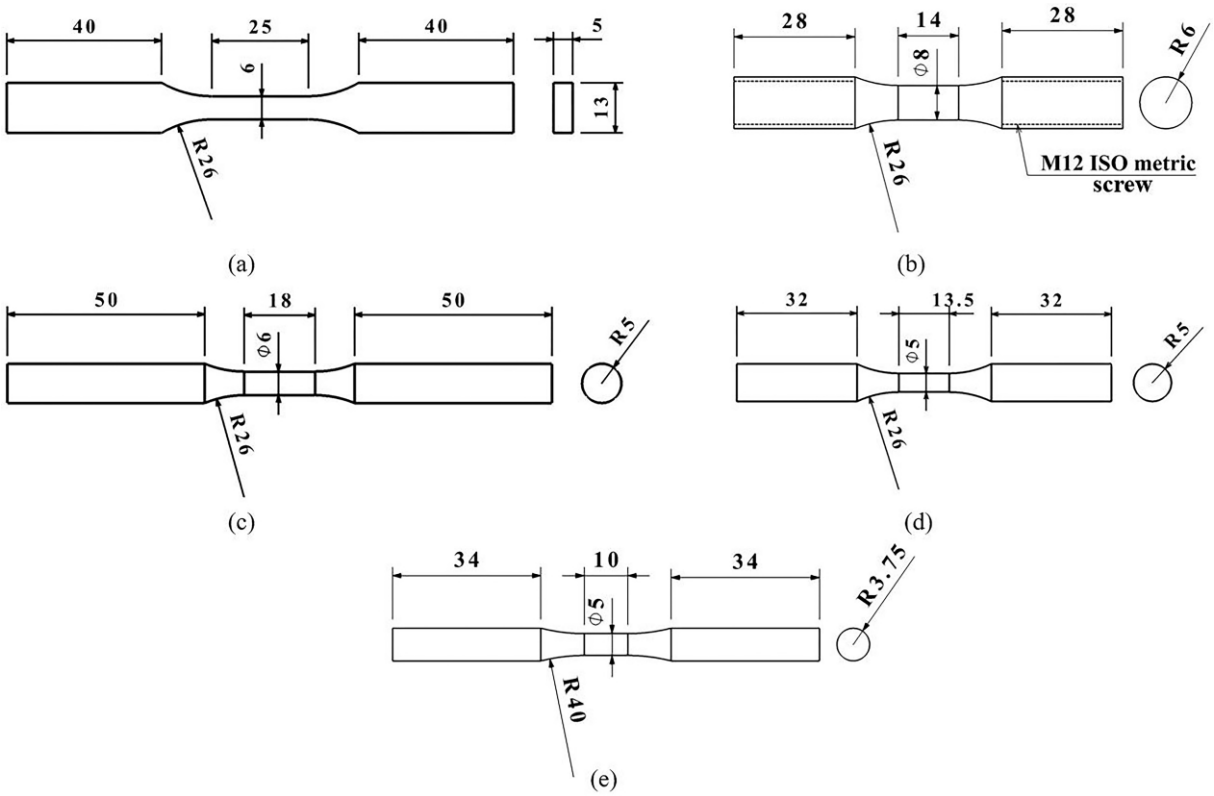

Fig. 4.5 Specimen geometry and dimensions for: (a) tensile test, (b) cyclic stress-strain test $(\sigma - \varepsilon)$, (c) porosity fatigue test, (d) reference fatigue test and (e) interrupted-fatigue tomography test.

4.4.3 Fatigue test

Fatigue test specimens were machined according to ASTM E466 standard from the porosity and reference walls as shown in Fig. 4.5(c) and Fig. 4.5(d) respectively. The cylindrical specimens were polished at the gauge section with 600, 1200, 2500 and 4000 grit papers to achieve a final surface roughness of 0.5±0.1 μm. Fatigue tests were conducted with a 100 kN Instron servo-hydraulic test machine. Load controlled test was performed at a stress ratio of 0.1, frequency of 50 Hz and at laboratory temperature condition.

4.4.4 Interrupted fatigue-tomography test

Load controlled fatigue test specimens were extracted from the porosity wall in vertical orientation with respect to the build direction and machined according to ASTM E466 standard as shown in Fig. 4.5(e). The first specimen was subjected to interrupted fatigue test with six X-ray CT measurements taken at every stop during the fatigue test, while the remaining two specimens were scanned before the start of the test and followed by fatigue cycling till failure. The interrupted fatigue test set-up consisted of two units: a 50 kN load controlled fatigue test unit of Shimadzu and an X-ray CT scanning unit (X TH 160 system, Nikon Metrology). The entire gauge section (dia. 5 mm and length 10 mm) of the specimen was scanned by the X-ray CT to map the initial porosity distribution. The specimen was then fatigue tested at an applied stress amplitude of 315 MPa, stress ratio of 0.1 and frequency of 20 Hz for 2×10^4 cycles. At this point the fatigue test was interrupted to perform X-ray CT scanning, following which the fatigue test was resumed. Subsequent fatigue tests were interrupted at every few thousand cycles to perform X-ray CT scans.

Chapter 5

Experimental Test Results

5.1 Introduction

This chapter presents the findings from the experimental studies conducted with (1) reference group specimens, built according to the standard manufacturing procedure using clean wire and optimised processing parameters, and (2) porosity group specimens, built with contaminated wires and the same process parameters as used in the reference group, to represent the feedstock contamination.

5.2 Material characterisation

5.2.1 Microstructural analysis

(a) α and β grain morphology: Owing to the directional solidification, the prior β grains grow epitaxially in the build direction with lengths ranging from a few 100 microns to the entire length of the wall as shown in Fig. 5.1(a). The prior β grains are about 1 to 3 mm wide, which is much larger than the prior β grain widths reported in selective laser melting and electron beam melting processes [5, 61, 52]. Fig. 5.1(b) is the enlarged view of a prior β grain showing the variation in α phase morphology at the prior β grain boundary (Fig. 5.1c), away from prior β grain boundary (Fig. 5.1d) and at the intersection of each layer with the next layer (Fig. 5.1e). According to [56], grain boundary α forms at the prior β grain boundary and there is a preferred orientation relationship between the grain boundary α and the adjacent β grain (<0001>α parallel to <110>β). Therefore, the preferred orientation relationship at the prior β grain boundary leads to the formation of lamellar α colonies of 20-30 μm width. In Fig. 5.1(d) α phase exhibits a Widmanstätten microstructure away from prior β grain boundary, with an

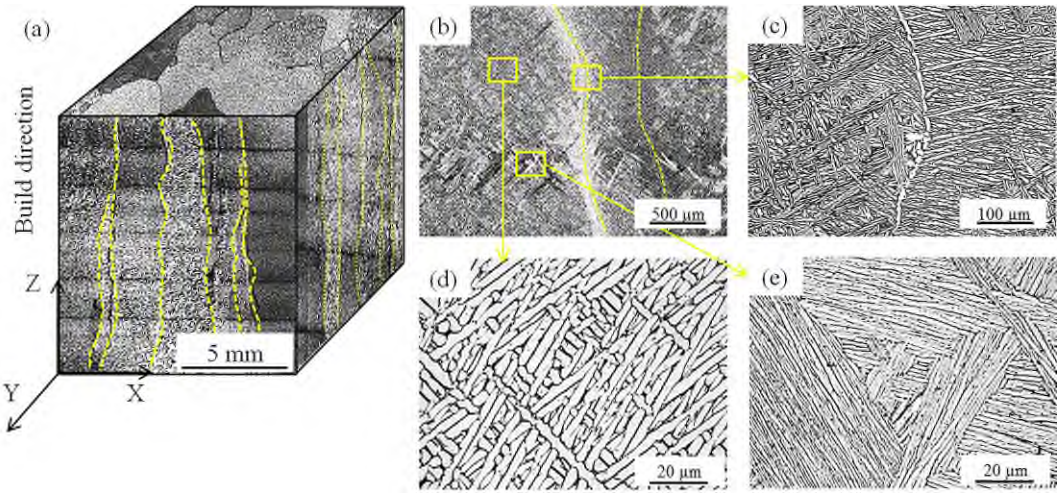

Fig. 5.1 Optical images showing: (a) macrostructure of as-deposited WAAM Ti-6Al-4V, (b) prior β grain boundary, with magnified views: (c) showing lamellar α colonies, (d) Widmanstätten microstructure, (e) dark bands between two layers showing fine lamellar α colonies. Note the different scales in (a) and (b).

average α lath width of 3±0.7 μm. However, at localised regions such as the intersection between two layers (Fig. 5.1e), the average α lath width was reduced to 1±0.2 μm. The reduction in the α lath width at the intersection can be attributed to the higher cooling rate during the deposition of each new layer [14].

It should be mentioned here that the location to location variation in grain morphology was significant in WAAM Ti-6Al-4V, irrespective of the differences in the manufacturing strategy applied for building the two walls i.e the reference wall (deposited with clean wire) and porosity wall (deposited with contaminated wire at the gauge section). In other words, the microstructure observed in the reference and porosity walls were comparable. This is because, the contamination did not change the chemical composition significantly (as reported in Table 4.2) and the primary factors such as process parameters, scan path, etc., which have a greater contribution towards the cooling rate (and hence the microstructural variations) were identical for both the walls.

(b) α grain orientation: EBSD analysis was performed to study the local texture in the α grains since more than 90% of the resulting microstructure was found to be α phase. Inverse pole figure map taken perpendicular to the build direction (showing the cross-section of the columnar prior β grains) showed large α colonies at the prior β grain boundaries as shown in Fig. 5.2(a). Formation of such micro-textured zones was previously reported in literature [56, 58] and attributed to the preferred variant selection of grain boundary α. At regions away from the prior β grain boundary, the texture strength varied from location to location as shown in the Fig. 5.2(b) and 5.2(c). The corresponding pole figure maps are shown in Fig. 5.2(d) and 5.2(e) respectively.

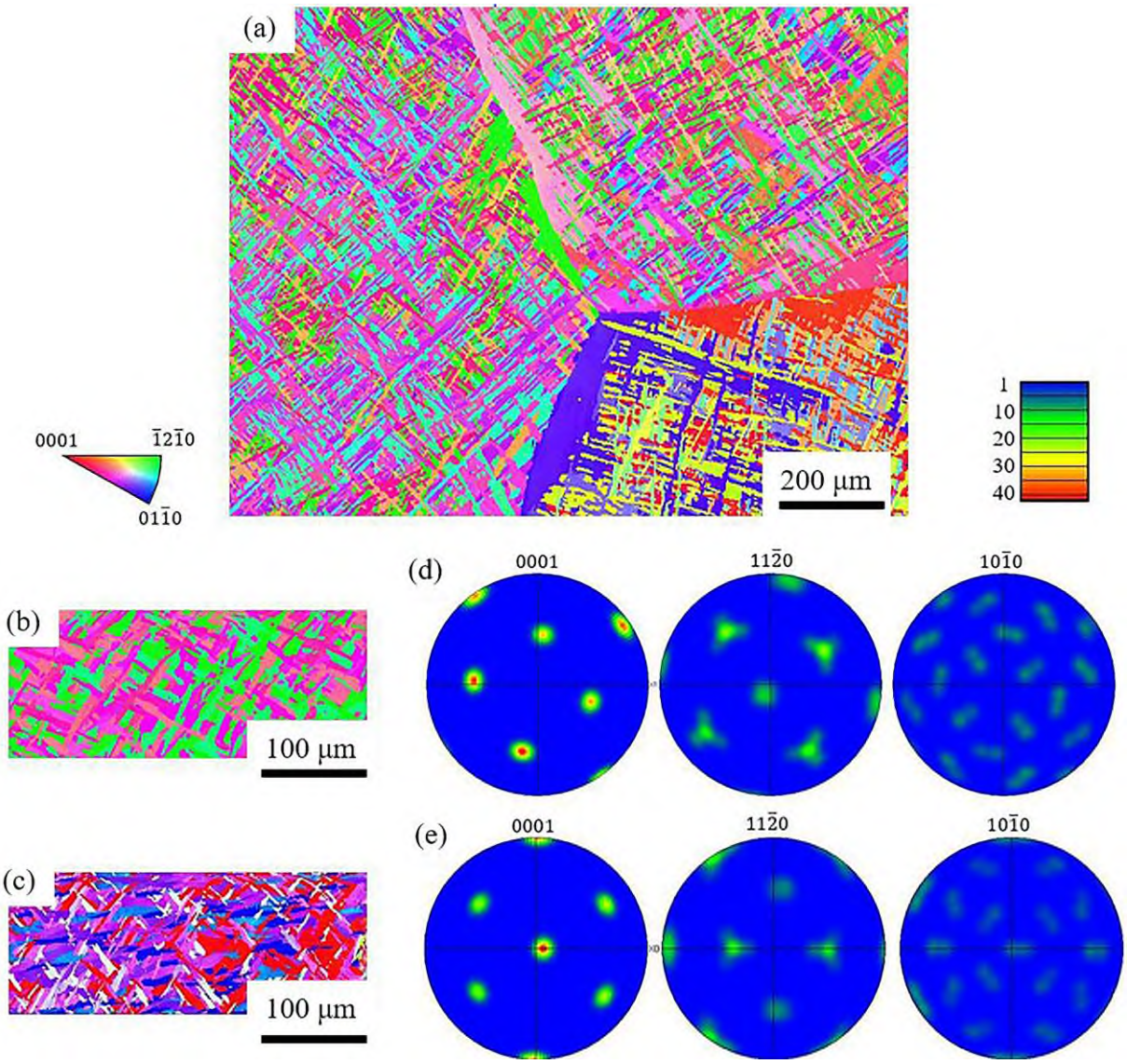

Fig. 5.2 Grain orientation map of WAAM Ti-6Al-4V, (a) inverse pole figure (IPF) perpendicular to the build direction (*Y-X* plane), (b) grains showing weak basal texture, (c) grains with strong basal texture, (d-e) pole figure of (b) and (c) respectively. Colour key for the IPF plots is in the left and that of the pole figures is in the right.

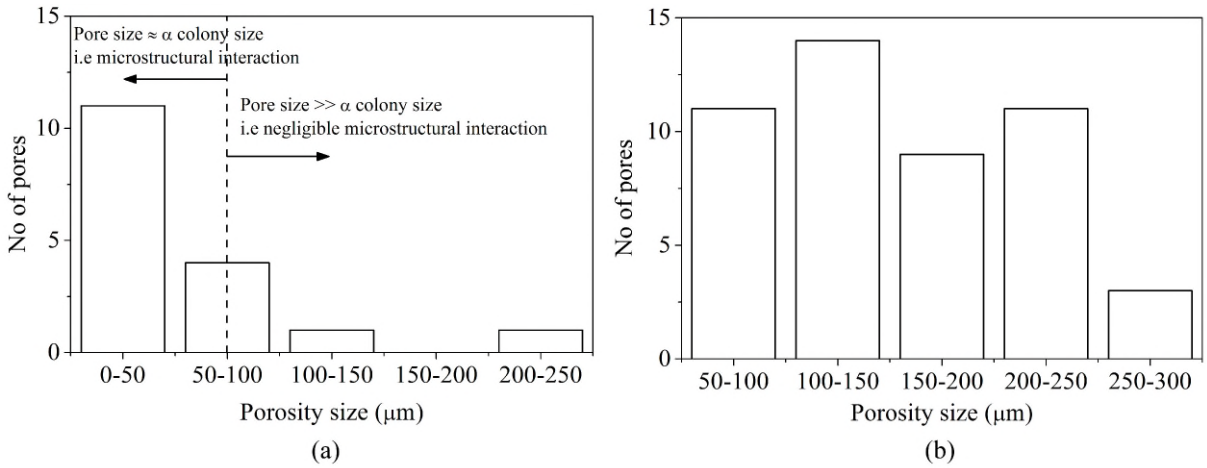

Fig. 5.3 Porosity size distribution in WAAM Ti-6Al-4V: (a) reference wall, (b) porosity wall

5.2.2 Porosity analysis

Porosity distribution in WAAM Ti-6Al-4V (reference and porosity group) was studied using metallography specimens as well as X-ray tomography scans. Fig 5.3 shows the porosity distribution studied from metallography specimens. It was found that the pores are essentially spherical gas pockets of less than 100 μm diameter for the reference specimens ($62 \pm 23\mu$m), while majority of the pore diameters lie between 150 μm to 250 μm in the porosity specimens ($206 \pm 80\mu$m).

Further examination of the size of pore with respect to the surrounding α lamellae width was analysed using etched specimens as shown in Fig. 5.4. Characteristic length is defined as the width of α colony, which is 20 μm to 30 μm for WAAM Ti-6Al-4V and according to [78], when the pore diameter is less than 8 times of the characteristic length, the micro-crack growth will be influenced by the surrounding microstructure. In case of pores larger than 8 times the characteristic length (as in the porosity specimens where the average pore diameter is 200 μm), the pore will behave like a notch and the gross mechanical properties can be used for fatigue life predictions. However, in reference specimens, average porosity diameter (close to 60 μm) is within the characteristic length scale, therefore, local microstructure will affect the crack initiation and initial growth phase.

X-ray CT analysis showed that the three-dimensional geometry of the pores was spherical in both reference and porosity specimens as shown in Fig. 5.4(c) and 5.4(d), which is in agreement with the results reported in literature [14, 66]. Density of the porosity specimens was found to be 99.96% while the reference specimen density was more than 99.99% showing a fully dense microstructure. Distribution of the porosity defects in the reference specimens could not be studied since the porosity sizes in reference specimens were close to the X-ray CT resolution

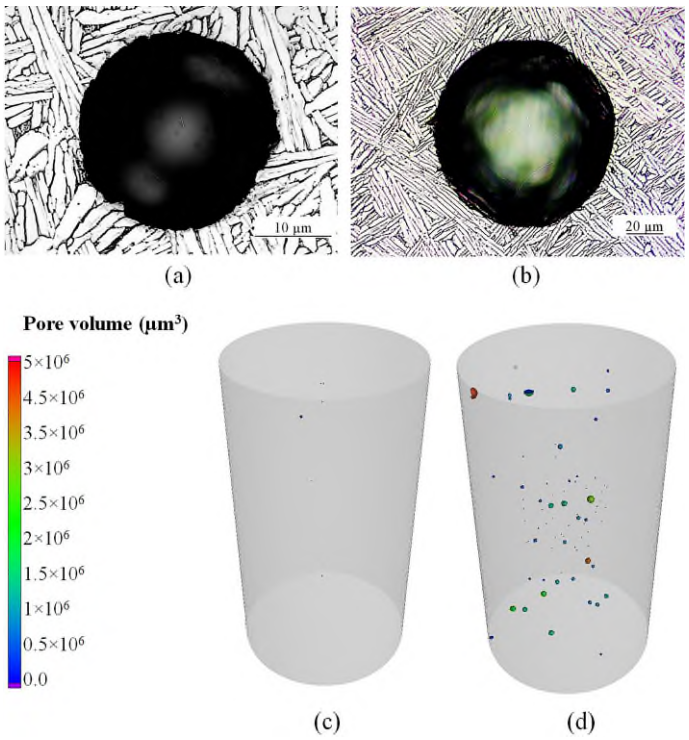

Fig. 5.4 Optical image of representative porosity in (a) reference wall, (b) porosity wall, comparing the size of the α lamellae width with the pore diameter, (c) X-ray computed tomography scan at gauge section of the reference specimen, density is 99.99%, and (d) porosity specimen, density is 99.96%. Note the different scales used in (a) and (b).

limit i.e 40 μm which is approximately twice the voxel size. Defect distribution in the porosity specimens did not show any noticeable change with respect to the distance from the substrate, i.e location did not seem to affect the probability of formation of porosity defect. However, this observation is not representative of the true porosity distribution as the porosity specimens were built with selective contamination at the gauge section. Further investigation of the effects of porosity on the tensile and fatigue performance was conducted using mechanical tests followed by fractography analysis.

5.3 Tensile properties

The tensile test results for the reference and porosity specimens are shown in Fig. 5.5 and the values are provided in Table 5.1. It was observed that the yield strength and ultimate tensile strength were comparable between the two groups. Presence of pores did not change the yield strength because stress concentration at the pores causes localised plastic deformation, while yield strength corresponds to the beginning of gross (bulk material) plastic deformation. In addition, the ultimate tensile strength was also comparable due to the fact that after yielding the stress-strain curve becomes horizontal for Ti-6Al-4V, which results in negligible variation in stress

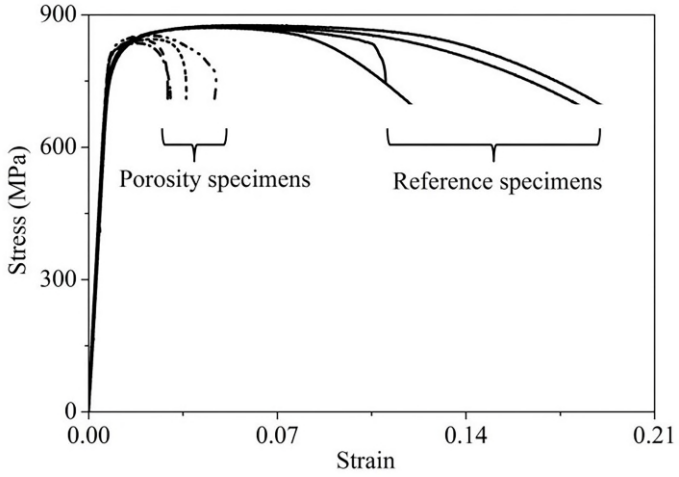

Fig. 5.5 Engineering stress vs. strain relations from tensile test results for the reference (solid lines) and porosity specimens (dotted lines).

Table 5.1 Tensile test results

Group	0.2% offset, σ_{ys} (MPa)	Tensile strength, σ_{uts} (MPa)	Uniform Elongation (%)
Reference	802 ±7	859 ±4	10 ±2
Porosity	825 ±5	842 ±8	4 ±1

with respect to strain and therefore the comparable strength values. However, uniform elongation was significantly lower for the porosity specimens which can be due to the development of micro-cracks in the material at the root of the pores which is constrained by the surrounding material at lower stress.

From the porosity characterisation study presented in section 5.2.2 it was found that reference group specimens may contain porosity defects (refer Fig. 5.3a). Consequently, the ductility of the reference specimens showed a significant scatter.

The tensile fracture surfaces of a reference specimen and porosity specimen are shown in Fig. 5.6(a) and Fig. 5.6(b) respectively. Dimples were observed in both the cases as shown by enlarged views in Fig. 5.6(c) and Fig. 5.6(d), thereby indicating a ductile fracture. However, the sizes of dimples in the reference specimens (Fig. 5.6c) were significantly smaller than that in porosity specimens (Fig. 5.6d). The dimple size difference can be due to higher elongation in the reference specimens which deforms (pulls) the grains resulting in the ruptured grains (manifested as dimples) having a smaller cross-section on the fracture surface, whereas the porosity specimens undergo lower elongation and the grains are not deformed as much and therefore the dimples are comparatively larger [114].

5.4 Cyclic stress-strain relationship

The cyclic constitutive relationship of WAAM Ti-6Al-4V was obtained from the displacement controlled cyclic load test. The changes in the cyclic deformation behaviour was more pronounced for the initial 20 cycles as shown in Fig. 5.7(a), due to the rearrangement of the dislocation substructure [106]. Subsequently, the material stabilises and the stress vs. strain response at this stage can be used to represent the steady state cyclic deformation behaviour of the material (or stabilised hysteresis loop). The material showed cyclic hardening behaviour for the first 3 to 4 cycles, followed by cyclic softening response for the remaining test cycles. This behaviour can be attributed to the lamellar morphology of the α grains (present in colony and Widmanstätten arrangement) which have been reported to cause initial hardening effect [115]. It was also observed that the extent of softening in WAAM Ti-6Al-4V was less than the softening reported for selective laser melting [5, 17] and wrought Ti-6Al-4V [103, 102]. This is because cyclic softening is primarily due to the plastic deformation in the soft α phase, however, the lamellar morphology of the α grains and the surrounding hard β matrix assist in pinning down the movement of dislocations [115] thereby resulting in only 5% to 6% reduction in the peak stress (softening) with increase in number of cycles.

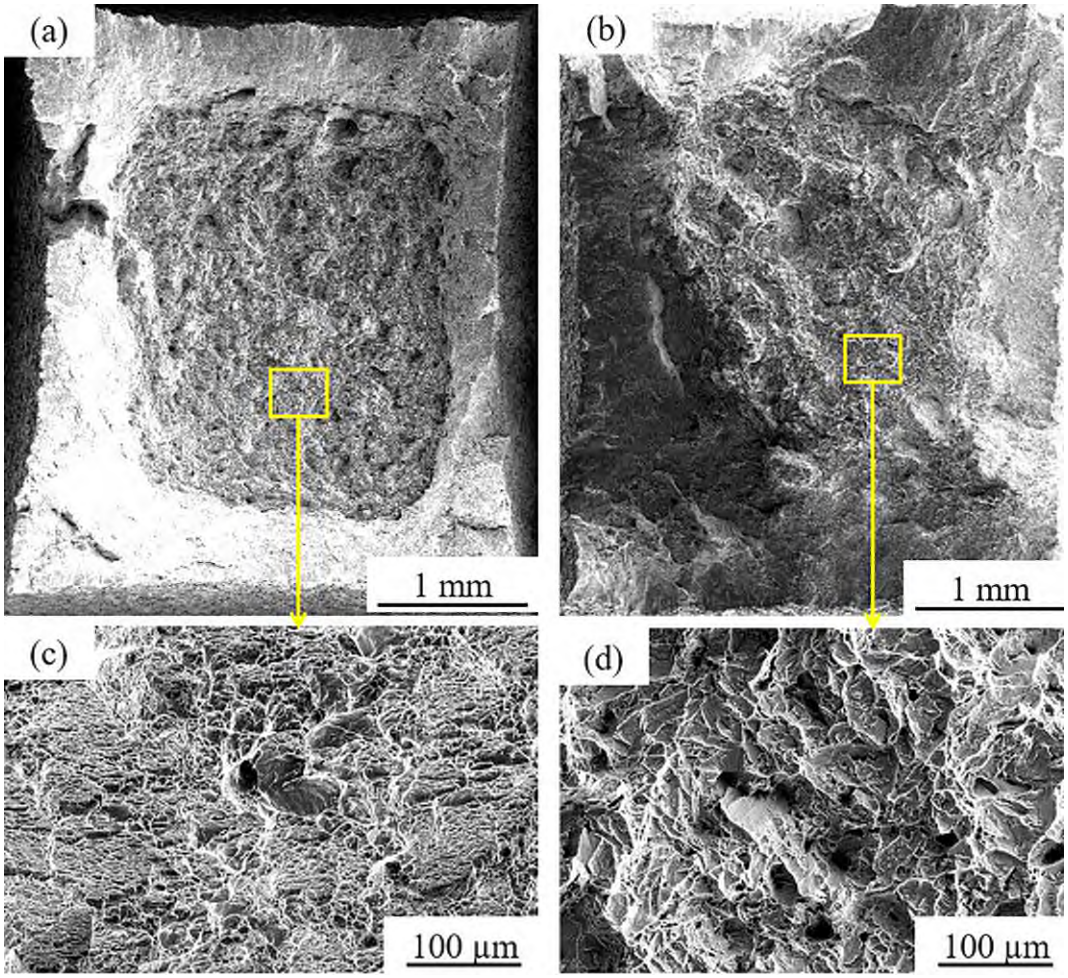

Fig. 5.6 Tensile fracture surfaces, (a) reference, (b) porosity, (c) and (d) enlarged views of (a) and (b) to show the difference in the dimple sizes.

The stabilised cyclic stress-strain response, i.e hysteresis loops are shown in Fig. 5.7(b) and the stabilised cyclic stress-strain curve is shown in 5.7(c). The material showed cyclic softening in comparison to the monotonic stress-strain curve [85]. The cyclic stress vs. plastic strain plot was used to determine the material constants in the Ramberg-Osgood relationship as shown in Eq. 3.1. The coefficient and slope of the best-fit curve gives the cyclic strength coefficient and cyclic strain hardening exponent respectively. The cyclic material property values are given in Table 5.2. It should be mentioned that the engineering stress and strain values were used instead of the true stress and strain values because cyclic hysteresis loops were measured at low strain levels (up to 2%) where the difference between true and engineering values is negligible [107].

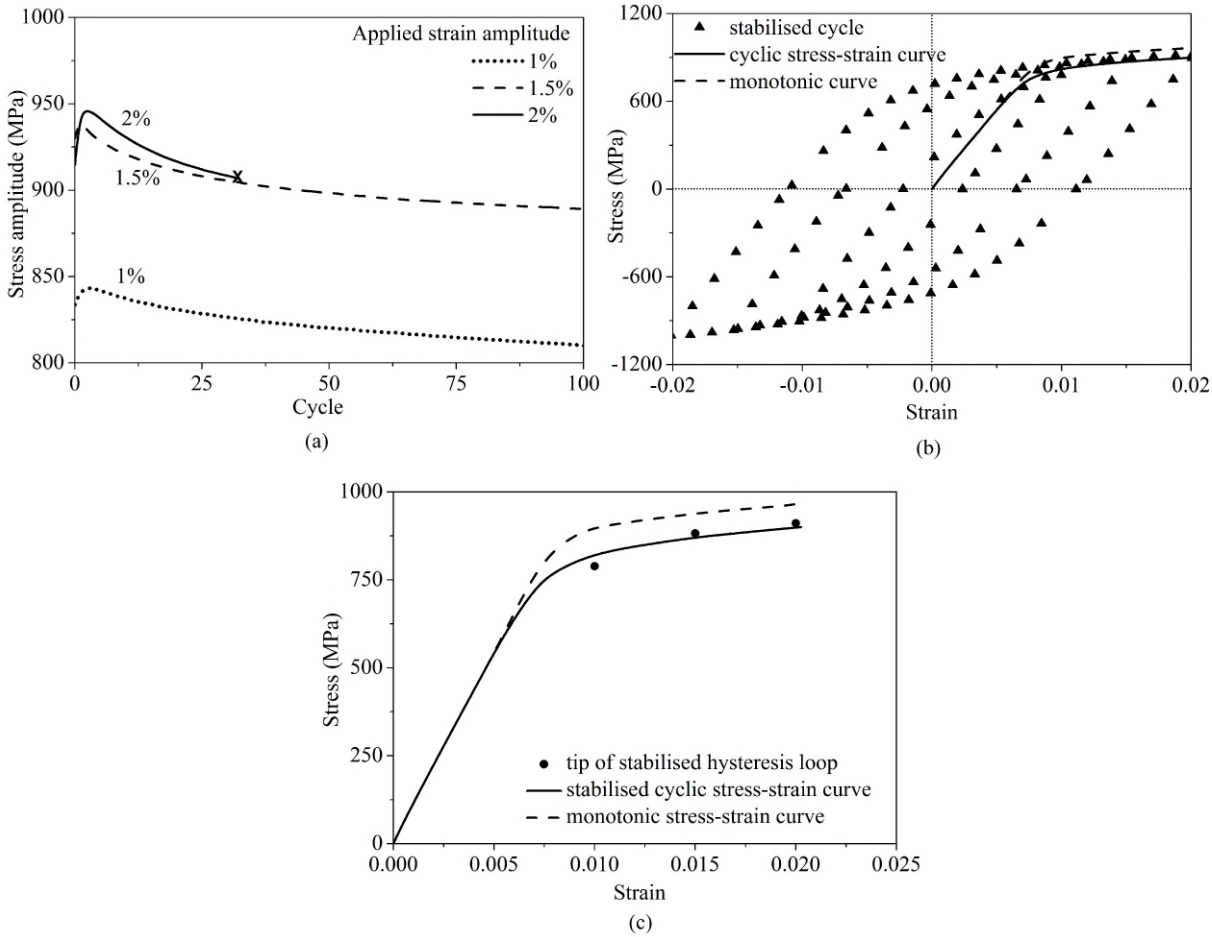

Fig. 5.7 (a) Cyclic softening behaviour, (b) stabilised hysteresis loops of WAAM Ti-6Al-4V at 1%, 1.5% and 2% fully reversed applied strain amplitude, (c) stabilised cyclic stress-strain curve obtained by joining the tip of the stabilised hysteresis loops.

Table 5.2 Cyclic properties of WAAM Ti-6Al-4V

Modulus of elasticity, E (GPa)	Cyclic strength coefficient K' (MPa)	Strain hardening exponent n'	Fatigue strength coefficient σ_f' (MPa)	Fatigue strength exponent b
116	1582	0.125	1470	-0.068

5.5 Fatigue test results

It is known that in high cycle fatigue regime, the total life of a coupon fatigue specimen is essentially the crack initiation phase, while in low cycle fatigue regime, micro-cracks nucleate within few loading cycles due to the high stress level, and therefore the total life is dominated by the crack propagation phase. Fig. 5.8 shows the fatigue test results obtained from the reference and porosity specimens. It was found that the scatter in the porosity specimen tests

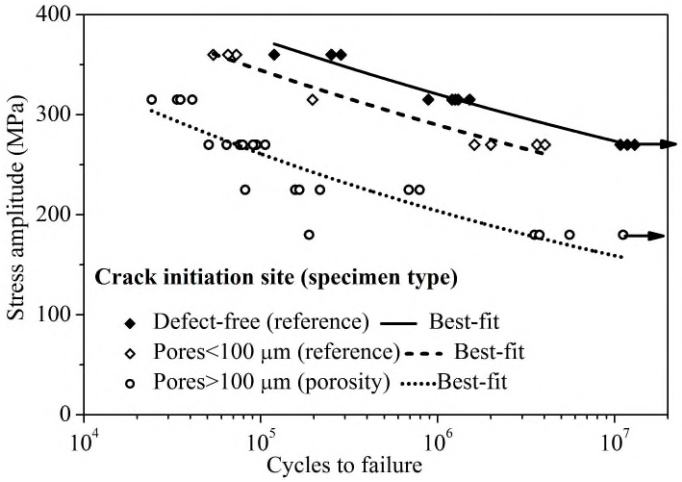

Fig. 5.8 Fatigue test results with information from the fracture surface analysis. Three distinct S-N curves were identified depending on the crack initiation site and pore size.

was significantly reduced for applied stress amplitudes of 270 MPa and above. The reason for this behaviour can be the local yielding that takes place at the pore root, leading to micro-crack nucleation within a few loading cycles. Following this, the pore and the micro-crack collectively contribute towards the effective crack size. Given the larger pore diameter in the porosity specimens, a stress level of 270 MPa is high enough to cause the crack to grow unhindered, leading to limited scatter in the fatigue life. However, in reference specimens, the micron sized pores coupled with the micro-crack, tend to remain within the size-scale of the surrounding microstructure, thereby leading to an extended short crack growth phase. This phase causes significant variation in the fatigue life owing to microstructural interactions (the micro-crack deflects from grain to grain while seeking the easy slip planes), thereby resulting in higher scatter in the fatigue life of the reference specimens.

Fracture surface examination was performed to elucidate the differences among the three S-N curves (Fig. 5.8); the S-N behaviour (relation) depends on whether the crack was initiated at microstructural features (no pores), at porosity of diameter comparable to α colony width (pore diameters below 100 μm), or at porosity of diameter much larger than the α colony width (pore diameters above 100 μm). The fatigue strength of porosity specimens was reduced by a factor of 1.5 (at fatigue life of 10^7 cycles) as compared to the defect-free reference specimens.

The best-fit curves were expressed in terms of the Basquin's equation (Eq. 5.1) using a double log scale, the value of constants (σ_f, b) was $(827 \pm 47, -0.068 \pm 0.004)$ for defect-free reference specimens, $(818 \pm 60, -0.075 \pm 0.005)$ for the reference specimens with crack initiation at pores below 100 μm diameter, and $(899 \pm 142, -0.107 \pm 0.01)$ for the porosity specimens with crack initiation at pores greater than 100 μm diameter.

$$\sigma_a = \sigma_f'(2N_f)^b \tag{5.1}$$

where σ_a is the applied stress amplitude, σ_f' the fatigue strength coefficient, $2N_f$ the cycles to failure and b the fatigue strength exponent.

Fig. 5.9 shows the fracture surface of two specimens tested at the same loading conditions. The measured diameter of the crack initiating pore in Fig. 5.9 (a-c) was comparable to the microstructure size while the crack initiating pore diameter in Fig. 5.9 (d-f) was significantly larger than the microstructure. Depending on the porosity size, the crack initiation and growth shows transgranular cleavage as shown in Fig. 5.9 (c) for the specimen with smaller porosity (dia. $<$ 100 µm) and intergranular facets for the specimen with larger porosity (dia. $>$ 200 µm) as shown in Fig. 5.9 (f). Therefore, the higher fatigue life for the specimen with porosity size comparable to the characteristic length of the microstructure (width of lamellar α colony [91]) was due to interaction of the pore with the microstructure. It is worth to mention that the specimen with smaller porosity was from the reference group while the larger porosity specimen was from porosity group.

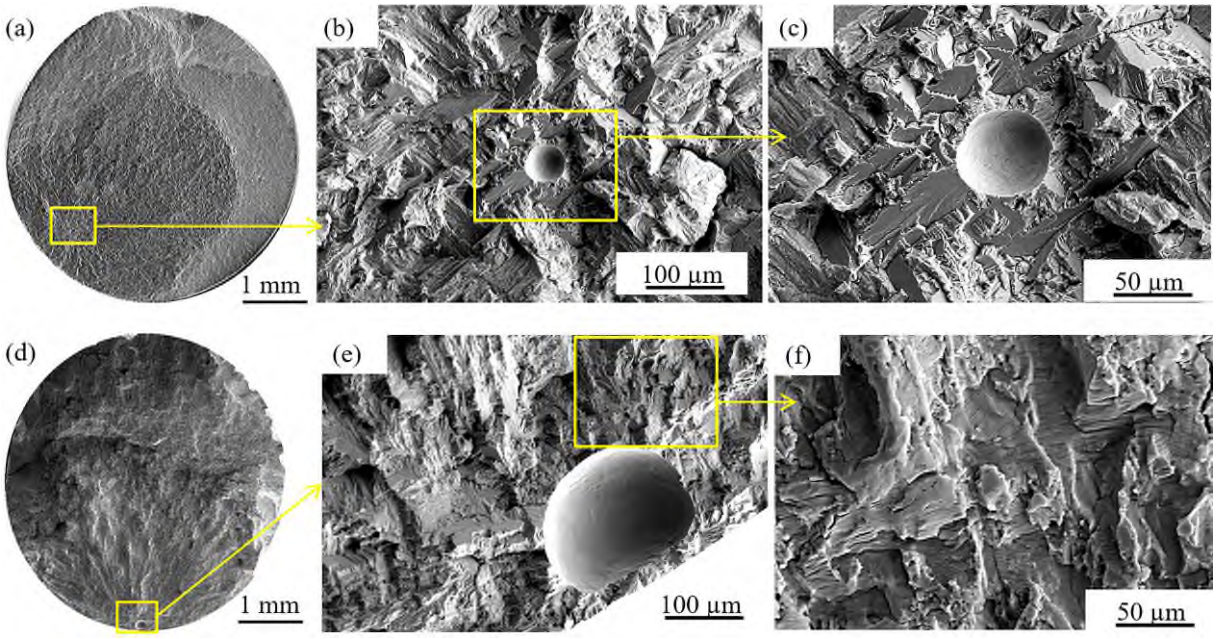

Fig. 5.9 Effect of porosity diameter on fatigue fracture behaviour; (a-c) initial porosity diameter ($d_0 = 58\mu$m) is comparable to surrounding α colony size, $N = 8.8 \times 10^5$ cycles, (d-f) initial porosity diameter ($d_0 = 220\mu$m) is much larger than surrounding α colony size, $N = 3.3 \times 10^4$ cycles. Both specimens were tested at applied stress amplitude of 315 MPa, stress ratio 0.1.

Fatigue life was found to be lowest when multiple pores were present within a distance less than the diameter of the larger pore as shown in Fig. 5.10(a). Proximity of the pore to the free surface was found to be the next most damaging characteristic of a pore. Sub-surface location

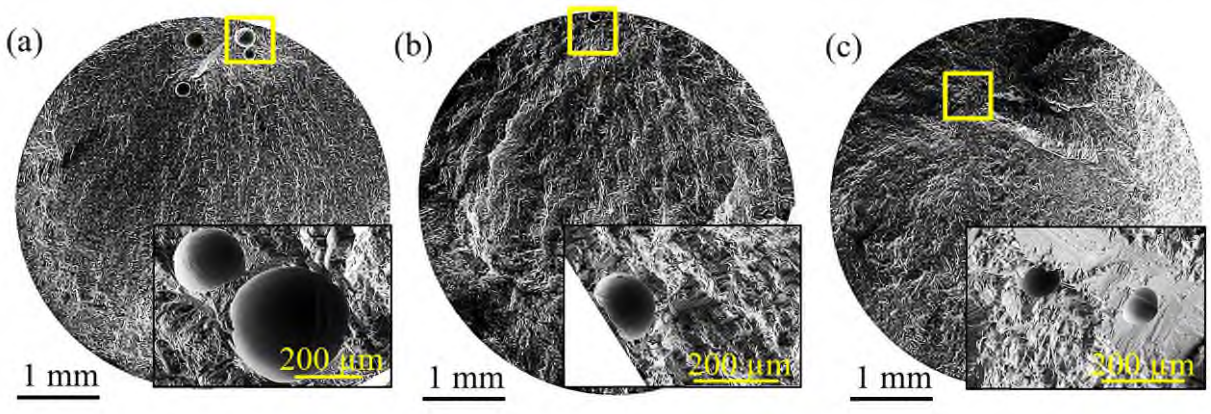

Fig. 5.10 Overall fracture surface with magnified view (bottom right corner) of crack initiation site: (a) multiple pores at close proximity, $d_0 = 320\mu$m, 197 μm, $N = 1.87 \times 10^5$ cycles, (b) sub-surface pore, $d_0 = 190\mu$m, $N = 1.19 \times 10^6$ cycles, (c) internal pore, $d_0 = 113\mu$m, 93 μm, $N = 5.57 \times 10^6$ cycles. All three specimens were tested at applied stress amplitude of 180 MPa, stress ratio 0.1.

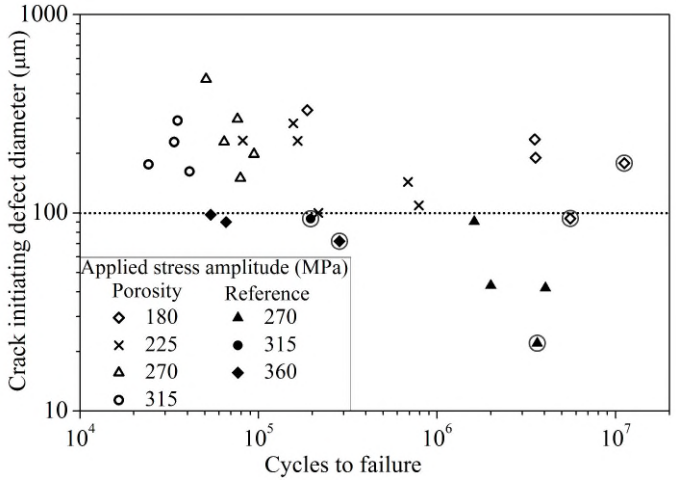

Fig. 5.11 Crack initiating pore diameter for reference and porosity specimens showing no correlation between the defect size (pore diameter) and the fatigue life under various applied stress amplitudes. Note: encircled data points denote crack initiation at internal pores.

(Fig. 5.10b) reduced the fatigue life by a factor of four as compared to the internal location (Fig. 5.10c). Additionally, it was observed that 5 specimens had crack initiation at surface defects, 18 at sub-surface defects, 5 at internal defects and the remaining at microstructural features (defect-free). Therefore, sub-surface location was found to be the most critical characteristic, as approximately 65% of the cracks initiated at subsurface pores. Fig. 5.11 presents the results for the crack initiating porosity diameter vs. fatigue life. It can be observed that the pores in the reference specimens were predominantly less than 100 μm in diameter. However, the scatter in the results indicates that in addition to porosity size, the applied stress should also be considered.

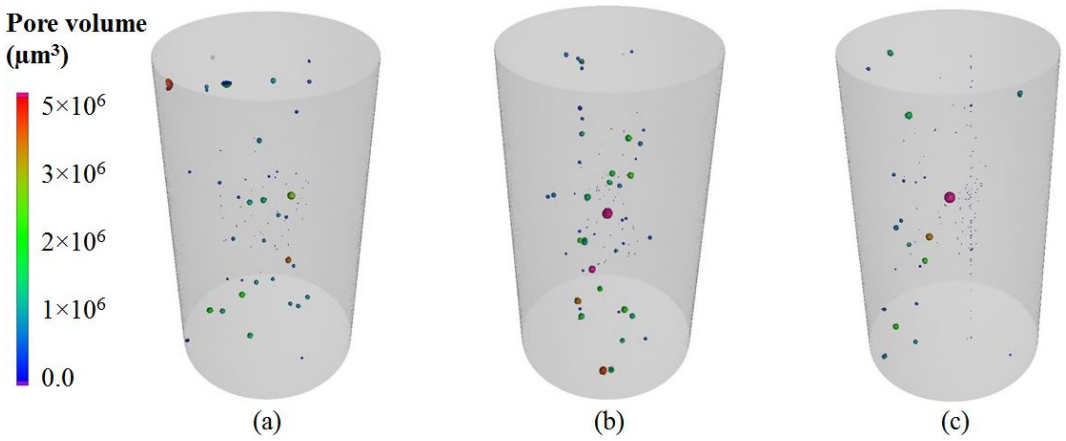

Fig. 5.12 X-ray CT scans before fatigue test: (a) specimen 1 (used for interrupted fatigue-tomography test), (b-c) specimen 2 and 3 (used for S-N test).

5.6 Interrupted fatigue-tomography testing

Porosity size and distribution plays an important role in fatigue life, particularly when pore sizes are larger than the surrounding microstructural dimensions. Therefore, the initial spatial distribution of the pores was obtained from X-ray CT scanning. The porosity density in all the specimens was 0.04±0.005%. All the observed pores had a spherical geometry with pore diameter ranging between 40 μm and 250 μm as shown in Fig. 5.12. In terms of location, pores could be observed in surface, sub-surface and internal locations. It is worth mentioning that in some cases the X-ray CT measurement can include additional features close to the resolution limit, such as the scattered dots in Fig. 5.12(c). Due to the uncertainty of such measurements, the data points were treated as artifacts in this study and excluded while performing porosity density calculations.

Subsequent growth of pores was confirmed from the results of the interrupted fatigue-tomography test results as shown in Fig. 5.13(a). Porosity growth was observed between every scan, with the maximum growth seen between 2×10^4 cycles and 2.8×10^4 cycles which is 65%-85% of the total fatigue life of the specimen. This can be due to the high stress region at the pore root ($K_t \geq 2.08$) which undergoes localised plastic deformation. Slip lines, which are a manifestation of cyclic plastic deformation, were observed on one of the specimens where the crack initiation site (Fig. 5.13b) showed persistent slip bands on the pore surface near the mid riff region (which is close to the stress concentration region) as shown in Fig. 5.13(c). In addition to being a stress raiser, pores also provide free surface for the dislocations to pile up [77], which causes the material to move away from the pore surface and therefore can lead to an increase in the pore diameter. Fig. 5.14(a-c) show the changes in the pore morphology with fatigue loading cycles.

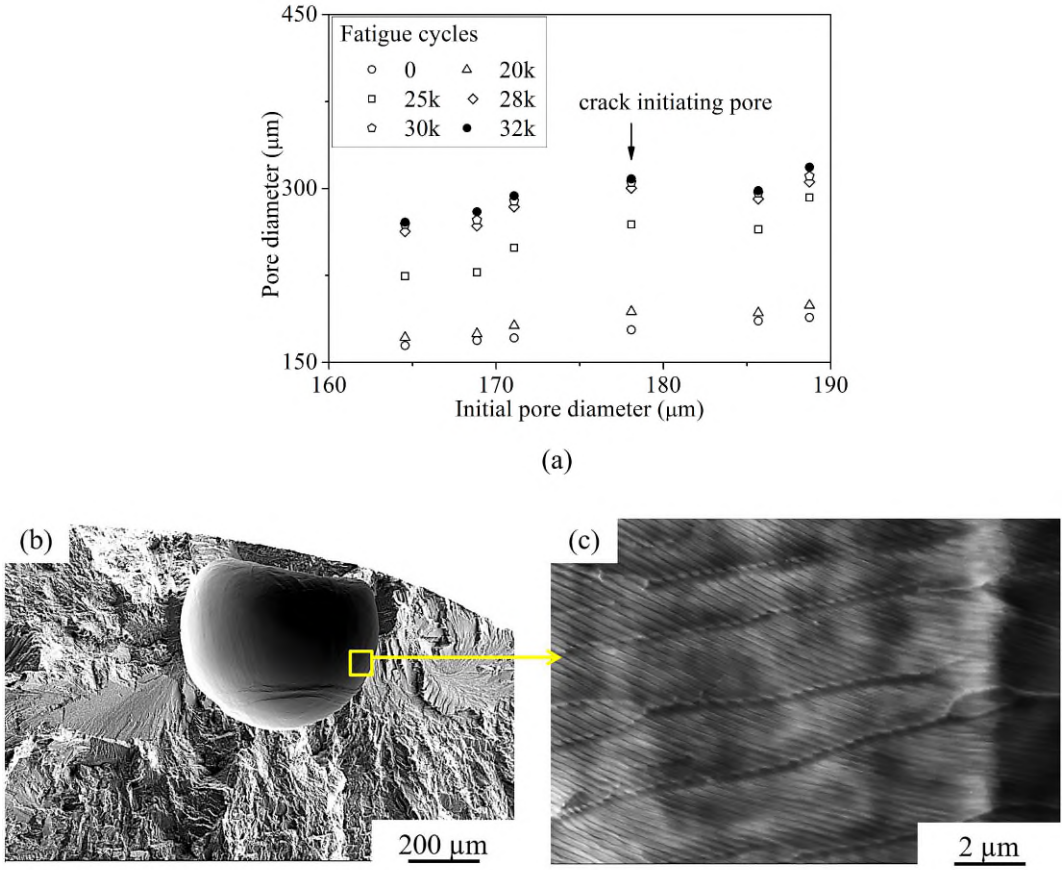

Fig. 5.13 (a) Increase in porosity diameter with fatigue cycles, (b) crack initiation at a pore (applied stress amplitude 315 MPa, stress ratio 0.1, fatigue life 2.46×10^4 cycles), (c) enlarged image of the pore surface showing slip lines which indicates dislocation pile-up and hence fatigue damage.

Due to pore growth, the pores located initially at sub-surface sites, tend to open to the free surface of the specimen. It was observed that fatigue crack was initiated from more than one pores at 70%-80% of the fatigue failure life of the specimen. Since the tomography scans were taken at unloaded condition, it was difficult to image the entire crack. Fig. 5.15 shows that tortuous cracks originated preferentially at sub-surface pores in comparison to internal pores and grow towards the free surface of the specimen. The location of the cracks were found to be at the mid-riff section of the pores. This can be explained by the higher value (25%) of stress concentration factor for sub-surface pores.

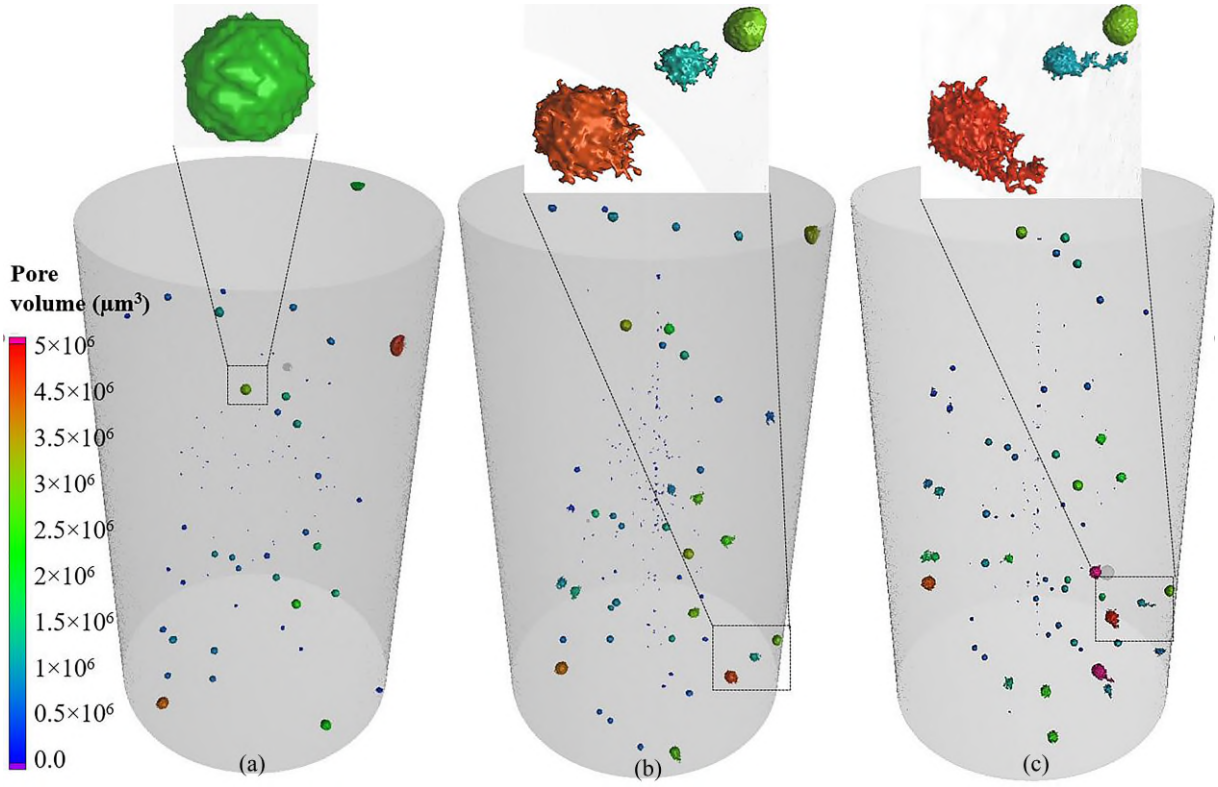

Fig. 5.14 Three dimensional view of X-ray CT scans of Specimen-1, showing the changes in pore morphology with accumulated fatigue cycles (N): (a) N= 0, (b) N= 2.5×10^4, (c) N= 3.2×10^4 (specimen failed at 32380 cycles).

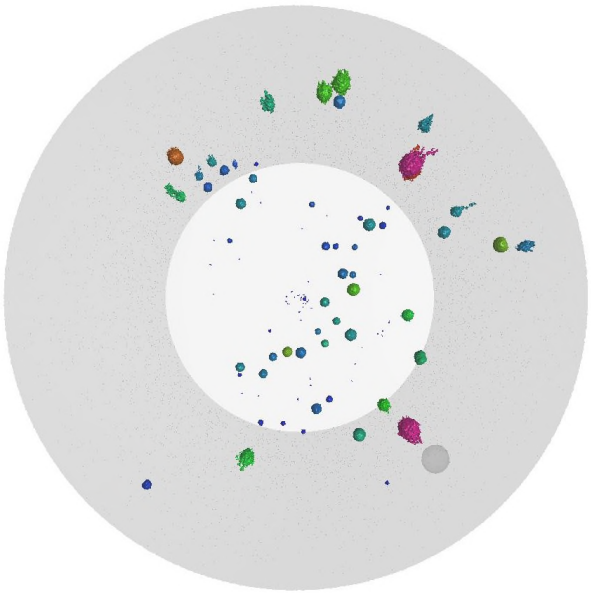

Fig. 5.15 X-ray CT image of the top view of Specimen-1 gauge section at 3.2×10^4 cycles, showing the tortuous cracks emerging from the near surface defects and growing towards the free surface. Note: scale bar shown in Fig. 5.14 is applicable.

All the specimens showed crack initiation at isolated spherical pores located on the free surface of the specimen as shown in Fig. 5.16(a-c). It was found that the critical sub-surface pores identified in the initial X-ray CT scan had been transformed into surface pores. This

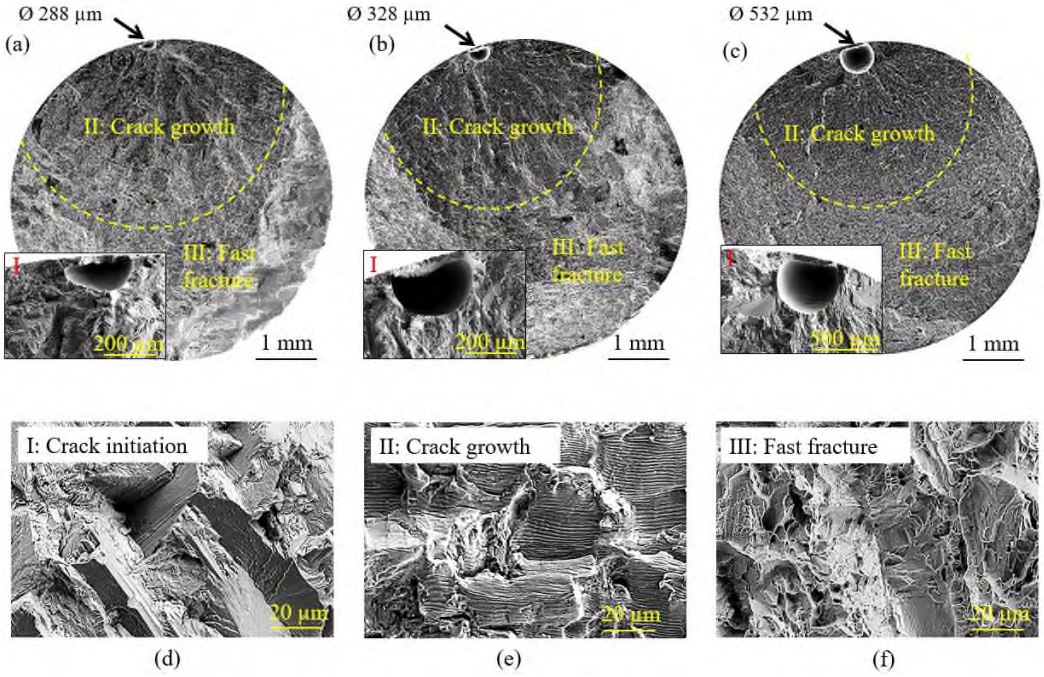

Fig. 5.16 SEM image of fatigue fracture surface of: (a) Specimen 1, (b) Specimen 2, (c) Specimen 3, with enlarged view of the crack initiating pore at bottom left corner (note the different scale bars in the enlarged porosity image), crack path morphology at: (d) initiation region (transgranular facets), (d) rapid crack growth region (striations) and (e) fast or final fracture region (dimples).

is due to the collapse of the tiny ligament of material between the pore and the free surface [87]. The fatigue fracture surface was characterised by three distinct regions, (i) crack initiation and short crack growth region (within 0.5mm to 1mm radius around the gas pore) visualised as transgranular facets as shown in Fig. 5.16(d), (ii) rapid crack growth region which showed ductile striations as shown in Fig. 5.16(e), and the final fracture region which was characterised by a dimple fracture behaviour as shown in Fig. 5.16(f). The crack initiating pore from the SEM image of the fracture surface was traced back to the initial X-ray tomography scan taken during the porosity characterisation studies presented in Fig. 5.12 (before application of fatigue loading). The crack initiating pore diameter measured from the fracture surface image was found to be approximately twice the pore diameter measured from the initial X-ray CT scan data.

5.7 Summary

Two groups of wire + arc additive manufactured titanium alloy (WAAM Ti-6Al-4V) were fabricated and tested to study the material performance of the reference group (manufactured with clean wire) and porosity group specimens (manufactured with contaminated wire at the specimen gauge section). The findings can be summarised as the following:

(1) The microstructure of both groups was similar and consisted of epitaxial prior β grains aligned along the build direction. The α phase exhibited Widmanstätten and lamellar colony morphology with an average α lath width of 3 μm and α colony width of 20-30 μm. Average gas pore diameter was 60 μm for the reference group and 200 μm for the porosity group.

(2) The material did not exhibit any distinct texture except at the prior β grain boundaries where the growth of primary α selectively underwent growth in specific orientations to maintain the Burgers orientation relationship with the adjacent β phase.

(3) Fatigue strength ($\Delta\sigma$) was found to be 540 MPa and 360 MPa respectively for the reference specimens and porosity specimens. The tensile properties were comparable for the two groups, except for the uniform elongation (elongation up to necking), which was 10% and 4% for the reference and porosity specimens respectively.

(4) The 10 largest pores in the gauge section were found to almost double in size with increase in number of cycles. Rapid increase in pore diameter was observed between 65-85% of the total fatigue life of the specimen. Presence of fine slip lines on the pore surface indicated that the pores act as free surfaces for the accumulation of dislocations and hence undergo growth during fatigue loading.

Chapter 6

Finite Element Modelling and Fatigue Life Prediction

6.1 Introduction

Studies on selective laser melted Ti-6Al-4V [61, 10], electron beam melted Ti-6Al-4V [66, 52] and wire arc additive manufactured Ti-6Al-4V [14, 42] have shown that the primary cause for the inferior fatigue performance of additive manufactured (AM) materials can be attributed to porosity defects. While few studies have been carried out to understand the percentage reduction in the fatigue strength of AM Ti-6Al-4V by the presence of porosity [66, 87], there has been no studies on the fatigue life prediction of wire + arc additive manufactured titanium alloy (WAAM Ti-6Al-4V). Therefore, this chapter presents a mechanistic approach to quantify the influence of location and shape of gas pores on the fatigue life of WAAM Ti-6Al-4V. Finite element (FE) analysis is a powerful tool that can be used to determine the local stress and strain at complex geometrical features (i.e porosity defects). Hence, FE models were used to calculate the local stress and strain acting at the pore root and eventually applied in stress-life (for low values of applied stress) or strain-life (for high values of applied stress) relationship to perform fatigue life prediction.

6.2 Modelled pore geometries

The metallography and X-ray computed tomography (X-ray CT) results presented in Section 5.2.2 have shown that the gas pores frequently exhibit a spherical or near spherical morphology. Fig. 6.1 illustrates the pore geometries that have been modelled in this work where Fig. 6.1(a)

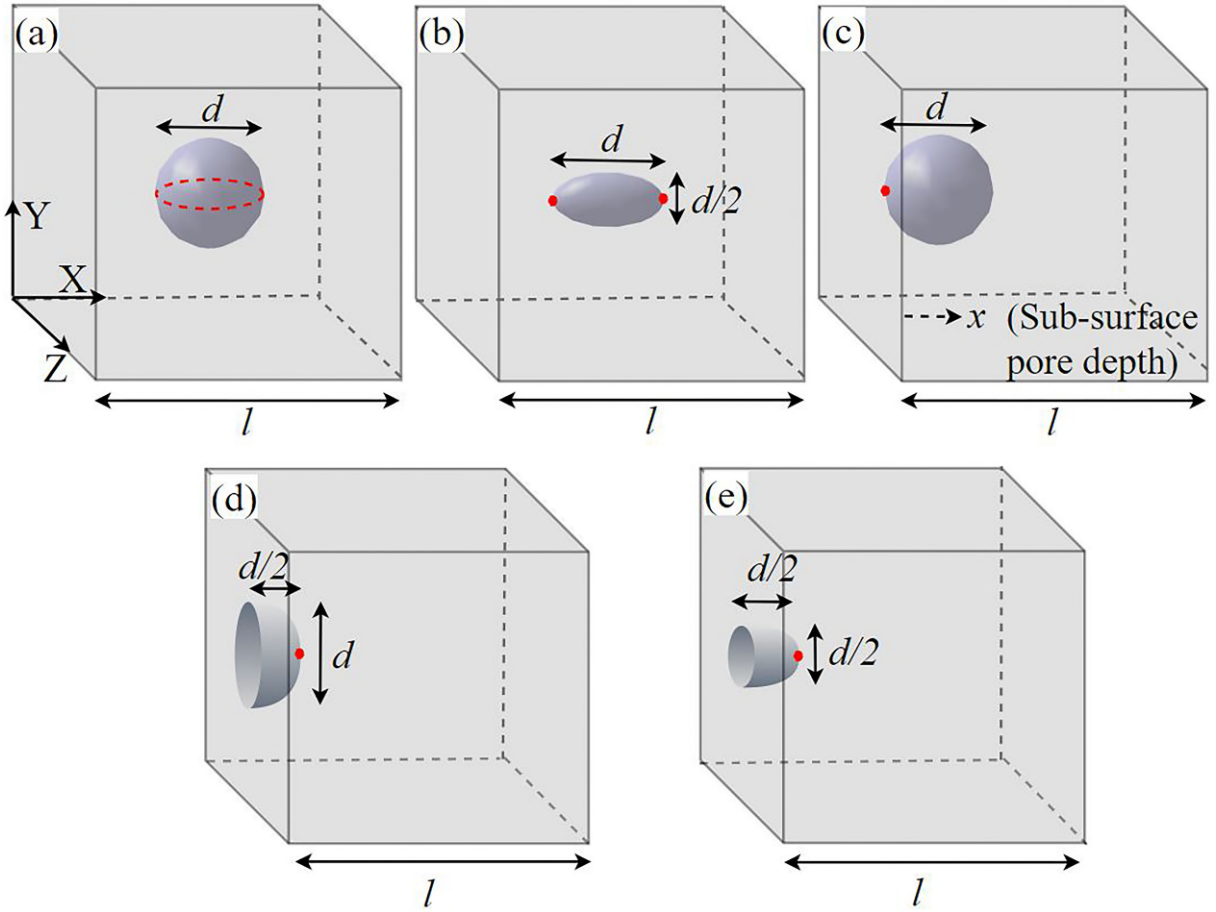

Fig. 6.1 Sketch of the model with one of the following pore geometries, as used for FE modelling, (a) internal spherical, (b) internal oval, (c) subsurface spherical (x is the distance between the pore edge and nearest free surface), (d) surface hemispherical, (e) surface oval. Stress was applied on the Z-X plane and the red marks indicate the pore root where stress concentration was calculated.

corresponds to the internal spherical pore geometry. To understand a more critical condition, in addition to the spherical geometry an oval geometry was also included in the study as shown in Fig. 6.1(b). The ratio of the major diameter of the pore to the minor diameter is defined as aspect ratio and for an oval pore its value is 2. Further, the location effect on near surface pores was analysed by modelling a spherical pore placed at varying distances from the free surface as shown in Fig. 6.1(c). It should be noted that this model was also for pores that are within the bulk material. The extreme limit of the porosity location was modelled with the pore exposed to the free surface, as shown in Fig. 6.1(d) and Fig. 6.1(e) that shows the spherical and oval pores respectively placed on the free surface of the model. This condition may be encountered when surface machining of the AM part brings the sub-surface spherical or oval pores to the free surface. These pore geometries broadly include all the possible shape and location combinations for isolated gas pores.

6.3 Linear elastic stress analysis

6.3.1 Assumed pore geometry

Internal pores of spherical and oval geometries have been modelled using a 1/8 model owing to the three planes of symmetry while the subsurface spherical pores and surface pores have been modelled using a 1/4 model due to two planes of symmetry $(X-Z, Y-Z)$. FE mesh size convergence study of each model showed that an optimum mesh size is achieved around a pore when the ratio of pore (major) diameter to the finite element size is 25. Ten noded quadratic tetrahedron elements (C3D10) were used for meshing the geometry as shown in Fig. 6.2.

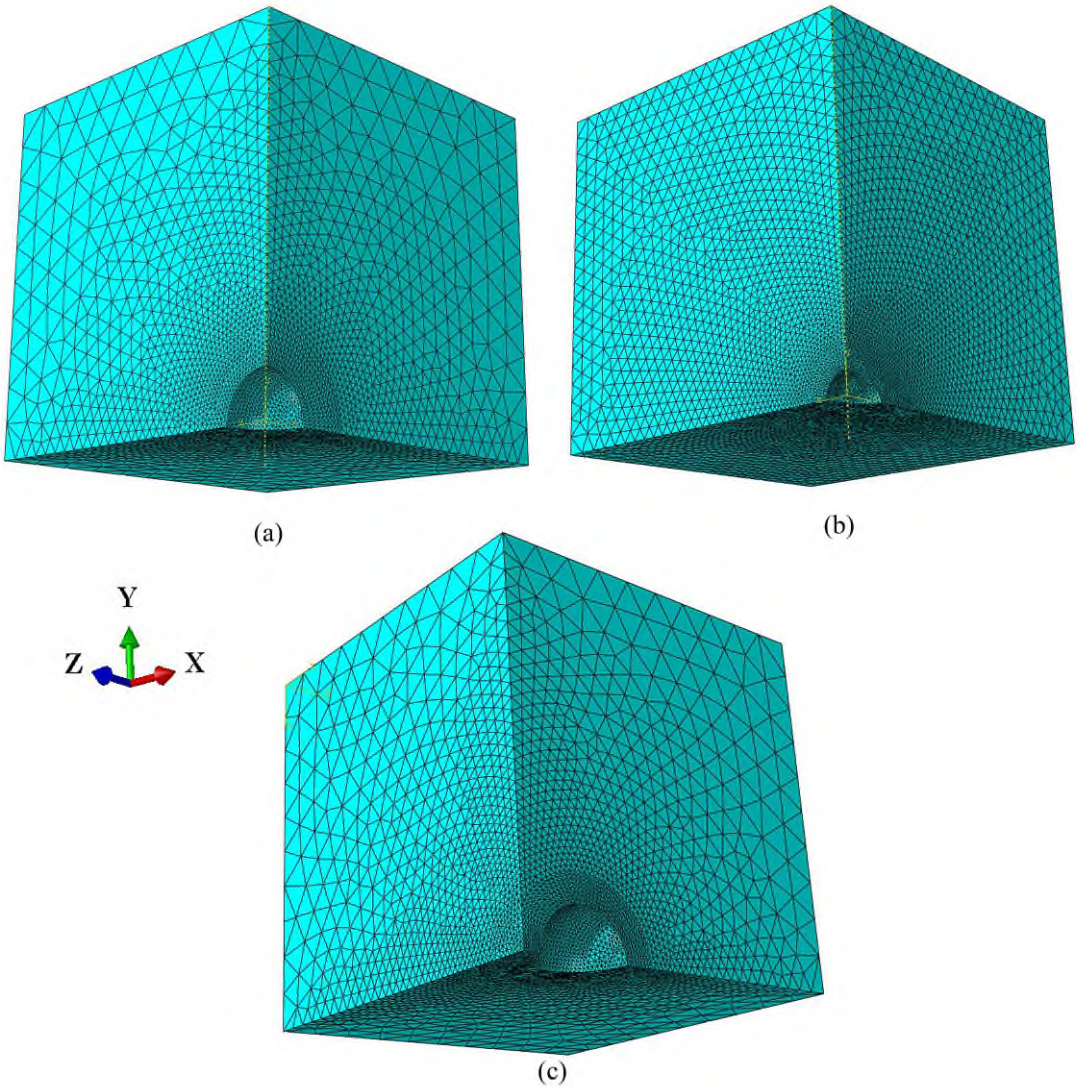

Fig. 6.2 FE mesh used for the various pore geometries shown in Fig. 6.1: (a) spherical pore, (b) oval pore and (c) sub-surface spherical pore. For internal spherical and internal oval pore model, symmetry boundary condition was applied on *X-Z*, *X-Y* and *Y-Z* planes. For surface and sub-surface pore models, symmetry boundary condition was applied on *X-Z* and *Y-Z*. Load was applied in the *Z-X* plane.

Stress concentration factor, K_t, is defined as the ratio of the maximum elastic stress at the pore root to the applied stress. Since it is a geometric parameter, it depends on dimensionless parameters such as the ratio of the model dimension to the pore size and Poisson's ratio.

Therefore to understand the variation in K_t with increase in the model dimension, FE analysis has been conducted where the porosity size was kept constant while increasing the model size. It was found that as the ratio of model size pore size increases, i.e the pore size becomes negligible in comparison with the model size, the value of K_t at the pore root reaches a constant value. The reason for this is that when the model size is much larger than the pore, any further increase in the model dimension has a negligible influence on the local stress distribution at the pore. Accordingly, the minimum model size to pore size ratio required to reach this condition was found to be eight. This implies that beyond this ratio the size of pore does not influence any computed results at the pore root. Since in case of industrial applications the dimension of the components can be much greater than the porosity size, it can be inferred that the value of K_t for porosity defects can be assumed to be dependent only on the shape and location parameters.

6.3.2 X-ray CT pore geometry

Fig. 6.3(a) shows the X-ray computed tomography (X-ray CT) image which includes the spatial distribution of the pores in the specimen gauge section. X-ray CT scan is particularly useful for modelling the actual pore morphology and distribution of pores using image-based FE analysis. The X-ray CT data was processed i.e sectioned and meshed, as shown in Fig. 6.3(b) using the Simpleware® software and imported to FE analysis software (ABAQUS® 6.14). The number of finite elements in the entire gauge section was 8×10^5. However, due to computational limitations, instead of modelling the entire gauge volume, a sub-volume model of the specimen gauge section was selected.

Quadratic tetrahedron element of 10 nodes was used, with element sizes varying between 3 μm (at regions near the pore) and 150 μm (at regions away from the pores) which resulted in approximately 2×10^5 finite elements in the reduced model. Considering the time and expenses involved with X-ray CT scanning, a comparative study was performed using selected pores from the X-ray CT scanned section such that, the location (internal, subsurface or surface) and shape (spherical, oval) was similar to the assumed ideal pore geometry conditions as presented in Section 6.3.1. The stress concentration factor value obtained from the two models, i.e, (i) FE model with pore geometry from X-ray CT and (ii) FE model with idealised pore geometry, were compared to determine the difference between the two models.

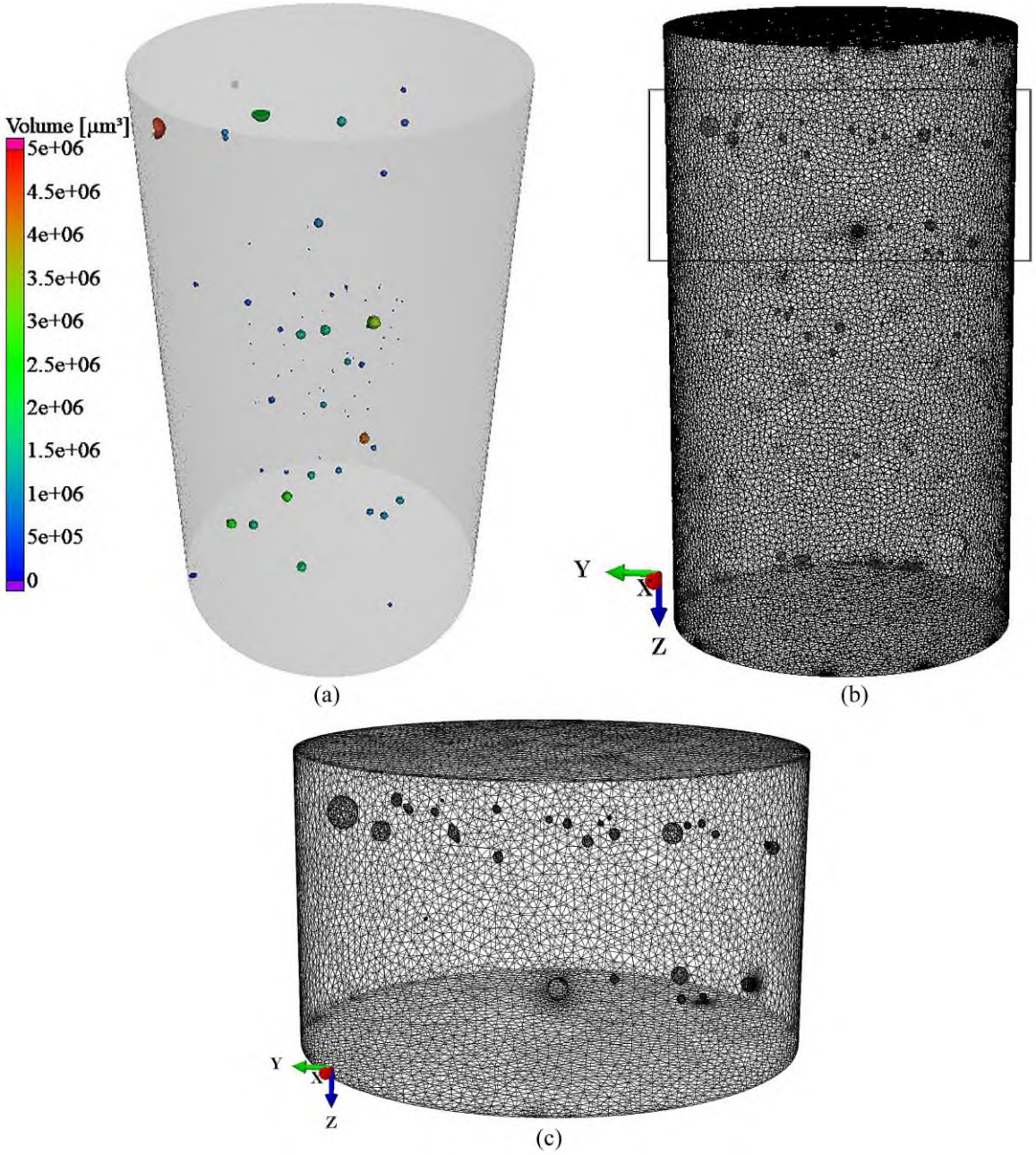

Fig. 6.3 (a) X-ray CT image of the specimen gauge section, (b) finite element (FE) mesh on the X-ray CT scan, (c) FE mesh on a reduced region that is highlighted in (b).

6.3.3 Stress concentration factor due to gas pores

Values of K_t for the various pore geometries were calculated using a linear elastic FE model with uniaxial loading condition and a Poisson's ratio of 0.324 [5]. In 3D geometry, the value of Poisson's ratio, ν, affects the magnitude of load direction stress and is therefore an important parameter in the FE model. In other words, it can be interpreted that the value of K_t is directly proportional to the Poisson's ratio as it increases the Poisson's contraction in the lateral direction exhibited by the material. Elastic FE model results were validated by analytical solutions [31, 33, 32]. The results are presented in Table 6.1. It can be seen that K_t values are virtually the same for the internal spherical pore and the surface hemispherical pore. This is because the "hot spot" at the surface pore root is subjected to a similar boundary condition as that of the internal pore. Fig. 6.4(a) shows that the results of the FE model built from the X-ray CT input (i.e image-based FE model) and Fig. 6.4(b) and 6.4(c) show the FE model built from the ideal spherical subsurface pore geometry assumptions. One of the limitations of image-based meshed FE models is the erroneous indications of high stress regions at the edges of the model, as can be noticed in Fig. 6.4(a). Therefore, the true value of K_t was obtained using the probe tool at the local nodes at the root of various selected pores from Fig. 6.4(a) and compared with the nearest ideal pore geometry as shown in Fig. 6.5. It was observed that the location parameter dominates the K_t for pores located within unit normalised distance of the pore from the free centre (ratio of the true distance of the pore from the free surface to the pore diameter). Influence of location on the pores located further away from free surface was negligible and the value of K_t was found to be close to 2 for all such pores. Further, Fig. 6.4(a) also shows that multiple pore of varying diameter exhibit similar values of K_t, which can be because the load carrying cross-section area is not affected significantly with changes in porosity diameter (which usually varies between 50 μm and 300 μm).

Shape (or aspect ratio) of the pore was also found to be an important parameter. The K_t for an internal oval pore (major diameter twice of minor diameter) was 21% higher than an internal spherical pore thereby indicating that a reduction in the root radius of curvature leads to rapid rise in the local stress value.

Table 6.1 Stress concentration factor values for the pore geometries modelled using elastic FE analysis and comparison with analytical solutions [31–33].

Shape	Aspect ratio	Distance to surface	K_t	% error (FE vs. analytical)
	1	$4d$	2.08	0.9
	1	Surface	2.1	0.6
	2	$4d$	2.50	1.2
	2	Surface	2.53	1.2
	1	$0.02d$ - $0.5d$	4.36 - 2.18	N/A

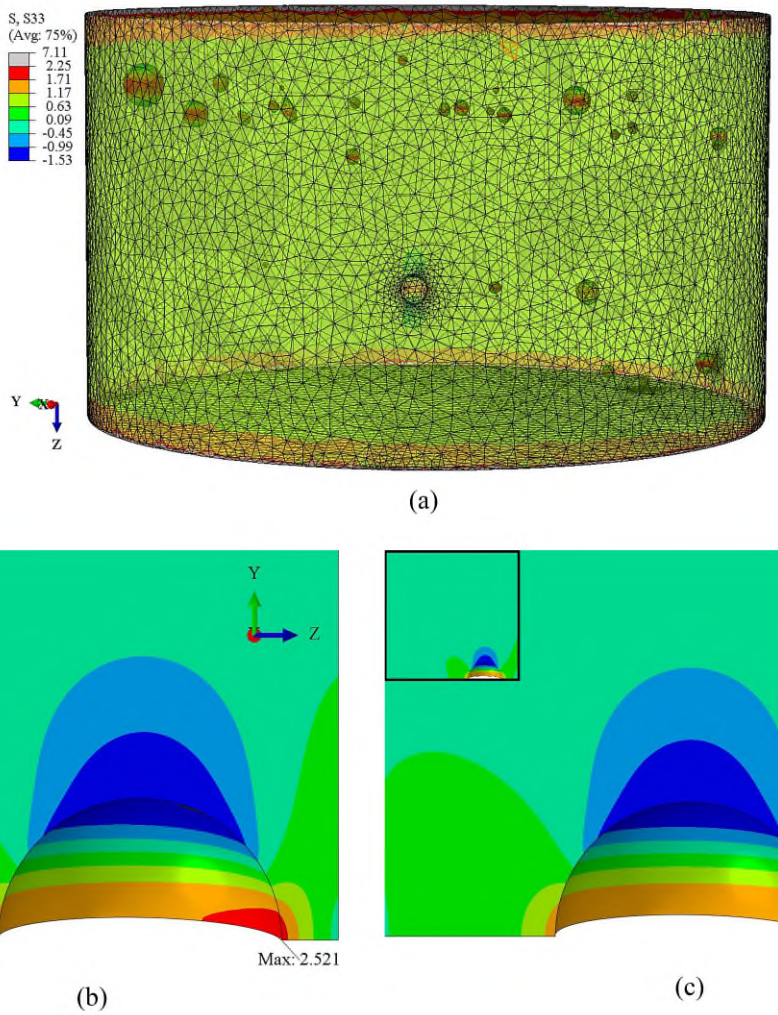

Fig. 6.4 Stress concentration factor at gas pores calculated using: (a) FE model with X-ray CT scanned geometry under unit stress in the *Y*-*X* plane, (b) and (c) overall FE model with assumed pore geometry (top left corner) and enlarged view of local stress distribution under applied unit stress in the *Z*-*X* plane; $x = 0.3d, K_t = 2.52$ in (b), $x = 0.5d, K_t = 2.18$ in (c).

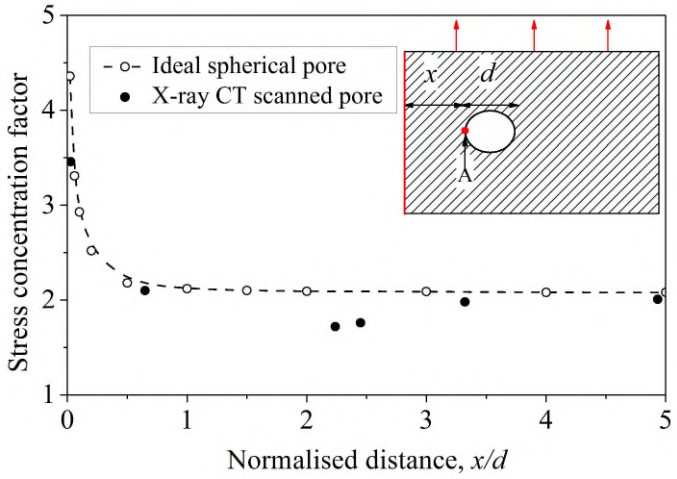

Fig. 6.5 Stress concentration factor, K_t vs. distance, x to free surface (point A, marked in red).

6.4 Elastic-plastic stress-strain analysis

6.4.1 Finite element modelling

(a) Constitutive model

Presence of a stress raiser in the material can lead to the stresses at the pore root to go beyond the yield strength. Therefore, cyclic plasticity analysis was performed with the material models available in the ABAQUS library to model the isotropic and kinematic softening response of Ti-6Al-4V. The von Mises yield criterion was used where the yield surface F was defined by Eq. 6.1.

$$F = f(\sigma - \alpha) - \sigma^0 \tag{6.1}$$

where f represents the von Mises stress function that is also referred to as the J_2 stress function, σ^0 is the yield strength and α the back-stress. Five back-stress components were used to improve the fitting of stress-strain response of the model to the experimentally observed non-linear material response. The back-stress for each strain range was determined by integrating the back-stress evolution over the monotonically rising section of the stabilised hysteresis loop, as shown in Eq. 6.2. The overall back-stress α, was given by the summation of these individual back-stresses, as shown in Eq. 6.3.

$$\alpha_k = \frac{C_k}{\gamma_k}\left(1 - e^{-\gamma_k \varepsilon^{pl}}\right) + \alpha_{k,1} e^{-\gamma_k \varepsilon^{pl}} \tag{6.2}$$

$$\alpha = \sum_{k=1}^{N} \alpha_k \tag{6.3}$$

where $\alpha_{k,1}$ is the k_{th} back-stress at the first data point $(\sigma_1, 0)$, C_k the modulus of the material in the plastic region, and γ_k the rate of decrease of the material modulus with increasing plastic strain. These parameters were determined from inverse analysis operations to obtain a fit with stabilised hysteresis loop measured from the cyclic stress-strain experiment presented in Section 5.4. Further verification of the calibration process was performed using published cyclic stress-strain data from literature [5, 17].

The isotropic softening behaviour of the model was introduced by Eq. 6.4.

$$\sigma^0 = \sigma_0 + Q_\infty(1 - e^{-b\bar{\varepsilon}^{pl}}) \tag{6.4}$$

where σ^0 is the yield stress for the n^{th} cycle, σ_0 the yield stress at zero plastic strain, Q_∞ the maximum change in the value of yield stress, b the rate of decrease of yield stress with an increase in equivalent plastic strain, $\bar{\varepsilon}^{pl}$.

The FE model was calibrated such that the computed hysteresis loops reach the stabilised state within 20 load cycles. In general, under cyclic loading, the localised plastic zone at a pore root is subjected to displacement controlled loading condition owing to the constraint effect of the surrounding material which is subjected to elastic loading conditions. Therefore, the model was calibrated using the stabilised hysteresis loops for WAAM Ti-6Al-4V obtained from fully reversed displacement controlled cyclic load test as described in Section 5.4. Additionally, the parameters for selective laser melted Ti-6Al-4V were also determined using the stabilised hysteresis loops published in literature [5, 17]. The values of C_k, γ_k, Q_∞ and b for WAAM and SLM Ti-6Al-4V are given in Table 6.2. Fig. 6.6(a) and 6.6(c) compares the hysteresis curves of the first and the stabilised cycle extracted from the experiment (at 2% fully reversed applied strain amplitude) with the corresponding hysteresis loop calculated by the mixed cyclic plasticity model for WAAM and SLM Ti-6Al-4V respectively. Fig. 6.6(b) and 6.6(d) shows the stabilised hysteresis loops for WAAM and SLM Ti-6Al-4V at 1%, 1.5% (only for WAAM) and 2% fully reversed applied strain amplitudes, compared with the respective stabilised hysteresis loops computed by the FE model.

Table 6.2 Cyclic plasticity model parameters fitted to stabilised hysteresis loops of WAAM and SLM Ti-6Al-4V [5]

WAAM				SLM			
C_k(GPa)	γ_k	Q_∞(MPa)	b	C_k(GPa)	γ_k	Q_∞(MPa)	b
95	2000	-100	0.5	100	3000	-206	7
52	1200			70	3000		
35	850			45	3000		
22	100			30	850		
6.8	50			29.7	12		

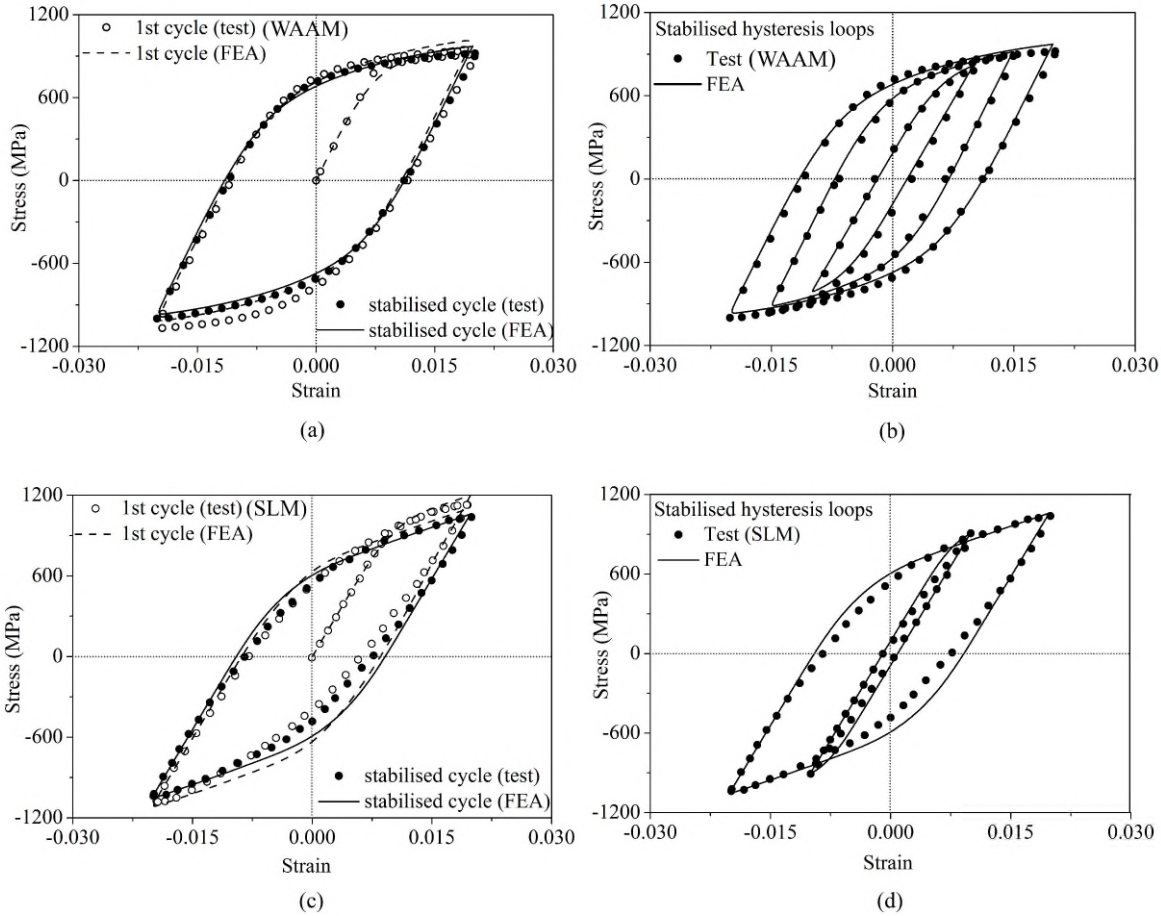

Fig. 6.6 Comparison of the cyclic plasticity model results with experimental hysteresis loop obtained at fully reversed applied strain amplitude, (a) WAAM Ti-6Al-4V (first cycle and stabilised cycle at 2%), (b) WAAM Ti-6Al-4V (stabilised cycles at 1%, 1.5% and 2%), (c) SLM Ti-6Al-4V (first cycle and stabilised cycle at 2%), (d) SLM Ti-6Al-4V (stabilised cycles at 1% and 2%).

(b) Application of cyclic plasticity model to gas pores

Elastic-plastic FEA was performed using cyclic loading to investigate the local stress-strain state, plastic deformation and local stress ratio at the root of the various pore geometries. The calibrated parameters (refer Table 6.2) for WAAM and SLM Ti-6Al-4V were applied as the material models that define the transition of the yield stress response surface due to cyclic loading. The pore geometries (shown in Fig. 6.1) were modelled using applied stress amplitudes between 200 MPa and 560 MPa and stress ratios ranging between 0.1 and -0.5. The hysteresis loops obtained at the root of the pores are provided in Fig. 6.7 for an applied stress amplitude and stress ratio of 560 MPa and -0.5 respectively.

Fig. 6.7(a-e) show the cyclic stress-strain response of WAAM Ti-6Al-4V alongside the corresponding results for SLM Ti-6Al-4V presented in Fig. 6.7(f-j) to make a comparative study of the two AM processes. It can be seen in Fig. 6.7(a,b) (for WAAM) and Fig. 6.7(f,g) (for SLM) that the hysteresis loops obtained at the root of an internal spherical pore was comparable to the hysteresis loops obtained at the root of a hemispherical pore. This can be explained by the similar boundary condition acting at the pore root for both the sites which was also discussed earlier in the elastic stress analysis. A similar behaviour was observed for an internal oval pore and a surface oval pore as shown in Fig. 6.7(c-d, h-i), thereby confirming the effect of surrounding constraint on the local stress and strain profile.

The higher K_t for the internal (K_t = 2.5) and surface oval (K_t = 2.52) pore leads to higher cyclic plastic strain accumulation as shown in (Fig. 6.7(c,d) and 6.7(h,i) for WAAM and SLM respectively. Same statement can be made for the subsurface pore in Fig. 6.7(e) and 6.7(j). The higher stress concentration at the root of the pore will cause the material within the plastic zone of the pore to undergo yielding while the surrounding material remains below the elastic threshold. Consequently, the stress drops in the plastic zone at the expense of higher plastic strain and the maximum stress shifts to the surrounding elastic region in the plane perpendicular to the loading axis. This shows that once the crack initiates, it will propagate in the plane perpendicular to the loading axis. It was observed that WAAM Ti-6Al-4V undergoes higher cyclic plastic deformation as compared to SLM Ti-6Al-4V. This behaviour can be explained by the relatively lower value of initial yield strength (800 MPa) of WAAM as opposed to a higher yield strength of SLM (1000 MPa [5]).

The distribution of stress and strain at a surface hemispherical pore modelled using SLM Ti-6Al-4V material property is shown in Fig. 6.8. The stress value was found to vary along the circumference of the pore, with the stress concentration being highest at the bottom of the

pore. This difference is caused due to the difference in applied boundary conditions on the two faces adjacent to the pore. One face is free while the other is constrained due to the symmetry boundary condition.

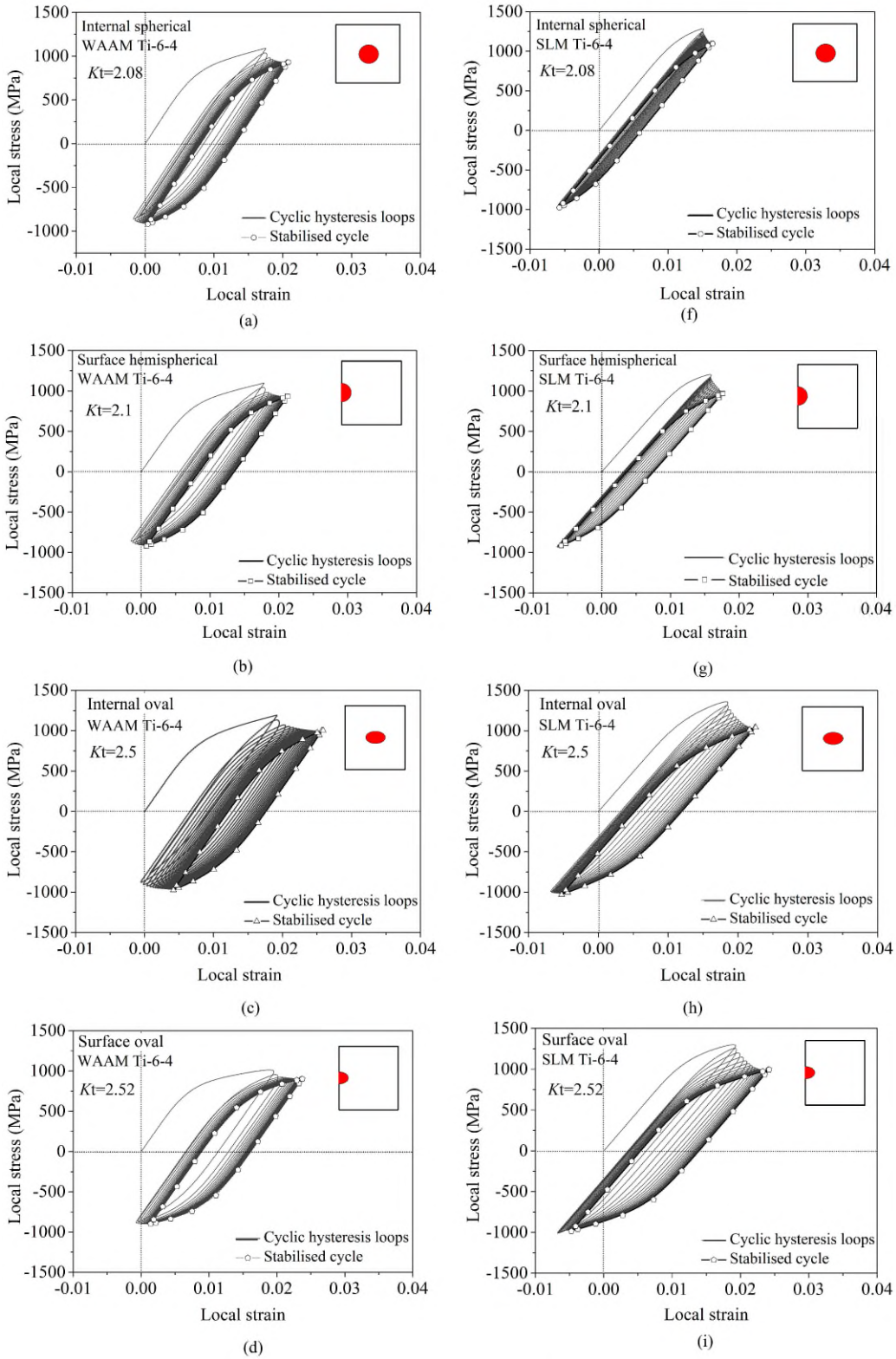

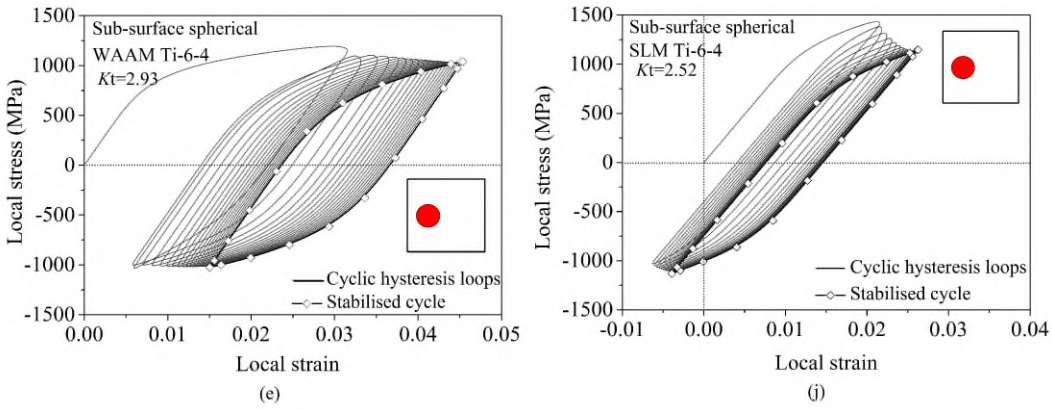

Fig. 6.7 FEA results of stable hysteresis loops at the root of various pore geometries: (a-e) WAAM Ti-6Al-4V and (f-j) SLM Ti-6Al-4V. Sub-surface pore in (e) is 0.2*d* from free surface, and (j) is 0.3*d* from free surface, *d* is pore diameter; applied stress amplitude 560 MPa, applied stress ratio -0.5. Note the reduction in local stress ratio to -1 due to the stress concentration and cyclic plastic deformation.

Therefore the edge of the pore adjacent to the free surface (mouth) shows higher local strain (refer Fig. 6.8a) while the bottom (refer Fig. 6.8b). The higher stress concentration at the root of the surface hemispherical pore will therefore lead to crack initiation at the pore root.

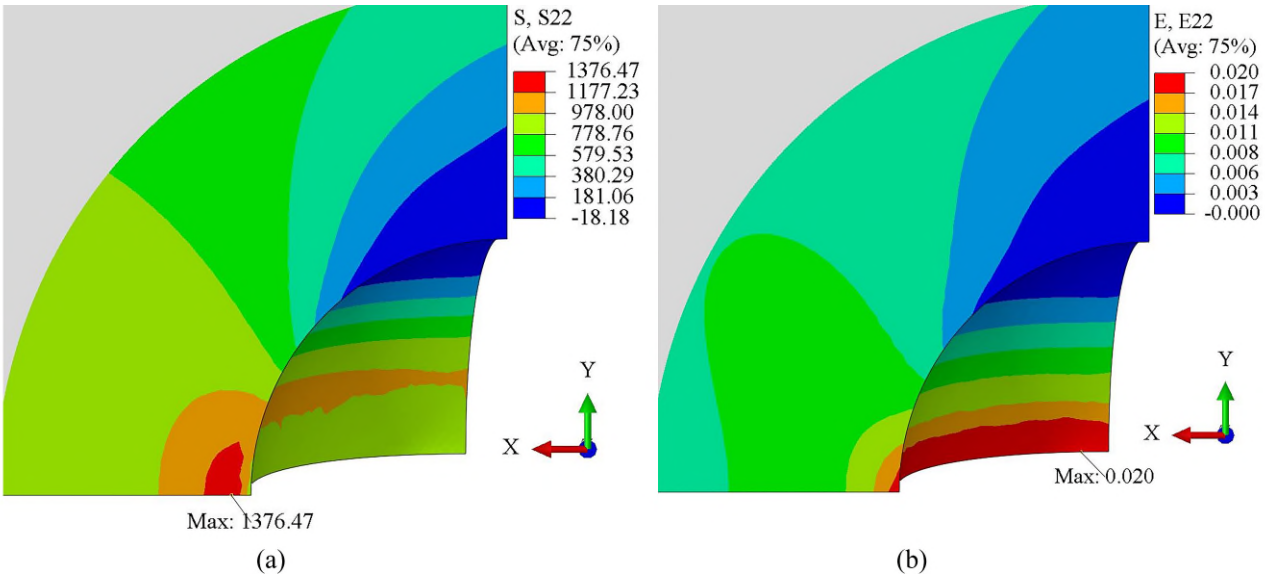

Fig. 6.8 Surface hemispherical pore (symmetry boundary in *X-Z, Y-X*; free boundary in *Z-Y*), (a) local stress greatest at the pore root indicated as "Max 1376.47" (symmetric boundary condition on the adjacent faces), (b) local strain is greatest at pore mouth indicated as "Max 0.02" (free boundary on one face); at applied maximum stress 750 MPa, applied stress ratio -0.5, SLM Ti-6Al-4V material model.

Fig. 6.9(a) and 6.9(b) respectively show the local stress and strain distribution in the loading direction for a surface pore calculated using WAAM Ti-6Al-4V material model; applied stress amplitude of 315 MPa and applied stress ratio of 0.1 and the schematic of the front view of the pore geometry is given in Fig. 6.9. Note that the pore geometry is not hemi-spherical as the depth of the point of stress concentration from the free surface is 0.8*d*. The location of maximum

stress was at the root of the pore while that of the maximum strain was at the free surface or the mouth of the pore. Fig. 6.9(c) shows the stress vs. strain calculated at the pore root. It can be seen that after a few initial ratcheting cycles, the stress vs. strain response stabilises. Further, it was observed that the mean stress at the root of the pore was always lower than the applied stress and the percentage reduction was directly proportional to the applied maximum stress, applied stress ratio, and the K_t.

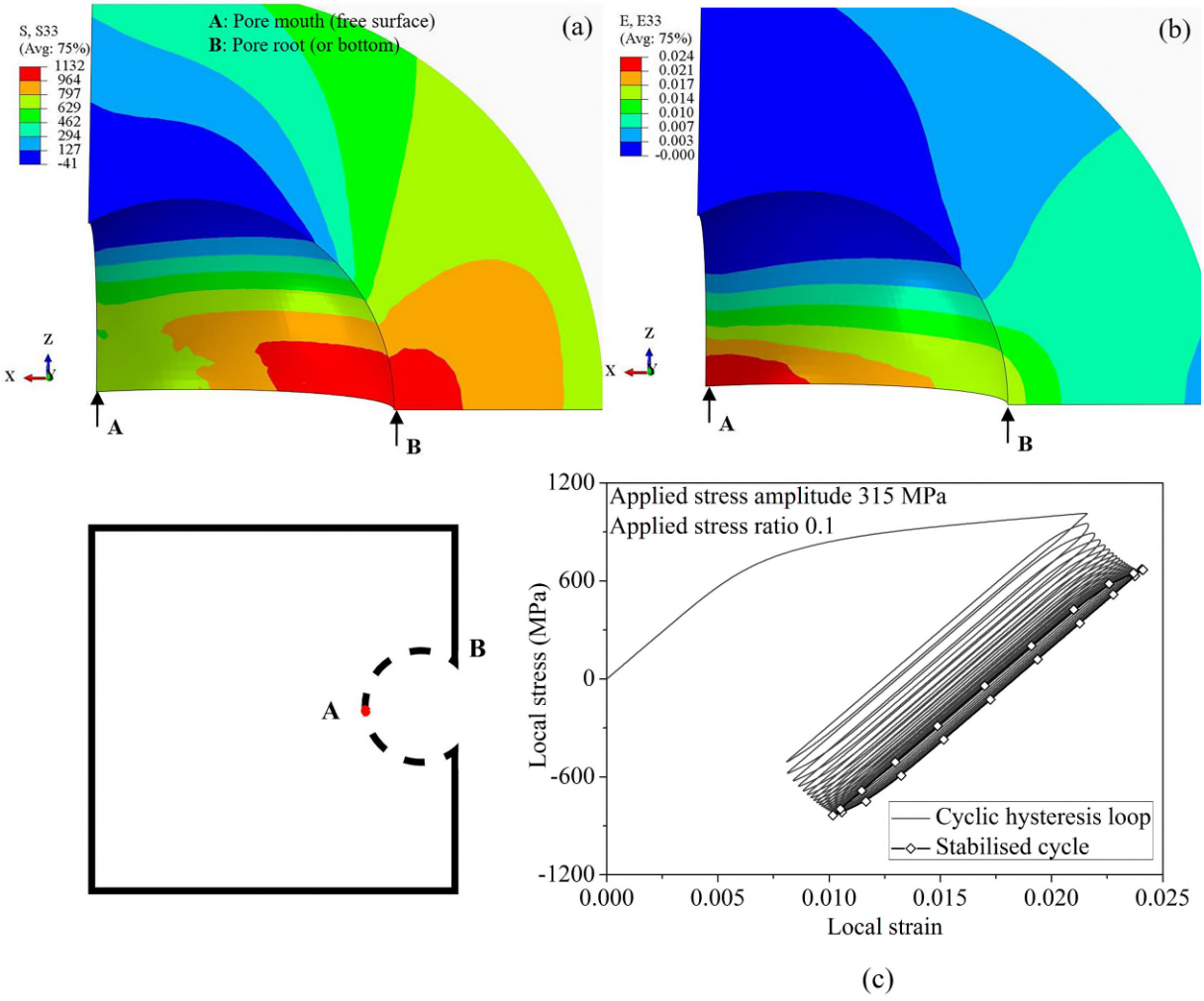

Fig. 6.9 Stress and strain distribution at pore root (applied maximum stress 700 MPa, stress ratio 0.1, WAAM Ti-6Al-4V material model): (a) maximum local stress at pore root, (b) maximum local strain at pore mouth, (c) mean stress relaxation at the pore mouth.

6.4.2 Neuber's method as an alternative to FEA

If porosity is treated as a notch, then the Neuber's method can be applied to calculate the local stress and strain. Eq. 6.5 shows the relation between the local stress and strain amplitude (σ_a and ε_a) and the applied stress amplitude (S_a) and stress concentration factor (K_t). Since this approach is limited to applications with known analytical values of K_t, subsurface pores were not included

in this analysis. For life prediction, use of the fatigue notch strength reduction factor (K_f) is preferred over K_t to avoid highly conservative estimation (Eq. 6.6). K_f is the ratio of the fatigue strength of smooth specimens to that of notched specimens.

$$\sigma_a \varepsilon_a = \frac{(K_t S_a)^2}{E} \tag{6.5}$$

$$\sigma_a \varepsilon_a = \frac{(K_f S_a)^2}{E} \tag{6.6}$$

K_f and K_t are related by the notch sensitivity factor q, as shown in Eq. 6.7. From [20], the value of q for Ti-6Al-4V ELI can be deduced as 0.6. Therefore, K_f is lower than K_t to account for the plasticity and notch sensitivity effects. Eq. 6.8 and Eq. 6.6 were solved simultaneously to obtain the local stress and total strain at the root of the pore.

$$K_f = q(K_t - 1) + 1 \tag{6.7}$$

$$\Delta \varepsilon_a = \frac{\Delta \sigma_a}{E} + \left(\frac{\Delta \sigma_a}{K'}\right)^{1/n'} \tag{6.8}$$

where σ_a and ε_a are the local stress amplitude and local strain amplitude respectively, K_f and K_t are the fatigue notch sensitivity factor and elastic stress concentration factor respectively and E, K' and n' are the material constants i.e Young's modulus, cyclic strength coefficient and cyclic strain hardening exponent respectively.

6.4.3 FE vs. Neuber's method

Neuber's approach was also used to calculate the local stress and strain at the root of the three pore geometries. The FE model results were plotted against Neuber's results in Fig. 6.10 in terms of calculated local strain amplitude, under applied stress amplitudes between 200 MPa and 560 MPa with applied stress ratios of 0.1, -0.2 and -0.5. It was found that local strain obtained from FE model was in good agreement with Neuber's method for lower plastic strains. For higher plastic strains, Neuber's method was relatively conservative as compared to FE method. This is because Neuber's method is better suited for low plastic strains [107], whereas the advanced computation techniques in FE method have enabled us to implement complex algorithms to model the non-linear material response with a better approximation.

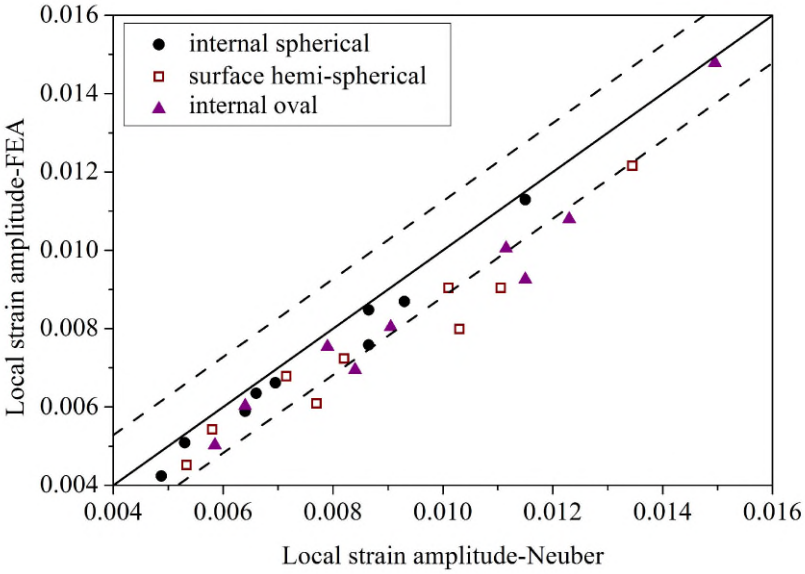

Fig. 6.10 Calculated local strain amplitudes: FEA vs. Neuber's method. Dotted lines indicate ±10% error.

6.5 Fatigue life prediction method

Fatigue life of WAAM Ti-6Al-4V containing a gas pore was predicted with the following assumptions:

(a) Pores can be considered as notches as they both are stress raisers, and fatigue life is controlled by the local stress and strains at the root of the critical pore (pore root location is indicated in Fig. 6.1).

(b) Predicted fatigue life at pore root using the local stress and strain values from elastic-plastic FE model and material's S-N data represents the crack initiation life at pore root. (Note: subsequent crack propagation life is relatively short for a small specimen, whereas for a service part with a similar pore and subjected to similar local cyclic stress-strain histories, crack propagation life is much longer and cannot be neglected).

The stabilised local stress-strain response under fatigue loading was obtained using the cyclic plasticity model discussed in Section 6.4.1. When the area enclosed by the hysteresis loop is negligible, i.e local stress-strain response is elastic, the local stress amplitude can be used to predict the fatigue life by using the S-N data of defect-free WAAM Ti-6Al-4V as shown in Fig. 5.8. It should be noted that the local mean stress (if present) should be accounted by using Walker's equation [39] as shown in Eq. 6.9.

$$\sigma_e = \sigma_{max}\left(\frac{1-R}{2}\right)^{0.28} \tag{6.9}$$

where σ_e is the equivalent stress amplitude for fully reversed loading, σ_{max} the maximum stress amplitude and R the stress ratio at the notch root.

In case of WAAM Ti-6Al-4V, the local stress and strain amplitude was calculated from the cyclic plasticity model and used in the Basquin's relationship (WAAM Ti-6Al-4V material property provided in Chapter 5 Table 5.2) for fatigue life prediction. Owing to mean stress relaxation, the local stress ratio at the pore was reduced to nearly -1 for the various applied stress ratios. In case of SLM Ti-6Al-4V, the local strain amplitude and the local maximum stress obtained from the cyclic plasticity model were used in the SWT model (Eq. 6.10) [99], where the local maximum stress term is used to account for the effect of the local mean stress. The material property data for SLM Ti-6Al-4V was taken from [85].

$$\varepsilon_a \sigma_{max} = \frac{(\sigma_f')^2}{E}(2N_f)^{2b} + \sigma_f'\varepsilon_f'(2N_f)^{b+c} \tag{6.10}$$

where the material constants (σ_f' the fatigue strength co-efficient, b the fatigue strength exponent, ε_f' the fatigue ductility co-efficient and c the fatigue ductility exponent) were presented in Table 5.2.

6.6 Validation of life prediction method

6.6.1 Using WAAM Ti-6Al-4V test data from this study

Two batches of test specimens were used for validating the life prediction method. The first batch included the specimens where the FE model was conducted on assumed pore geometry concept with the crack initiating defect characteristics determined solely from the SEM fractographs. The second batch included the samples where the critical defect was identified using interrupted fatigue-tomography testing. The characteristics of the crack initiating pore (shape, location and proximity to other pores) were determined from image-based meshed geometry subjected to linear elastic stress analysis. Later, an assumed pore geometry model was used (to enhance computational efficiency) for running the cyclic model and obtain the local stress and strain values. As a result of mean stress relaxation, the local stress ratio at the pore was reduced to -1 while the applied stress ratio was 0.1. Therefore, the local stress and strain amplitude was used in the Basquin's equation for fatigue life prediction.

Fatigue life predicted by the model corresponded well with the test fatigue life as shown in Table 6.3. Fig. 6.11(a) shows that the error in the fatigue life prediction was significantly higher

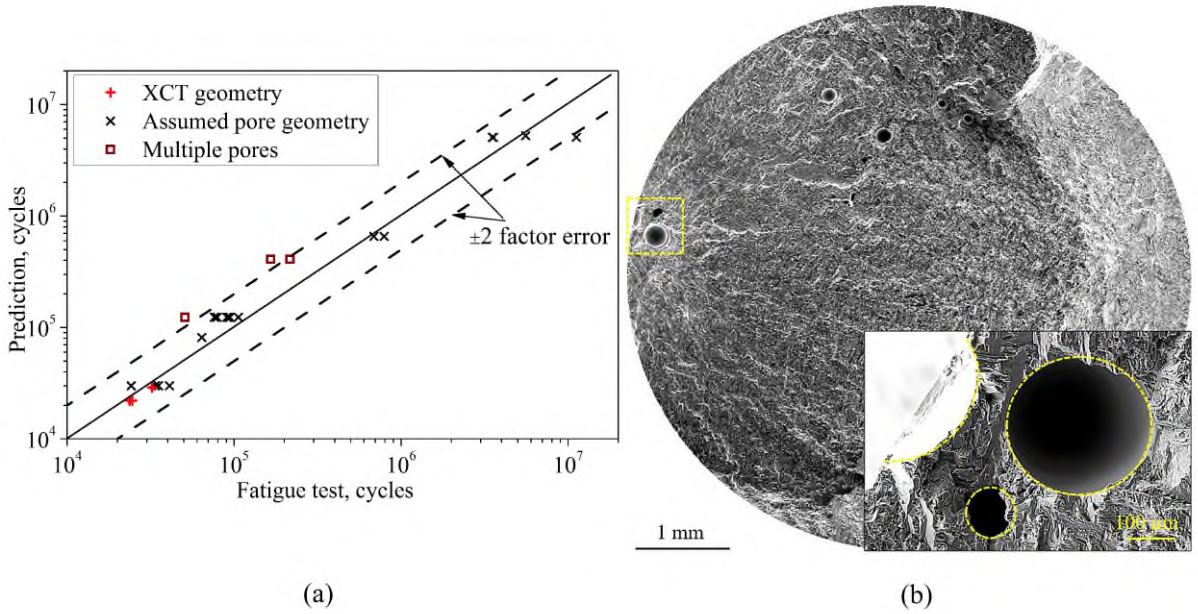

Fig. 6.11 Validation of fatigue life prediction method with WAAM Ti-6Al-4V test data, (b) specimen with multiple pores leading to over-prediction by FE model which is based on isolated critical pore geometry.

when the prediction is based solely on information from fracture surface as opposed to when X-ray CT information is used in addition to fracture surface analysis (results in Table 6.3). In some cases, the over-prediction of the model was justified by the presence of multiple pores in close proximity to each other as shown in Fig. 6.11(b).

Table 6.3 Validation of FE model predictions with WAAM Ti-6Al-4V test data.

Pore diameter (μm)		Pore root depth from surface (μm)	Normalised distance (x/d)	Fatigue life (test) (cycles)	Fatigue life (prediction) (cycles)	Error %
XCT*	SEM**					
162	288	144	0.5	3.23×10^4	2.9×10^4	10.2
229	328	240	0.7	2.37×10^4	2.2×10^4	7.17
241	534	430	0.8	2.46×10^4	2.2×10^4	10.5

Note: Pore diameter measured on the fracture surface was used in the (cyclic plastic) FE model.
*pore dia. before fatigue test measured using X-ray CT (XCT) technique
**pore dia. on fracture surface measured using SEM imaging technique

6.6.2 Using AM Ti-6Al-4V test data from literature

Fatigue data reported in the literature with respective fracture surface images showing crack initiation at individual gas pores were used to validate the prediction model. From the fracture surface images, the pore geometry, distance from free surface and the nearest idealised defect shape were determined for modelling.

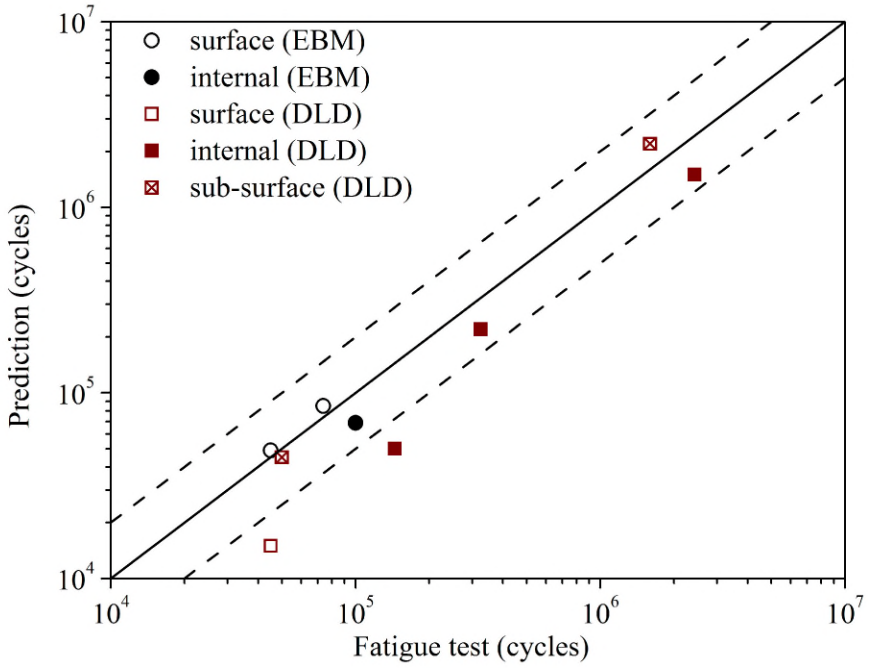

Fig. 6.12 Validation of the fatigue life prediction with the fatigue test data taken from literature as shown in Table 6.4.

Table 6.4 Fatigue test data of AM Ti-6Al-4V specimens taken from literature with crack initiation at gas pores of known size, location and shape.

Crack initiating defect			AM process [ref.]	Maximum applied stress (MPa)	Applied stress ratio	Fatigue life (prediction) (cycles)	Fatigue life (test) (cycles)
Location	Aspect ratio	Dia. μm					
Surface	1	72	EBM[66]	575	0	8.5×10^4	7.3×10^4
Surface	1	70	EBM[66]	600	0	4.9×10^4	4.5×10^4
Internal	1	170	EBM[66]	600	0	6.9×10^4	1×10^4
Subsurface	1	45	DLD[18]	356	-1	2.2×10^6	1.6×10^6
Subsurface	1	58	DLD[18]	470	-1	1.5×10^4	4.5×10^4
Surface	1	100	DLD[18]	415	-1	4.5×10^4	5×10^4
Internal	1		DLD[52]	680	0.1	5×10^4	1.4×10^4
Internal	1	160-240	DLD[52]	570	0.1	2.2×10^5	3.2×10^5
Internal	1		DLD[52]	550	0.1	1.5×10^6	2.4×10^6

Note: Porosity-fatigue life data of reference [18] was provided by the authors via. email communications.

The present FE model does not account for the interaction between adjacent pores, therefore the test cases were selected with no other visible pores in the vicinity of the crack initiating pore. All the studies [18, 66, 52] reported the use of optimized processing parameters, which makes it highly likely that the distance between the pores is more than four times the pore diameter, which was determined by the FE model in this study to be the minimum distance for neglecting any interaction. Summary of the porosity characteristics and experimental fatigue life [18, 66, 52] are presented in Table 6.4 along with the fatigue life prediction conducted in this study. The local strain obtained from FE analysis was used in the SWT relationship, Eq. 6.10, to predict the fatigue life. Fig. 6.12 shows that the fatigue life prediction was in good agreement with the test data.

6.7 Summary

The effect of isolated porosity defects on the fatigue strength of wire + arc additive manufactured Ti-6Al-4V material is evaluated based on the gas pore morphologies found in experiments. Elastic-plastic finite element analysis was performed first to calculate the cyclic plastic deformation, local stress and strains, and local mean stress change at the vicinity of the pores. The strain-life approach is used for the life prediction. S-N data of defect-free WAAM Ti-6Al-4V are used as the benchmark for the material performance. Key findings can be summarised as:

(1) Stress concentration factor (K_t) mainly depends on the location and shape of isolated gas pores. When the location of a spherical gas pore is more than four times of its diameter from the free surface, it is regarded as an internal defect and K_t is 2.08. For a subsurface spherical pore, K_t increases to the value range of 2.2 to 4.3 depending on the proximity to free surface. When the shape of internal pore change from spherical to oval with an aspect ratio of 2, K_t increases from 2.08 to 2.5.

(2) The size of internal gas pore has little effect on the stress concentration factor, although larger pore contributes towards reduction in the load carrying cross-section area.

(3) Plastic deformation at the pore root causes local mean stress relaxation. Using the local stress and strains from finite element analysis in the Smith-Watson-Topper strain-life equation can account for the effects of higher local strains and mean stress relaxation in the fatigue life prediction for wire + arc additive manufactured (WAAM) Ti-6Al-4V specimens with gas pores.

(4) The life prediction method was validated with fatigue tests performed on WAAM Ti-6Al-4V and published test results on powder based AM Ti-6Al-4V alloys.

Chapter 7

Fracture Mechanics Modelling and Fatigue Strength Prediction

7.1 Introduction

The effect of the shape and location of gas pores on the fatigue life was presented in the previous chapter using the classic notch-fatigue approach. One of the limitations of using notch-fatigue analysis is the model being independent of the porosity size. Prior works of Murakami [74] and El-Haddad [89] have applied fracture mechanics to small irregular defects by assuming the defect as a crack. Murakami coined the square root area term as the equivalent crack size for a small embedded defect while El-Haddad introduced an additional crack length parameter to maintain the concept of similitude in the short crack regime by increasing the stress intensity factor value. The present chapter is based on the aforementioned models, following which, the stress intensity factor range was used as a fatigue design parameter. Further, the reduction in the fatigue strength due to the presence of gas pores was presented in the form of the Kitagawa-Takahashi diagram as it is essential for the quality control of materials, especially when the part consists of defects, as in case of AM materials.

7.2 Fatigue design using stress intensity factor range

The fatigue test results presented in Section 5.5 showed that when considered separately, neither the applied stress amplitude (Fig. 5.8) nor the size of the crack initiating pore (Fig. 5.11) correlated with the fatigue life. In order to jointly consider the two parameters, i.e applied stress range and the porosity size, fracture mechanics concept was applied. According to Murakami's

approach [74], the square root of the projected area of an embedded gas pore can be assumed as the equivalent planar crack length. Eq. 7.1 shows the Murakami's approach to calculate the stress intensity factor range for a small defect [74]. The stress intensity factor range for gas pores was calculated using this approach and was re-plotted as the relation of ΔK vs. N in Fig. 7.1 to obtain a substantially better correlation between the two parameters.

$$\Delta K = C \times \Delta\sigma \sqrt{\pi \sqrt{area}} \tag{7.1}$$

where ΔK is the stress intensity factor range, $\Delta\sigma$ the applied stress range, $\sqrt{area}$ the square root of the projected area of the pore perpendicular to the loading direction and parameter C is 0.5 for internal defects and 0.65 for surface defects [74].

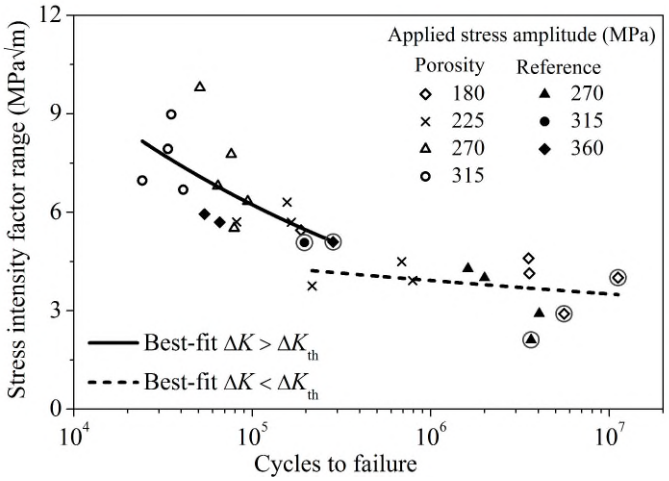

Fig. 7.1 Correlation between fatigue life and normalised stress intensity factor range (ΔK) for porosity defects tested in this study (ΔK was calculated using the Murakami's equation, Eq. 7.1.

It was also observed that the best fit curve for the experimental data points presented in Fig. 7.1 had a sudden change in the slope, i.e was discontinuous at the value of threshold stress intensity factor range of the material (ΔK_{th}). The explanation for this behaviour can be the exponential drop in the crack growth rate when the crack growth driving force, ΔK, is below its threshold value ΔK_{th}, leading to a considerable increase in the fatigue life, hence the change in the slope of the best fit curves [91]. From Fig. 7.1, the threshold stress intensity factor range of the material can be estimated as $4.5\sqrt{\text{m}}$ at the point of discontinuity, which agrees with the reported values of ΔK in literature for AM Ti-6Al-4V [87, 10, 34, 116].

7.3 Modified Kitagawa-Takahashi diagram

The original Kitagawa-Takahashi (K-T) diagram combines the intrinsic fatigue limit of the material to the LEFM non-propagating crack condition and sets the fatigue limits for the given life [105]. It was developed based on the LEFM material properties for long cracks. For small irregular defects, Beretta and Romano adapted and modified the K-T diagram [87]. However, the experimental tests performed in this study have shown that in case of spherical gas pores, a lower bound should be set for the K-T diagram by the notch fatigue limit for porosity defects. Therefore, in it is proposed that the K-T diagram for porosity defects should have three regions as shown in Fig. 7.2 and elaborated as follows.

(a) Region I is set by the material's intrinsic fatigue limit and forms the upper bound of the fatigue limit vs. porosity size curve. This condition is applicable when the porosity size reduces to near zero, thereby resulting in negligible effect on the fatigue limit of the material.

(b) Region II sets the criterion for non-propagating defects based on the LEFM condition of SIF range equal to the threshold SIF range (ΔK=ΔK_{th}).

(c) Region III is set by the notch fatigue limit due to the porosity defect and forms the lower bound of the fatigue limit vs. porosity size curve. A similar approach was also applied in a previous study to modify the K-T diagram for notched specimens [117].

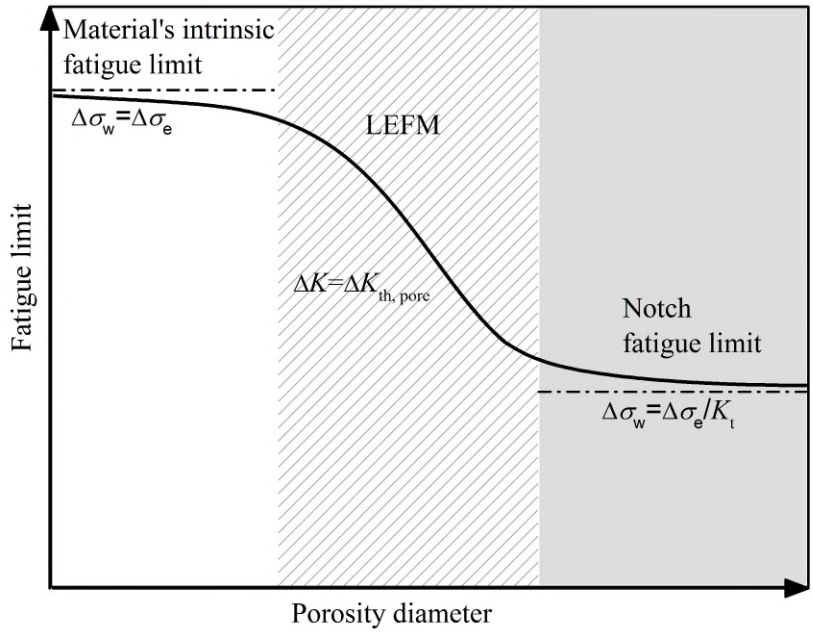

Fig. 7.2 Schematic of the proposed effect of porosity size (diameter) on the fatigue limit.

However, the size of porosity ranges only within a few hundred microns and thereby lies in the short crack regime. The condition of similitude does not apply for defects in this regime, as at similar nominal SIF range, they grow at a faster rate than long cracks [110, 111]. In other words,

applying the LEFM condition would give non-conservative predictions for porosity defects. Therefore, as presented in a previous study on defect tolerances [87], Murakami's square root area argument the was used to represent the porosity size which was then applied in the El Haddad's model [89] to satisfy the condition of similitude for porosity defects. El Haddad et al. [89] introduced an additional crack length, a_0, as shown in Eq. 7.2 to use the LEFM theory for short cracks. It has been referred to as the El Haddad material constant, given in Eq. 7.3. It can be seen that the value of SIF for short crack length is increased by the El Haddad material constant.

$$\Delta K = \Delta\sigma\sqrt{\pi(a+a_0)} \tag{7.2}$$

$$\Delta K_{\text{th}} = \Delta\sigma_{\text{e}}\sqrt{\pi a_0} \tag{7.3}$$

where ΔK is the stress intensity factor range, $\Delta\sigma$ the applied stress range, a the short crack length, a_0 the El Haddad material constant, ΔK_{th} the stress intensity factor range threshold obtained from long crack fatigue test (4.5 MPa$\sqrt{\text{m}}$), $\Delta\sigma_{\text{e}}$ the intrinsic fatigue limit of the material (540 MPa for WAAM Ti-6Al-4V, R=0.1).

Let ΔK=ΔK_{th}, from Eqs. 7.2 and 7.3, the reduced fatigue limit, $\Delta\sigma_{\text{w}}$, is given by Eq. 7.4, which also bridges the fatigue limit to the linear elastic fracture mechanics threshold condition via a smooth transition region.

$$\Delta\sigma_{\text{w}} = \Delta\sigma_{\text{e}}\sqrt{\frac{a_0}{a+a_0}} \tag{7.4}$$

where $\Delta\sigma_{\text{w}}$ is the reduced fatigue limit of the material due to short crack.

Beretta and Romano modified the El Haddad's model for porosity defects by replacing the short crack length in Eq. 7.4 with the Murakami's square root area parameter as shown in Eq. 7.5 [87] for calculating the fatigue limit for specimens with crack initiation at porosity defects. Further, Eq. 7.5 converges to the upper bound set by the material's intrinsic fatigue limit when the defect size reduces to zero ($\sqrt{area} = 0$).

$$\Delta\sigma_{\text{w}} = \Delta\sigma_{\text{e}}\sqrt{\frac{\sqrt{area_0}}{\sqrt{area}+\sqrt{area_0}}} \tag{7.5}$$

where $\sqrt{area}$ is the defect size expressed according to Murakami's square root area argument, and $\sqrt{area_0}$ is the modified El Haddad parameter that was calculated according to Eq. 7.1 by

replacing ΔK with $\Delta K_{\text{th,LC}}$ (4.5 MPa$\sqrt{\text{m}}$) and $\Delta\sigma$ with the material's intrinsic fatigue limit $\Delta\sigma_{\text{e}}$ (540 MPa). Therefore, the El Haddad parameter in Eq. 7.5 for WAAM Ti-6Al-4V was calculated as 52 μm for both surface and sub-surface pores, and 88 μm for internal pores.

The lower bound was determined from Eq. 7.6. However, use of stress concentration factor, K_{t}, can be conservative as the notch sensitivity of Ti-6Al-4V is often reported to be between 0.5 to 0.6 [20, 94]. Therefore, Eq. 7.7 was used to find the notch fatigue factor, K_{f}, which sets the lower bound of the K-T diagram for porosity defects.

$$\Delta\sigma_{\text{w}} = \frac{\Delta\sigma_{\text{e}}}{K_{\text{t}}} \tag{7.6}$$

$$\Delta\sigma_{\text{w}} = \frac{\Delta\sigma_{\text{e}}}{K_{\text{f}}} \tag{7.7}$$

where K_{t} is the stress concentration factor and FE analysis presented in Chapter 6 showed that the value of K_{t} for spherical internal pores is 2.08. K_{f} is the notch fatigue factor determined by the ratio of the fatigue limit of the reference (or smooth) specimens to the fatigue limit of the porosity specimens. The value of K_{f} was 1.5 for the fatigue test results presented in Chapter 5 (Fig. 5.8).

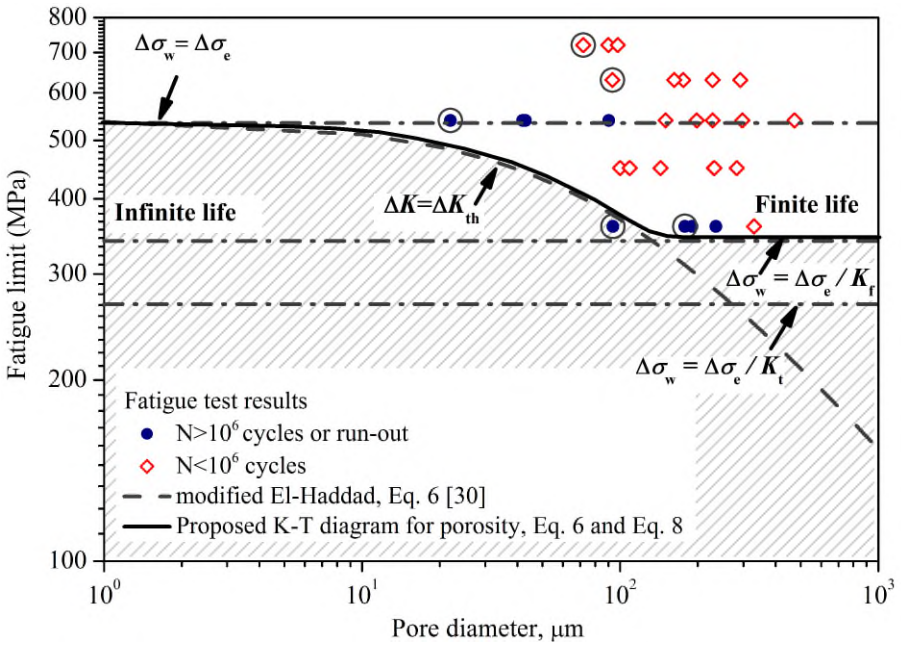

Fig. 7.3 Fatigue limit of WAAM Ti-6Al-4V as a function of porosity diameter. Material's intrinsic fatigue limit is 540 MPa at applied stress ratio 0.1. Note: encircled data points denote crack initiation at internal pores.

The modified K-T diagram for porosity defects with the three limiting conditions (material's intrinsic fatigue limit as upper bound, modified El Haddad's LEFM criterion, and the notch

fatigue limit as the lower bound) was found to agree well with the test results as shown in Fig. 7.3.

7.4 Summary

The objective of the present chapter was to study the correlation between the porosity defect size and the stress intensity factor range. The fatigue test data and finite element modelling results presented in Chapters 5 and 6 were used to arrive at meaningful conclusions. The findings of this chapter can be summarised as follows:

(1) Fatigue life can be correlated with the stress intensity factor range of the crack initiating defect using Murakami's equation, which takes account of both the applied stress level and defect size. The best fit curve of the correlation is discontinuous at the point (or value) corresponding to the threshold stress intensity factor range.

(2) Fatigue strength limit can be predicted by a modified Kitagawa-Takahashi diagram for porosity defects. Instead of using a monotonically decreasing relation of the applied stress range with porosity size, a sigmoidal curve was used in this study to set the lower bound according to the notch fatigue limit.

(3) The critical porosity diameter was found to be close to 100 μm for WAAM Ti-6Al-4V.

Chapter 8

Conclusions and Future Work

8.1 Introduction

This concluding chapter summarises the important findings, novel contributions and final conclusions from the experimental and modelling work presented in this thesis. Subsequently, some suggestions are presented on areas where further research is required, or could be useful, to improve the understanding of the WAAM process and its mechanical properties.

8.2 Novel contributions

This study was conducted with an aim to study the effect of porosity defects on the fatigue performance of wire + arc additive manufactured Ti-6Al-4V. The experimental test plan was designed with two groups of test specimens. First group, referred to as 'reference specimens', was built using the standard processing route and was used to obtain the benchmark material behaviour. The second group, referred to as 'porosity specimens', was built using similar processing parameters as the reference specimens, except for the gauge section being built using a contaminated wire that caused the formation of large isolated pores in the specimens. Important observations were made using these two specimen groups. Finally, a fatigue life prediction method was developed to account for the presence of gas pores that was based on notch-fatigue approach. Further, a linear elastic fracture mechanics model was used to determine the critical size of pore for WAAM Ti-6Al-4V. The novel contributions of the research are presented below.

(1) Porosity characterisation in WAAM Ti-6Al-4V and its evolution under fatigue loading

The size range of pores in the reference specimens was between 50 and 100 μm. Morphology of the pores was spherical or near spherical. No lack of fusion defects were observed. Inter-

rupted fatigue-tomography studies performed on the porosity group specimens showed that with increasing number of fatigue cycles, the pores can grow in size. Some pores grew upto twice of their original size. The changes in the pore morphology can be due to the localised plastic deformation. The interrupted fatigue-tomography experiment also showed that pores located closer to the surface acted as preferred crack initiation sites. Crack initiated at the pore root where the value of stress concentration factor was highest.

(2) Effect of pores on the tensile and fatigue properties of WAAM Ti-6Al-4V

The ductility was found to reduce from 10% to 4% when the material density of the tensile test specimens reduced from 99.99% to 99.96%. However, porosity was found to have little effect on the yield strength (close to 825MPa) and tensile strength (close to 859MPa) of WAAM Ti-6Al-4V. Further, load controlled fatigue tests performed at a stress ratio of 0.1 showed that the fatigue limit ($\Delta\sigma$) of the reference and porosity group specimens was 540 MPa and 360 MPa respectively. The notch fatigue factor for WAAM Ti-6Al-4V with porosity defects was found to be 1.5 and the corresponding notch sensitivity was 0.5. Electron microscopy analysis of the fatigue fracture surface revealed that morphology of the crack path at the vicinity of pore was a function of the applied stress amplitude and the pore size.

(3) Fatigue life prediction method

Finite element analysis (FEA) performed with ideal spherical pore geometry was found to be consistent with the FEA conducted using image based meshing of X-ray computed tomography scans. The stress concentration factor at gas pores was found to be close to 2. The local stress and strain determined using elastic plastic finite element analysis can be used with the strain-life or stress life models for estimating the fatigue life of the specimen. The approach was validated using fatigue test results obtained from this study as well as with published literature.

(4) Modified Kitagawa diagram for gas pores

A plot of fatigue limit vs. porosity diameter should be a sigmoidal curve instead of a monotonically decreasing curve, with the upper limit of asymptote at fatigue limit of defect-free specimens ($\Delta\sigma_w = \Delta\sigma_e$) and the lower limit at the value of fatigue limit reduced by a factor equal to the stress concentration factor of gas pores, the notch fatigue limit ($\Delta\sigma_w = \Delta\sigma_e/K_t$). This diagram suggests that the critical pore size for WAAM Ti-6Al-4V is 100 μm.

8.3 Conclusions

The purpose of this thesis was to determine the role of porosity defects on the fatigue performance of WAAM Ti-6Al-4V. The findings of the research are summarised as follows.

8.3.1 Experimental studies

The material manufacturing strategy involved 2 specimen groups, (a) reference and (b) porosity. The reference specimens represented the inherent material behaviour while the porosity specimens included pores in the gauge section due to the use of contaminated wires. Tensile and fatigue tests were performed on the two specimen groups to experimentally determine the effect of pores on the strength and ductility values of WAAM Ti-6Al-4V. Tensile strength reduction due to pores was negligible, while the ductility dropped by 60%. Consequently, the fatigue performance was also affected by the presence of pores. Fatigue strength of the porosity specimens was 33% lower than the reference specimens. It is worth mentioning that some of the reference specimens also revealed crack initiation at pore which had a size comparable to the α colony (20 μm to 30 μm). Such pores resulted in a fatigue strength reduction of 8% with respect to the reference specimens where crack initiation was at α lamellae. Further, displacement controlled cyclic load testing showed that WAAM Ti-6Al-4V exhibits an overall cyclic softening behaviour. This indicates that while conducting fatigue tests at positive stress ratios, the mean stress at the regions of stress concentration would be lower than the applied value due to the mean stress relaxation effect. Interrupted fatigue - tomography testing showed that crack was initiated at more than one pore and the pores located closer to the free surface were more prone towards initiating cracks. The crack path was highly tortuous and directed towards the nearest free surface of the specimen. Additionally, the pores were observed to grow with increasing number of fatigue cycles. This can be explained by the plastic strain accumulation at the pore root during each fatigue cycle. Therefore, with the quantitative effect of porosity on the tensile and fatigue behaviour of WAAM Ti-6Al-4V was studied. Further, the X-ray CT analysis indicated the effect of porosity characteristics, i.e shape and location of pore, on the fatigue crack initiation behaviour. Such new information has helped in understanding the role of porosity in fatigue damage and in developing more better predictive models.

8.3.2 Fatigue life prediction

Elastic stress analysis showed that the value of stress concentration factor (K_t) for gas pores is 2. Since the specimen size is generally much larger than the pore size, it can be inferred that the value of K_t for gas pores is independent of the size of pore. In case of surface pores, the bottom of the pore, which is constrained on either sides by symmetry boundary condition, was found to be the pore root. Consequently, the value of K_t for internal and surface locations of pore was found to be very close due to the similar boundary condition acting at the pore root. Subsurface location of pores was most critical, with the value of K_t increasing exponentially as the distance between the edge of the pore and the free surface reduces. In addition to pore location, pore morphology also affects K_t. Oval pores exhibited a K_t of 2.5, which is 25% higher than the value of K_t for a spherical pore. The mixed isotropic-kinematic hardening/softening model was calibrated with WAAM Ti-6Al-4V and SLM Ti-6Al-4V to compute the local stress and strain values for the WAAM Ti-6Al-4V specimens tested in this study and published studies on powder bed fusion processed Ti-6Al-4V respectively. Fatigue life of the specimen was predicted using the notch-fatigue approach where the local stress-strain values govern the fatigue crack initiation like. Mean stress effect was considered by the Smith-Watson-Topper [99] model. The significance of this study is in improving the accuracy of predictive models which can increase the reliability of the material and enhance the acceptance of additive manufacturing technology in the commercial sectors.

8.3.3 Fatigue limit prediction

Finite Element Analysis does not address the size effect of porosity defects, however, some of the experimental tests indicated that when the pore size is comparable to the size of the surrounding α lamellae, the fatigue life was much higher than that predicted using local stress-strain values. The enhanced fatigue life is caused due to the microstructural interactions with the micro crack originating at the pore. Subsequently, the stress intensity factor range for pores calculated using Murakami's model [74] and used as a fatigue design parameter the square root area parameter as an equivalent crack length for porosity defects. Further, Beretta and Romano's [87] modified El-Haddad model was used to set the non-propagating crack boundary for the porosity defects. This boundary was unified with the material's intrinsic fatigue limit and the notch fatigue limit, both values obtained from the fatigue testing performed with the reference and porosity specimens. Therefore, a modified Kitagawa-Takahashi (KT) diagram was proposed for the gas pores and

was validated with the fatigue test results. The modified KT diagram suggested that the critical size of porosity in WAAM Ti-6Al-4V is 100μm.

8.4 Outlook for future work

While the research documented within this thesis has shed new light on the characteristics of process induced gas pores and its effect on mechanical properties in WAAM Ti-6Al-4V, there is still work to be done to engineer them out of the process and further characterise the fatigue behaviour of the material. Some suggestions for further investigations, based on the current findings are listed below:

(1) Interrupted fatigue test with X-ray computed tomography scans is a very powerful techniques to monitor the changes in pore morphology and further studies are required to add on to the findings of the present thesis.

(2) Microstructural studies on WAAM Ti-6Al-4V showed large varations in the α grain morphology from location to location. Such variations can make it difficult to maintain repeatability in the part performance and therefore better scanning strategies may be developed to established a more uniform cooling rate. In addition, a thermal model can be a useful tool on this context since it can be adapted to any arbitrary part geometry to estimate the thermal history at different sections of the part. Thus, a thermal model could help efforts to better predict and control the crystal structure within AM material, as well as avoid porosity.

(3) Diffraction contrast tomography (DCT) can be used to calculate in 3D the size and crystallographic orientations of grains down to around 10 μm in size. Thefine microstructure of SEBM samples is likely to make it difficult or impossible to distinguish individual α laths, but colonies of similarly orientated grains may be detectable. The detection of such small grains by DCT would also necessitate the use of smaller samples (less than 1mm). It could be useful to create a model alloy, with larger grains and pores, to test the technique prior to using it on WAAM Ti-6Al-4V samples.

(4) Alternatively, electron back-scatter diffraction (EBSD) could be used to achieve a resolution high enough to distinguish individual α laths in WAAM Ti-6Al-4V, with the limitation being that the information is obtained for a single plane. Measuring the crystallographic orientation around crack initiating pores that with different stress intensity factor but similar fatigue life, may be studied using EBSD. The Schmidt factor of grains surrounding a pore can be calculated and then implemented into the $\Delta Kvs.N$ relationship to achieve better correlation.

References

[1] B. Dutta, V. Singh, H. Natu, J. Choi, and J. Mazumder, "Direct Metal Deposition," *Adv. Mater. Process*, vol. 167, no. 3, pp. 33–36, 2009. [Online]. Available: http://mbraun.com/images/201/POMGroup.pdf

[2] S. Katani, F. Madadi, M. Atapour, and S. Ziaei Rad, "Micromechanical modelling of damage behaviour of Ti-6Al-4V," *Materials and Design*, vol. 49, pp. 1016–1021, 2013. [Online]. Available: https://doi.org/10.1016/j.matdes.2013.02.021

[3] Y. Zhai, H. Galarraga, and D. A. Lados, "Microstructure, static properties, and fatigue crack growth mechanisms in Ti-6Al-4V fabricated by additive manufacturing: LENS and EBM," *Engineering Failure Analysis*, vol. 114, pp. 658–666, 2016. [Online]. Available: http://linkinghub.elsevier.com/retrieve/pii/S1350630716303752

[4] S. Tammas-Williams, H. Zhao, F. Léonard, F. Derguti, I. Todd, and P. Prangnell, "XCT analysis of the influence of melt strategies on defect population in Ti–6Al–4V components manufactured by Selective Electron Beam Melting," *Materials Characterization*, vol. 102, pp. 47–61, apr 2015. [Online]. Available: http://www.sciencedirect.com/science/article/pii/S104458031500039X

[5] D. Agius, K. I. Kourousis, C. Wallbrink, and T. Song, "A Cyclic plasticity and microstructure of as-built SLM Ti-6Al-4V : The effect of build orientation," *Materials Science & Engineering A*, vol. 701, no. May, pp. 85–100, 2017. [Online]. Available: http://dx.doi.org/10.1016/j.msea.2017.06.069

[6] P. Edwards and M. Ramulu, "Fatigue performance evaluation of selective laser melted Ti–6Al–4V," *Materials Science and Engineering: A*, vol. 598, pp. 327–337, 2014. [Online]. Available: http://linkinghub.elsevier.com/retrieve/pii/S0921509314000720

[7] K. D. Rekedal, "Investigation of the High cycle Fatigue Life of Selective Laser Melted and Hot Isostatically Pressed Ti-6Al-4V," *MSc Thesis,, Air force institute of technology, US*, 2015.

[8] H. K. Rafi, T. L. Starr, and B. E. Stucker, "A comparison of the tensile, fatigue, and fracture behavior of Ti–6Al–4V and 15-5 PH stainless steel parts made by selective laser melting," *The International Journal of Advanced Manufacturing Technology*, vol. 69, no. 5-8, pp. 1299–1309, nov 2013. [Online]. Available: http://link.springer.com/10.1007/s00170-013-5106-7

[9] B. V. Hooreweder, R. Boonen, D. Moens, J.-p. Kruth, and P. Sas, "On the determination of fatigue properties of Ti6Al4V produced by selective laser melting," *Structural Dynamics and Materials Conference*, no. April, pp. 1–9, 2012.

[10] S. Leuders, M. Thöne, A. Riemer, T. Niendorf, T. Tröster, H. Richard, and H. Maier, "On the mechanical behaviour of titanium alloy TiAl6V4 manufactured by selective laser melting: Fatigue resistance and crack growth performance," *International Journal of Fatigue*, vol. 48, pp. 300–307, 2013. [Online]. Available: http://linkinghub.elsevier.com/retrieve/pii/S014211231200343X

[11] G. Kasperovich and J. Hausmann, "Improvement of fatigue resistance and ductility of TiAl6V4 processed by selective laser melting," *Journal of Materials Processing Technology*, vol. 220, pp. 202–214, 2015. [Online]. Available: http://dx.doi.org/10.1016/j.jmatprotec.2015.01.025

[12] H. K. Rafi, N. V. Karthik, H. Gong, T. L. Starr, and B. E. Stucker, "Microstructures and Mechanical Properties of Ti6Al4V Parts Fabricated by Selective Laser Melting and Electron Beam Melting," vol. 22, no. December, pp. 3872–3883, 2013.

[13] E. Brandl, F. Palm, V. Michailov, B. Viehweger, and C. Leyens, "Mechanical properties of additive manufactured titanium (Ti-6Al-4V) blocks deposited by a solid-state laser and wire," *Materials and Design*, vol. 32, no. 10, pp. 4665–4675, 2011. [Online]. Available: http://dx.doi.org/10.1016/j.matdes.2011.06.062

[14] F. Wang, S. Williams, P. A. Colegrove, and A. A. Antonysamy, "Microstructure and mechanical properties of wire and arc additive manufactured Ti-6Al-4V," *Metallurgical and Materials Transactions A: Physical Metallurgy and Materials Science*, vol. 44, no. 2, pp. 968–977, 2013.

[15] "Wire+Arc Additive Manufacturing website," 2018. [Online]. Available: https://waammat.com/documents

[16] "Metallic Materials Properties Development and Standardization (MMPDS)," no. 4, pp. 72, chapter 5, 2008.

[17] A. Phaiboonworachat and K. Kourousis, "Cyclic elastoplastic behaviour, hardness and microstructural properties of Ti-6Al-4V manufactured through selective laser melting," *International Journal of Materials Engineering Innovation*, vol. 7, no. 1, pp. 80–87, 2016.

[18] A. J. Sterling, B. Torries, N. Shamsaei, S. M. Thompson, and D. W. Seely, "Fatigue behavior and failure mechanisms of direct laser deposited Ti-6Al-4V," *Materials Science and Engineering A*, vol. 655, pp. 100–112, 2016. [Online]. Available: http://dx.doi.org/10.1016/j.msea.2015.12.026

[19] E. Wycisk, A. Solbach, S. Siddique, D. Herzog, F. Walther, and C. Emmelmann, "Effects of defects in laser additive manufactured Ti-6Al-4V on fatigue properties," *Physics Procedia*, vol. 56, pp. 371–378, 2014. [Online]. Available: http://linkinghub.elsevier.com/retrieve/pii/S187538921400265X

[20] M. Kahlin, H. Ansell, and J. J. Moverare, "Fatigue behaviour of notched additive manufactured Ti6Al4V with as-built surfaces," *International Journal of Fatigue*, vol. 101, pp. 51–60, 2017. [Online]. Available: http://dx.doi.org/10.1016/j.ijfatigue.2017.04.009

[21] D. Greitemeier, C. Dalle Donne, F. Syassen, J. Eufinger, and T. Melz, "Effect of surface roughness on fatigue performance of additive manufactured Ti–6Al–4V," *Materials Science and Technology*, no. 28th ICAF symposium, pp. 12–20, 2015. [Online]. Available: http://www.maneyonline.com/doi/abs/10.1179/1743284715Y.0000000053

[22] T. Nicholas, *High Cycle Fatigue - A Mechanics of Materials Perspective*, 2006.

[23] S. Bagehorn, J. Wehr, and H. J. Maier, "Application of mechanical surface finishing processes for roughness reduction and fatigue improvement of additively manufactured Ti-6Al-4V parts," *International Journal of Fatigue*, vol. 102, pp. 135–142, 2017. [Online]. Available: http://dx.doi.org/10.1016/j.ijfatigue.2017.05.008

[24] N. Hrabe, T. Gnaupel-Herold, and T. Quinn, "Fatigue properties of a titanium alloy (Ti-6Al-4V) fabricated via electron beam melting (EBM): Effects of internal defects and residual stress," *International Journal of Fatigue*, vol. 94, pp. 202–210, 2015. [Online]. Available: http://dx.doi.org/10.1016/j.ijfatigue.2016.04.022

[25] X. Shui, K. Yamanaka, M. Mori, Y. Nagata, and A. Chiba, "Effects of post processing on cyclic fatigue response of a titanium alloy addtively manufactured by electrom beam melting," *Materials Science & Engineering A*, vol. 680, pp. 239–248, 2017. [Online]. Available: http://dx.doi.org/10.1016/j.msea.2016.10.059

[26] M. Ackelid,U, Svensson, "Additive manufacturing of dense metal parts by electron beam melting," pp. 2711–9, 2009.

[27] Leuders, S. and Lieneke, T. and Lammers, S. and Troster, T., "On the fatigue properties of metals manufactured by selective laser melting – The role of ductility," pp. 1–9, 2014.

[28] Y. M. Hiroshige Masuo, Yuzo Tanaka, Shotaro Morokoshi, Hajime Yagura, Tetsuya Uchida, Yasuhiro Yamamoto, "Effects of Defects , Surface Roughness and HIP on Fatigue of Ti-6Al-4V manufactured by Additive Manufacturing," *Procedia Structural integrity*, vol. 7, pp. 19–26, 2017.

[29] G. Dieter and D. Bacon, *Mechanical Metallurgy*, ser. Materials Science and Engineering Series. McGraw-Hill, 1988. [Online]. Available: https://books.google.co.uk/books?id=hlabmB3e8XwC

[30] J. Schijve, *Fatigue of structures, Chapter 8*, 2004.

[31] S. Timoshenko and J. N. Goodier, *Theory of Elasticity*, 1st ed. McGraw-Hill, 1951. [Online]. Available: http://www.amazon.com/Elasticity-McGraw-Hill-Classic-Textbook-Reissue/dp/0070858055

[32] R.A. Eubanks, "Stress concentration due to a hemispherical pit at a free surface," Tech. Rep., 1953.

[33] W. D. Pilkey and D. F. Pilkey, *Peterson's Stress Concentration Factors, Third Edition*, 2008.

[34] A. A. Antonysamy, "Microstructure , texture and mechanical property evolution during additive manufacturing of Ti6Al4V alloy for aerospace applications, PhD thesis, Manchester university, UK," Ph.D. dissertation, 2012.

[35] B. Dutta and F. H. Froes, "Additive manufacturing of titanium alloys," *Additive Manufacturing Handbook: Product Development for the Defense Industry*, vol. 72, no. 2, pp. 263–274, 2017. [Online]. Available: http://dx.doi.org/10.1016/j.mprp.2016.12.062

[36] B. Sampson, "Finland flies 3D-printed engine parts for the first time," *Aerospace testing international, January*, 2018. [Online]. Available: https://www.aerospacetestinginternational.com/news/engine-testing/finland-flies-3d-printed-engine-parts-for-the-first-time.html

[37] Sampson, B., "Boeing backs titanium fusion bed process for 3D printing," *Aerospace testing international, February*, 2018. [Online]. Available: https://www.aerospacetestinginternational.com/news/industry-news/boeing-backs-titanium-fusion-bed-process-for-3d-printing.html

[38] A. James, "First titanium 3D-printed part installed into serial production aircraft," *Aerospace testing international, September*, 2017. [Online]. Available: https://www.aerospacetestinginternational.com/news/industry-news/first-titanium-3d-printed-part-installed-into-serial-production-aircraft.html

[39] P. Li, D. Warner, A. Fatemi, and N. Phan, "Critical assessment of the fatigue performance of additively manufactured Ti-6Al-4V and perspective for future research," *International Journal of Fatigue*, vol. 85, pp. 130–143, 2016. [Online]. Available: http://linkinghub.elsevier.com/retrieve/pii/S0142112315004399

[40] H. P. Tang, M. Qian, N. Liu, X. Z. Zhang, G. Y. Yang, and J. Wang, "Effect of Powder Reuse Times on Additive Manufacturing of Ti-6Al-4V by Selective Electron Beam Melting," *JOM*, vol. 67, no. 3, pp. 555–563, feb 2015. [Online]. Available: http://link.springer.com/10.1007/s11837-015-1300-4

[41] M. K. Thompson, G. Moroni, T. Vaneker, G. Fadel, R. I. Campbell, I. Gibson, A. Bernard, J. Schulz, P. Graf, B. Ahuja, and F. Martina, "Design for Additive Manufacturing: Trends, opportunities, considerations, and constraints," *CIRP Annals - Manufacturing Technology*, vol. 65, no. 2, pp. 737–760, 2016. [Online]. Available: http://linkinghub.elsevier.com/retrieve/pii/S0007850616301913

[42] C. R. Cunningham, J. M. Flynn, a. Shokrani, V. Dhokia, and S. T. Newman, "Invited review article: Strategies and processes for high quality wire arc additive manufacturing," *Additive Manufacturing*, vol. 22, no. June, pp. 672–686, 2018. [Online]. Available: https://doi.org/10.1016/j.addma.2018.06.020

[43] P. A. Colegrove, J. Donoghue, F. Martina, J. Gu, P. Prangnell, and J. Hönnige, "Scripta Materialia Application of bulk deformation methods for microstructural and material property improvement and residual stress and distortion control in additively manufactured components," *Scripta Materialia*, vol. 135, pp. 111–118, 2017. [Online]. Available: http://dx.doi.org/10.1016/j.scriptamat.2016.10.031

[44] J. R. Hönnige, P. A. Colegrove, B. Ahmad, M. E. Fitzpatrick, S. Ganguly, T. L. Lee, and S. W. Williams, "Residual stress and texture control in Ti-6Al-4V wire + arc additively manufactured intersections by stress relief and rolling," *Materials and Design*, vol. 150, no. 2017, pp. 193–205, 2018. [Online]. Available: https://doi.org/10.1016/j.matdes.2018.03.065

[45] D. Agius, M. Kajtaz, K. Kourousis, C. Wallbrink, C. Wang, W. Hu, and J. Silva, "Sensitivity and optimisation of the Chaboche plasticity model parameters in strain-life fatigue predictions," *Materials and Design*, vol. 118, pp. 107–121, 2017. [Online]. Available: http://dx.doi.org/10.1016/j.matdes.2017.01.027

[46] J. Yang, H. Yu, J. Yin, M. Gao, Z. Wang, and X. Zeng, "Formation and control of martensite in Ti-6Al-4V alloy produced by selective laser melting," *Materials & Design*, vol. 108, pp. 308–318, 2016. [Online]. Available: http://linkinghub.elsevier.com/retrieve/pii/S0264127516308796

[47] T. A. Book and M. D. Sangid, "Materials Characterization Strain localization in Ti-6Al-4V Widmanstätten microstructures produced by additive manufacturing," *Materials Characterization*, vol. 122, pp. 104–112, 2016. [Online]. Available: http://dx.doi.org/10.1016/j.matchar.2016.10.018

[48] M. Simonelli, *Microstructure evolution and mechanical properties of Selective Laser Melted Ti-6Al-4V*, 2014, no. PhD Thesis, Loughborough University.

[49] M. Seifi, M. Dahar, O. Harrysson, J. Beuth, and J. J. Lewandowski, "Evaluation of Orientation Dependence of Fracture Toughness and Fatigue Crack Growth Behavior of as-deposited ARCAM EBM Ti-6Al- 4V," no. February 2016, 2015.

[50] W. Xu, M. Brandt, S. Sun, J. Elambasseril, Q. Liu, K. Latham, K. Xia, and M. Qian, "Additive manufacturing of strong and ductile Ti-6Al-4V by selective laser melting via in situ martensite decomposition," *Acta Materialia*, vol. 85, pp. 74–84, 2015.

[51] G. Lutjering and J. Williams, *Engineering Materials and Processes - Titanium*, 2nd ed., 2007.

[52] D. Greitemeier, F. Palm, F. Syassen, and T. Melz, "Fatigue performance of additive manufactured TiAl6V4 using electron and laser beam melting," *International Journal of Fatigue*, vol. 44, no. 2, pp. 211–217, 2016. [Online]. Available: http://dx.doi.org/10.1016/j.ijfatigue.2016.05.001

[53] W. Xu, S. Sun, J. Elambasseril, Q. Liu, M. Brandt, and M. Qian, "Ti-6Al-4V Additively Manufactured by Selective Laser Melting with Superior Mechanical Properties," *Jom*, vol. 67, no. 3, pp. 1–6, 2015. [Online]. Available: http://dx.doi.org/10.1007/s11837-015-1297-8

[54] M. Simonelli, Y. Y. Tse, and C. Tuck, "Effect of the build orientation on the mechanical properties and fracture modes of SLM Ti-6Al-4V," *Materials Science and Engineering A*, vol. 616, pp. 1–11, 2014. [Online]. Available: http://dx.doi.org/10.1016/j.msea.2014.07.086

[55] T. Ahmed and H. Rack, "Phase transformations during cooling in α+β titanium alloys," *Materials Science and Engineering: A*, vol. 243, no. 1-2, pp. 206–211, 1998. [Online]. Available: http://linkinghub.elsevier.com/retrieve/pii/S0921509397008022

[56] R. Shi, V. Dixit, H. L. Fraser, and Y. Wang, "Variant selection of grain boundary α by special prior β grain boundaries in titanium alloys," *Acta Materialia*, vol. 75, pp. 156–166, 2014. [Online]. Available: http://dx.doi.org/10.1016/j.actamat.2014.05.003

[57] F. Martina, P. A. Colegrove, S. W. Williams, and J. Meyer, "Microstructure of interpass rolled wire + arc additive manufacturing Ti-6Al-4V components," *Metallurgical and Materials Transactions A: Physical Metallurgy and Materials Science*, vol. 46, no. 12, pp. 6103–6118, 2015.

[58] J. J. Lin, Y. H. Lv, Y. X. Liu, B. S. Xu, Z. Sun, Z. G. Li, and Y. X. Wu, "Microstructural evolution and mechanical properties of Ti-6Al-4V wall deposited by pulsed plasma arc additive manufacturing," vol. 102, pp. 30–40, 2016.

[59] M. J. Bermingham, D. Kent, H. Zhan, D. H. Stjohn, and M. S. Dargusch, "Controlling the microstructure and properties of wire arc additive manufactured Ti-6Al-4V with trace boron additions," *Acta Materialia*, vol. 91, pp. 289–303, 2015. [Online]. Available: http://dx.doi.org/10.1016/j.actamat.2015.03.035

[60] S. Leuders, M. Vollmer, F. Brenne, T. Tröster, and T. Niendorf, "Fatigue strength prediction for titanium alloy TiAl6V4 manufactured by selective laser melting," *Metallurgical and Materials Transactions A*, vol. 46, no. 9, pp. 3816–3823, 2015. [Online]. Available: http://link.springer.com/10.1007/s11661-015-2864-x

[61] J. Günther, D. Krewerth, T. Lippmann, S. Leuders, T. Tröster, A. Weidner, H. Biermann, and T. Niendorf, "Fatigue life of additively manufactured Ti-6Al-4V in the very high cycle fatigue regime," *International Journal of Fatigue*, vol. 94, pp. 236–245, 2016.

[62] K. S. Chan, "Roles of microstructure in fatigue crack initiation," *International Journal of Fatigue*, vol. 32, no. 9, pp. 1428–1447, 2010. [Online]. Available: http://dx.doi.org/10.1016/j.ijfatigue.2009.10.005

[63] H. Zhang, Y. Xie, D. Rui, and G. Wang, "Hybrid deposition and micro rolling manufacturing method of metallic parts," *24th International SFF Symposium - An Additive Manufacturing Conference, SFF 2013*, pp. 267–281, 2013. [Online]. Available: http://www.scopus.com/inward/record.url?eid=2-s2.0-84898427610{&}partnerID=40{&}md5=306c5e320817f794a23515eeba4eb98c

[64] P. A. Colegrove, F. Martina, M. J. Roy, B. A. Szost, S. Terzi, S. W. Williams, P. J. Withers, and D. Jarvis, "High Pressure Interpass Rolling of Wire + Arc Additively Manufactured Titanium Components," *Advanced Materials Research*, vol. 996, pp. 694–700, 2014. [Online]. Available: http://www.scientific.net/AMR.996.694

[65] A. R. McAndrew, M. Alvarez Rosales, P. A. Colegrove, J. R. Hönnige, A. Ho, R. Fayolle, K. Eyitayo, I. Stan, P. Sukrongpang, A. Crochemore, and Z. Pinter, "Interpass rolling of Ti-6Al-4V wire + arc additively manufactured features for microstructural refinement," *Additive Manufacturing*, vol. 21, no. February, pp. 340–349, 2018. [Online]. Available: https://doi.org/10.1016/j.addma.2018.03.006

[66] S. Tammas-Williams, P. J. Withers, I. Todd, and P. B. Prangnell, "The influence of porosity on fatigue crack initiation in additively manufactured titanium components," *Scientific Reports*, pp. 1–13, 2017. [Online]. Available: http://dx.doi.org/10.1038/s41598-017-06504-5

[67] S. Siddique, M. Awd, J. Tenkamp, and F. Walther, "Development of a stochastic approach for fatigue life prediction of AlSi12 alloy processed by selective laser melting," *Engineering Failure Analysis*, vol. 79, pp. 34–50, 2017. [Online]. Available: http://linkinghub.elsevier.com/retrieve/pii/S1350630717300894

[68] S. Tammas-Williams, P. Withers, I. Todd, and P. Prangnell, "Porosity regrowth during heat treatment of hot isostatically pressed additively manufactured titanium components," *Scripta Materialia*, vol. 122, pp. 72–76, 2016. [Online]. Available: http://linkinghub.elsevier.com/retrieve/pii/S1359646216301737

[69] C. Qiu, G. A. Ravi, C. Dance, A. Ranson, S. Dilworth, and M. M. Attallah, "Fabrication of large Ti-6Al-4V structures by direct laser deposition," *Journal of Alloys and Compounds*, vol. 629, pp. 351–361, 2015. [Online]. Available: http://dx.doi.org/10.1016/j.jallcom.2014.12.234

[70] B. Baufeld, O. V. D. Biest, and R. Gault, "Additive manufacturing of Ti–6Al–4V components by shaped metal deposition: Microstructure and mechanical properties," *Materials & Design*, vol. 31, pp. S106–S111, 2010. [Online]. Available: http://linkinghub.elsevier.com/retrieve/pii/S0261306909006529

[71] B. E. Carroll, T. a. Palmer, and A. M. Beese, "Anisotropic tensile behavior of Ti-6Al-4V components fabricated with directed energy deposition additive manufacturing," *Acta Materialia*, vol. 87, pp. 309–320, 2015. [Online]. Available: http://dx.doi.org/10.1016/j.actamat.2014.12.054

[72] C. L. A. Leung, S. Marussi, R. C. Atwood, M. Towrie, P. J. Withers, and P. D. Lee, "In situ X-ray imaging of defect and molten pool dynamics in laser additive manufacturing," *Nature Communications*, vol. 9, no. 1, pp. 1–9, 2018. [Online]. Available: http://dx.doi.org/10.1038/s41467-018-03734-7

[73] P. Li, P. D. Lee, D. M. Maijer, and T. C. Lindley, "Quantification of the interaction within defect populations on fatigue behavior in an aluminum alloy," *Acta Materialia*, vol. 57, no. 12, pp. 3539–3548, 2009. [Online]. Available: http://dx.doi.org/10.1016/j.actamat.2009.04.008

[74] Y. Murakami, *Metal fatigue: Effects of Small Defects and Nonmetallic Inclusions*, 1st ed. Elsevier, 2002.

[75] I. Bantounas, D. Dye, and T. C. Lindley, "The effect of grain orientation on fracture morphology during high-cycle fatigue of Ti-6Al-4V," *Acta Materialia*, vol. 57, no. 12, pp. 3584–3595, 2009.

[76] K. S. Chan, M. Koike, R. L. Mason, and T. Okabe, "Fatigue Life of Titanium Alloys Fabricated by Additive Layer Manufacturing Techniques for Dental Implants," *Metallurgical and Materials Transactions A*, vol. 44, no. 2, pp. 1010–1022, 2012. [Online]. Available: http://link.springer.com/10.1007/s11661-012-1470-4

[77] S. Suresh, *Fatigue of Materials*, 1998. [Online]. Available: http://ebooks.cambridge.org/ref/id/CBO9780511806575

[78] R. K. Nalla, B. L. Boyce, J. P. Campbell, J. O. Peters, and R. O. Ritchie, "Influence of microstructure on high-cycle fatigue of Ti-6Al-4V: Bimodal vs. lamellar structures," *Metallurgical and Materials Transactions A*, vol. 33, no. 13, pp. 899–918, 2002.

[79] G. Härkegrd and G. Halleraker, "Assessment of methods for prediction of notch and size effects at the fatigue limit based on test data by Böhm and Magin," *International Journal of Fatigue*, vol. 32, no. 10, pp. 1701–1709, 2010. [Online]. Available: http://dx.doi.org/10.1016/j.ijfatigue.2010.03.011

[80] S. Romano, a. Brandão, J. Gumpinger, M. Gschweitl, and S. Beretta, "Qualification of AM parts: Extreme value statistics applied to tomographic measurements," *Materials and Design*, vol. 131, no. April, pp. 32–48, 2017.

[81] S. Beretta, G. Chai, and E. Soffiati, "A weakest–link analysis for fatigue strength of components containing defects," in *Convegno IGF XVII Bologna 2004*, 2008. [Online]. Available: http://www.gruppofrattura.it/ocs/index.php/cigf/igf17/paper/view/272/0

[82] F. Bridier, D. L. McDowell, P. Villechaise, and J. Mendez, "Crystal plasticity modeling of slip activity in Ti-6Al-4V under high cycle fatigue loading," *International Journal of Plasticity*, vol. 25, no. 6, pp. 1066–1082, 2009. [Online]. Available: http://dx.doi.org/10.1016/j.ijplas.2008.08.004

[83] F. Morel, R. Guerchais, and N. Saintier, "Competition between microstructure and defect in multiaxial high cycle fatigue," in *In: Multiaxial Fatigue Workshop, Italie*, 2015.

[84] M. Zhang, J. Zhang, and D. L. Mcdowell, "Microstructure-based crystal plasticity modeling of cyclic deformation of Ti – 6Al – 4V," vol. 23, pp. 1328–1348, 2007.

[85] B. Romali, Z. Xiang, S. Abdul Khadar, A. Mustafa, D. Jialuo, W. Frank, and W. Stewart, "Criticality of porosity defects on the fatigue performance of wire + arc additive manufactured titanium alloy," *International Journal of Fatigue*, p. (submitted), 2018.

[86] G. Härkegård, "Short-crack modelling of the effect of corrosion pits on the fatigue limit of 12% Cr steel," *Fatigue & Fracture of Engineering Materials & Structures*, vol. 38, no. 9, pp. 1009–1016, 2015. [Online]. Available: http://doi.wiley.com/10.1111/ffe.12305

[87] S. Beretta and S. Romano, "A comparison of fatigue strength sensitivity to defects for materials manufactured by AM or traditional processes," *International Journal of Fatigue*, vol. 94, pp. 178–191, 2017. [Online]. Available: http://dx.doi.org/10.1016/j.ijfatigue.2016.06.020

[88] G. Härkegård, "Comparison between different methods for the prediction of the fatigue limit of a member with a small crack," *Procedia Structural Integrity*, vol. 7, pp. 343–350, 2017. [Online]. Available: http://linkinghub.elsevier.com/retrieve/pii/S2452321617304547

[89] M. H. El Haddad, T. H. Topper, and K. N. Smith, "Prediction of non propagating cracks," *Engineering Fracture Mechanics*, vol. 11, no. 3, pp. 573–584, 1979.

[90] R. Cunningham, A. Nicolas, J. Madsen, E. Fodran, M. D. Sangid, and A. D. Rollett, "Analyzing the effects of powder and post- processing on porosity and properties of electron beam melted Ti-6Al-4V," *Materials research letters*, vol. 5, no. October, pp. 516–525, 2017.

[91] M. Benedetti and V. Fontanari, "The effect of bi-modal and lamellar microstructures of Ti-6Al-4V on the behaviour of fatigue cracks emanating from edge-notches," *Fatigue and Fracture of Engineering Materials and Structures*, vol. 27, no. 11, pp. 1073–1089, 2004.

[92] J. D. Eshelby and P. R. S. L. A, "The Determination of the Elastic Field of an Ellipsoidal Inclusion , and Related Problems Article cited in :," pp. 376–396, 1957.

[93] S. Siddique, M. Imran, M. Rauer, M. Kaloudis, E. Wycisk, C. Emmelmann, and F. Walther, "Computed tomography for characterization of fatigue performance of selective laser melted parts," *Materials and Design*, vol. 83, pp. 661–669, 2015. [Online]. Available: http://dx.doi.org/10.1016/j.matdes.2015.06.063

[94] S. M. J. Razavi and F. Berto, "ScienceDirect Fatigue strength of notched specimens made of Ti-6Al-4V produced by SLM technique," *Procedia Structural Integrity*, vol. 00, no. 2452, pp. 0–4, 2018. [Online]. Available: https://doi.org/10.1016/j.prostr.2018.12.013

[95] N. Heinz, R. Fritjof Anderson, and J. S. Brock, 1937.

[96] O. H. Basquin, "The exponential law of endurance test." *Proceedings of the American Society for Testing and Materials*, vol. 10, pp. 625–630, 1910.

[97] L. F. J. Coffin, "A study of the effects of cyclic thermal stresses on a ductile metal." *Transactions of the ASME*, vol. 76, pp. 931–950, 1954.

[98] S. S. Manson, "Behavior of materials under conditions of thermal stress." *National Advisory Committee for Aeronautics NACA TN-2933*, 1953.

[99] K. Smith, T. H. Topper, and P. Watson, "A stress-strain function for the fatigue of metals(Stress-strain function for metal fatigue including mean stress effect)," *Journal of materials*, vol. 5, no. April, pp. 767–778, 1970.

[100] J. Morrow, *Fatigue design handbook*, 2nd ed., 1968.

[101] N. E. Dowling, "Mean Stress Effects in Stress-Life and Strain-Life Fatigue," *2nd SAE Brasil International Conference on Fatigue*, 2004.

[102] A. Thant, Y. Miyashita, Y. Otsuka, Y. Mutoh, and S. Sakurai, "Notch fatigue behavior of Ti-6Al-4V alloy in transition region between low and high cycle fatigue," *International Journal of Fatigue*, vol. 95, pp. 194–203, 2017. [Online]. Available: http://dx.doi.org/10.1016/j.ijfatigue.2016.10.024

[103] P. E. Carrion, N. Shamsaei, S. R. Daniewicz, and R. D. Moser, "Fatigue behavior of Ti-6Al-4V ELI including mean stress effects," *International Journal of Fatigue*, vol. 99, pp. 87–100, 2017. [Online]. Available: http://linkinghub.elsevier.com/retrieve/pii/S0142112317300671

[104] Y. Murakami, M. S. Ferdous, and C. Makabe, "Low cycle fatigue damage and critical crack length affecting loss of fracture ductility," *International Journal of Fatigue*, vol. 82, pp. 89–97, jan 2016. [Online]. Available: http://www.sciencedirect.com/science/article/pii/S0142112315001553

[105] H. Kitagawa and S. Takahashi, "Applicability of fracture mechanics to very small cracks or the cracks in the early stage," in *In: Proc 2nd Int conf mech behaviour of mater - ICM2*, 1976, pp. 627–31.

[106] R. W. Hertzberg, *Deformation and fracture mechanics of engineering materials*, 4th ed. Wiley, 1989.

[107] H. O. F. Ralph I. Stephens, Ali Fatemi, Robert R. Stephens, *Metal Fatigue in Engineering*, 2nd ed. Wiley and sons, 2000.

[108] T. Anderson and T. Anderson, *Fracture Mechanics: Fundamentals and Applications, Third Edition*. Taylor & Francis, 2005. [Online]. Available: https://books.google.co.uk/books?id=aBEUjCPMwyAC

[109] U. Zerbst, M. Madia, M. Vormwald, and H. T. Beier, "Fatigue strength and fracture mechanics – A general perspective," *Engineering Fracture Mechanics*, vol. 198, pp. 2–23, 2018. [Online]. Available: https://doi.org/10.1016/j.engfracmech.2017.04.030

[110] S. Pearson, "Initiation of fatigue cracks in commercial aluminium alloys and the subsequent propagation of very short cracks," *Engineering Fracture Mechanics*, vol. 7, no. 2, 1975.

[111] S. Suresh and R. O. Ritchie, "Propagation of short fatigue cracks," *International Metals Reviews*, vol. 29, no. 1, pp. 445–475, 1984. [Online]. Available: http://www.tandfonline.com/doi/full/10.1179/imtr.1984.29.1.445

[112] Y. Murakami and M. Endo, *Effects of Hardness and Crack Geometries on DeltaKth of Small Cracks Emanating from Small Defects*, K. Miller and de los Rios, Eds. Mechanical Engineering Publications, 1986.

[113] ASTM International, "ASTM F3302-18, Standard for Additive Manufacturing – Finished Part Properties – Standard Specification for Titanium Alloys via Powder Bed Fusion," no. February, p. 8, 2018. [Online]. Available: https://www.astm.org/Standards/F3302.htm

[114] A. Das and S. Tarafder, "Geometry of dimples and its correlation with mechanical properties in austenitic stainless steel," *Scripta Materialia*, vol. 59, no. 9, pp. 1014–1017, 2008.

[115] F. Han, B. Tang, H. Kou, J. Li, Y. Deng, and Y. Feng, "Cyclic softening behavior of Ti–6Al–4V alloy at macro and micro-scale," *Materials Letters*, vol. 185, pp. 115–118, 2016. [Online]. Available: http://dx.doi.org/10.1016/j.matlet.2016.08.119

[116] M. Seifi, A. Salem, D. Satko, J. Shaffer, and J. J. Lewandowski, "Defect distribution and microstructure heterogeneity effects on fracture resistance and fatigue behavior of EBM Ti-6Al-4V," *International Journal of Fatigue*, vol. 94, pp. 263–287, 2017. [Online]. Available: http://dx.doi.org/10.1016/j.ijfatigue.2016.06.001

[117] B. Atzori, P. Lazzarin, and G. Meneghetti, "Fracture mechanics and notch sensitivity," *Fatigue and Fracture of Engineering Materials and Structures*, vol. 26, no. 3, pp. 257–267, 2003.